TECHNISCHE UNIVERSITÄT MÜNCHEN

Fakutät für Physik

Fachgebiet Physik weicher Materie

Macromolecular pHPMA-Based Nanoparticles for Solid Tumor Targeting: Behavior in Protein Environment

Xiaohan Zhang

Vollständiger Abdruck der von der Fakultät für Physik der Technischen Universität München zur Erlangung des akademischen Grades eines

Doktors der Naturwissenschaften (Dr. rer. nat.)

genehmigten Dissertation.

Vorsitzende/-r:	Prof. Dr. Ulrich Gerland
Prüfende/-r der Dissertation:	1. Prof. Dr. Christine M. Papadakis
	2. Prof. Dr. Friedrich C. Simmel

Die Dissertation wurde am 22.08.2018 bei der Technischen Universität München eingereicht und durch die Fakultät für Physik am 11.10.2018 angenommen.

Preface

The present research has been conducted in collaboration with Dr. Sergey K. Filippov from the Institute of Macromolecular Chemistry (IMC), Prague, Czech Republic and Dr. Dmitri I. Svergun from European Molecular Biology Laboratory (EMBL), Hamburg, Germany. The synthesis of all polymer samples was performed by Dr. Petr Chytil from the IMC.

Small-angle X-ray scattering (SAXS) experiments were carried out at the beamline P12 at EMBL with the support from the instrument scientists Dr. D. C. Florian Wieland, Dr. Alexey Kikhney, Dr. Andrey Gruzinov and Dr. Tobias Graewert.

Small-angle neuron scattering (SANS) experiments were performed at the KWS-1 instruments operated by JCNS at the Heinz Maier-Leibnitz Zentrum (MLZ), Garching, Germany, with the support from the instrument scientist Dr. Henrich Frielinghaus.

Isothermal titration calorimetry (ITC) studies were carried out at the IMC with support from Dr. Sergey K. Filippov. Fluorescence lifetime correlation spectroscopy (FLCS) studies were performed at the IMC with the help of Dr. Jiří Pánek.

Fluorescence quenching experiments were carried out at the Chair of Pharmaceutical Technology and Biopharmaceutics, Department of Pharmacy, Ludwig Maximilian University of Munich, Munich, Germany, with the help of M. Sc. Letícia Rodrigues and M. Sc. Weiwei Liu.

Abstract

Nanoparticles (NPs) formed by self-assembly of amphiphilic poly(*N*-(2-hydroxypropyl)-methacrylamide) copolymers are potential drug carriers for solid tumor treatment. In this work, their structure and behavior are investigated in solutions of human serum albumin (HSA) in phosphate buffered saline. It is found, that the interaction between HSA and the NPs neither alters the size nor the structure of the NPs. Thus, the drug delivery is not hindered by the presence of HSA.

Abstrakt

Nanopartikel (NP), die durch Selbstassemblierung amphiphiler Poly(*N*-(2-hydroxypropyl)-methacrylamid) Copolymere gebildet werden, eignen sich für den Wirkstofftransport zur Behandlung solider Tumoren. In der vorliegenden Arbeit werden ihre Struktur sowie ihr Verhalten in Lösungen von Humanalbumin (HSA) in phosphatgepufferter Salzlösung untersucht. Es wird gezeigt, dass die Wechselwirkung zwischen HSA und NP weder die Größe noch die Struktur der NP beeinflusst. Die Anwendung als Wirkstofftransportsystem wird also durch HSA nicht eingeschränkt.

List of abbreviations and symbols

abbreviations

APD	avalanche photo diode
AUC	analytical ultracentrifugation
BAM	*N*-*tert*-butylacrylamide
BSA	bovine serum albumin
CMC	critical micelle concentration
DLS	dynamic light scattering
Dom	domperidone
Dox	doxorubicin
EBML	European Molecular Biology Laboratory
EPR	enhanced permeability and retention
FCS	fluorescence correlation spectroscopy
FLCS	fluorescence lifetime correlation spectroscopy
HPMA	*N*-(2-hydroxypropyl) methacrylamide
HSA	human serum albumin
IgG	immunoglobulin G
ITC	isothermal titration calorimetry
NIPAM	*N*-isopropylacrylamide
NP	nanoparticle
*p*AA	poly(acrylic acid)
PBS	phosphate buffered saline
PBS*	phosphate buffered saline containing fluorescence dye
PEG	polyethylene glycol
PGA	polyglutamic acid
*p*HEMA	poly(hydroxyethyl methacrylate)
*p*HPMA	poly(*N*-(2-hydroxypropyl)methacrylamide)
*p*NIPAM	poly(*N*-*iso*-propylacrylamide)
*p*nBA	poly(*N*-butyl acrylate)
RAFT	reversible addition−fragmentation chain-transfer
Rh6G	Rhodamine 6G
SANS	small-angle neutron scattering
SAXS	small-angle X-ray scattering
SLS	static light scattering

SLD	scattering length density
TCSPC	time-correlated single-photon counting
UV-Vis	ultraviolet–visible

symbols

ξ	correlation length from the Ornstein-Zernike structure factor
$Đ$	polydisersity
K_D	Stern-Volmer quenching constant
K_S	association constant for complex formation
k_q	bimolecular quenching constant
pI	isoelectric points
M	molar mass
M_w	weight average molar mass
N	degree of polymerization
$[Q]$	quencher concentration
R_g	radius of gyration
R_h	hydrodynamic radius
S_{OZ}	Ornstein-Zernike structure factor

Contents

1. Introduction

While traditional anti-cancer chemotherapy may bring along side effects, namely high organ toxicity of the drug, non-specific drug distribution and short plasma circulation time, the use of polymer-drug conjugates has been proven to be one of the most promising approaches to improve the delivery of drugs.[1] Their use reduces the toxicity of the drug by site-specific targeting, highly improved pharmacokinetics of the drug and prevents it from degradation before reaching the tumor. This leads to a passive accumulation of the polymer-drug conjugate within tumor tissue, which is known as the enhanced permeability and retention (EPR) effect.[2] One of the extensively studied systems are the poly(*N*-(2-hydroxypropyl)methacrylamide) (*p*HPMA) based polymer-drug conjugates, which features both site-specific delivery and controlled drug release.[3-8] Previously, *p*HPMA copolymers bearing cholesterol moieties and the anti-cancer drug doxorubicin (Dox) bound to the backbone via a pH-cleavable hydrazone bond showed enhanced tumor accumulation and antitumor activity.[9] Using fluorescence correlation spectroscopy (FCS) and small-angle X-ray scattering (SAXS) in phosphate buffered saline (PBS), it was found that, in aqueous solution, elongated nanoparticles (NPs) are formed by self-assembly of the cholesterol moieties above the critical micelle concentration (CMC).[10] These cholesterol moieties are located in the core of the NPs, which is surrounded by a shell formed by *p*HPMA chains. In a subsequent study, the release kinetics of the anti-cancer drug in response to pH changes was investigated in dependence on cholesterol content and type.[11]

However, the behavior of these drug carriers in blood is still poorly understood: On the one hand, hundreds of proteins are present in blood plasma, which may form complexes with the drug nanocarriers.[12] On the other hand, blood proteins may be influenced by the drug carriers and denaturize.[13] These considerations become even more critical when the NPs are formed by random copolymers: some of the hydrophobic segments may not be included in the hydrophobic core region, but are located in the outer part, which is exposed to the aqueous environment.[14] For drug delivery systems based on the self-assembly of random copolymers, this aspect must be examined carefully, since the hydrophobic segments exposed to blood stream may induce significant protein binding,[15] which can influence the functionality of the drug carrier.

Therefore, the present work is devoted to study the behavior of the *p*HPMA drug delivery NPs in a more relevant environment than PBS. As a first step towards real blood, we use human serum albumin (HSA), the most abundant protein in human blood, to mimick a physiological

environment, into which the NPs will be introduced. The choice of HSA is due to the following reasons: (i) Upon injection of the NPs, HSA is most likely the first biological matter which may interact with the NPs due to its high abundance. (ii) It was reported, that HSA plays a crucial role in transporting substances in human body, such as fatty acids, lipids, lipase and hydrophobic drugs.[16-24] It is thus reasonable that HSA also interacts with the *p*HPMA NPs, most probably through complex formation in the manner of building a protein corona.[25]

This work contains mainly two parts. In the first part, scattering methods, namely small-angle X-ray scattering (SAXS) and small-angle neutron scattering (SANS) will be used to investigate mesoscopic structures of the *p*HPMA NPs, HSA as well as their possible complexes using mixed solutions. This way, we seek evidence of any complex formation by comparing the scattering signals from the mixed solutions with the one from the respective pure ones. Additionally, a thermodynamic method, isothermal titration calorimetry (ITC), will be employed, to compensate the results from the scattering methods from another perspective.

In the second part, the mechanism of the observed complexation will be resolved and quantitatively analyzed with the aim of obtaining a binding constant, which is even more challenging, because all components in the mixed solution, namely the NPs, HSA and their possible complex, must be traced and characterized independently. Obviously, additional labelling is required to fulfill this aim. Therefore, fluorescent labels will be used to identify each component: First, the polymeric system will be marked by a far red dye. Second, HSA is intrinsically fluorescent in the UV region. This way, the different colors facilitate spectroscopic methods namely fluorescence lifetime correlation spectroscopy (FLCS) and fluorescence quenching, which can discriminate the components, to further elucidate the complexation of HSA and the NPs.

To summarize, five complementary methods, namely SAXS, SANS, ITC, FLCS and fluorescence quenching, are employed, to investigate the behavior of the *p*HPMA NPs for drug delivery in the presence of HSA.

2. Background

We will first start our discussion of polymer science with a blink into its history, followed by a brief introduction to polymers and their behavior in solution, especially the phenomenon of self-assembly of copolymers in solution, which is the base of modern polymeric therapeutics. This chapter is based on refs. 26, 27.

2.1. Copolymers in solution

As a matter of fact, eras of human history are named after the primary materials that are used, namely the Stone Age, the Bronze Age and the Iron Age. It is thus fair that we name our time as the Polymer Age, in which humans use not only naturally occurring polymer materials e.g. rubber from the trees, but also countless types of polymer products realized by modern chemical synthesis.

No matter whether naturally occurring or man-made, polymer means molecules consisting of many elementary units which are called monomers. These are repeating units connected to each other covalently, through a process called polymerization. The number of monomers in a polymer molecule is defined as degree of polymerization, *N*. In case only one type of monomer is present in a polymer, the molar mass, *M*, of the polymer is then given by a simple rule:

$$M = NM_{mon} \tag{2.1}$$

where M_{mon} denotes the molar mass of the monomer. Such a polymer is called a homopolymer.

When two types of monomers are present in a macromolecule, it is called a copolymer, which can be random, block or graft, depending on the sequence of the monomers that are bonded together (Figure 2.1). When three or more types of monomers are included on a single polymer chain, it is called heteropolymer, which usually has unique properties when dissolved in aqueous solutions and is vital for life. For instance, proteins, which will be intensively discussed in the following chapters, are heteropolymers normally consisting of 20 different monomer types, i.e. amino acids.

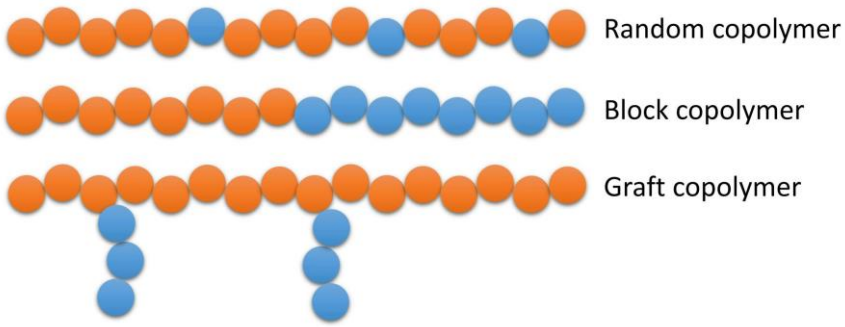

Figure 2.1: Schematic representation of different copolymer types. Two different monomer types are indicated by different colors.

Polymer solutions are usually obtained by dissolving a polymer in a solvent, which is a stepwise process including solvent diffusion and chain disentanglement.[28] This process starts with swelling of the polymer due to penetration of the solvent molecules, leading to a gel, which breaks up subsequently and releasing dispersed polymer chains into the solvent. Depending on the thermodynamic compatibility of the solvent, the polymer may not be completely dissolved in the solvent.

To address the thermodynamics of polymer solutions, or in other words, the thermodynamics of mixing polymers with a solvent, we first discuss briefly the mixing of regular solutions, since it gives the theoretical background of the theory proposed by Flory and Huggins in 1942.

From a thermodynamic point of view, the miscibility of the two components is determined by the free energy of mixing:

$$\Delta G_{mix} = \Delta H_{mix} - T\Delta S_{mix} \tag{2.2}$$

ΔH_{mix} and ΔS_{mix} are the enthalpy and entropy of mixing, respectively. $\Delta G_{\mathrm{mix}} < 0$ is a necessary but not sufficient condition for miscibility. To determine this condition mathematically, we use a 2-dimensional lattice model to calculate the enthalpy and entropy of mixing. Let us now consider a two-component system, the molecules of which are placed on a lattice: Each position in the lattice can be occupied by either of the two components. Using Boltzmann's entropy law and Stirling's approximation, the entropy of mixing is expressed as follows:

$$\frac{\Delta S_{mix}}{N_{mol}} = -R(x_1 ln x_1 + x_2 ln x_2) \tag{2.3}$$

where N_{mol} is the total number of moles of the two components, and x_1 and x_2 the molar fraction of components 1 and 2, respectively. Similarly, the enthalpy of mixing can be calculated from the interaction energies of the neighboring molecules, i.e. 1–1, 1–2 and 2–2 contacts:

$$\frac{\Delta H_{mix}}{N_{mol}} = Bx_1x_2 \tag{2.4}$$

B is a constant depending on the energies of vaporization of 1 and 2. Equation 2.2 can be thus rewritten as

$$\frac{\Delta G_{mix}}{N_{mol}} = Bx_1x_2 + -RT(x_1 lnx_1 + x_2 lnx_2) \tag{2.5}$$

The inflection points at which $(d^2(\frac{\Delta G_{mix}}{N_{mol}})/dx_1^2)$=0, are called spinodal points, pointing to the thermodynamic limits of metastability (Figure 2.2). Between the concentrations corresponding to the spinodal points, $(d^2(\frac{\Delta G_{mix}}{N_{mol}})/dx_1^2)$ is negative, leading to an unstable system. The binodal points have a common tangent in the plot of ΔG_{mix} against x_1, and can be found by differentiating ΔG_{mix} with respect to x_1. In the case of a symmetric ΔG_{mix}, the binodal points are the two minima. The compositions lying between the binodal and spinodal points are called metastable region, i.e. only stable to small composition fluctuations, but not large ones. The binodal and spinodal points, as well as the stable, metastable and unstable regions are illustrated in Figure 2.2.

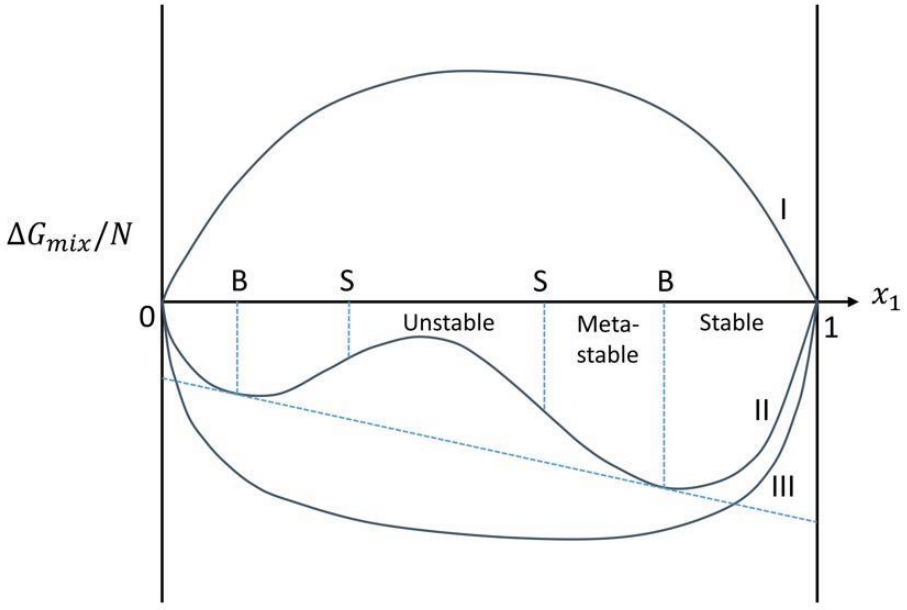

Figure 2.2: Free energy shown qualitatively as a function of composition x_1 with respect to the regular solution model. The curves I-III are representatively illustrated for three solutions having the same temperature but increasing *B* value, i.e. $B_I > B_{II} > B_{III}$, and $B_{III} = 0$ J mol^{-1}. I: Solution is unstable in all composition range. II: Miscibility depends on composition. B and S mark binodal and spinodal points, respectively. III: Solution is stable over full composition range.

The Flory-Huggins theory describes the general phase behavior of polymer solutions based on the idea discussed above and adding the following conditions:[29-31] When positioning a polymer in the lattice, after positioning the first segment, the second one must be placed at a neighboring position until the whole polymer chain is positioned. The entropic term of mixing, ΔS_{mix}, is described in this case as:

$$\frac{\Delta S_{mix}}{N_l} = -R(\varphi_1 ln\varphi_1 + \frac{\varphi_2}{x} ln\varphi_2) \tag{2.6}$$

φ_1 and φ_1 are the volume fractions of solvent and polymer, respectively. N_l is the total number of positions in the lattice, and x the number of positions in the lattice each polymer occupies. The enthalpy of mixing is calculated by considering the interaction energies between the solvent molecules and the solute segments. It is given by:

$$\frac{\Delta H_{mix}}{N_l} = RT\chi_{12}\varphi_1\varphi_2 \tag{2.7}$$

χ_{12} is called the interaction parameter. Combining equation 2.2, 2.6 and 2.7 gives the change in free energy on mixing:

$$\frac{\Delta G_{mix}}{N_l} = RT(\varphi_1 ln\varphi_1 + \frac{\varphi_2}{x} ln\varphi_2 + \chi_{12}\varphi_1\varphi_2) \tag{2.8}$$

This is the general case of free energy proposed by Flory and Huggins, recalling the necessary condition for mixing: The sign of $\Delta G_{mix}/N_l$ must be negative. However, in the real case, more aspects must be considered. For instance, molar mass polydispersity and a finite volume change upon mixing may invalidate equation 2.8.

Now, we continue to discuss a specific case of polymer solution, namely amphiphilic copolymers in solution, which contain both hydrophilic and hydrophobic segments. As a result, microphase separation may happen in aqueous solutions as well as in organic ones. We will concentrate on the former case in this work, because most biological processes, including delivering drugs in humans, take place in aqueous media.

The process, through which amphiphilic copolymers form micelles structure in water spontaneously without extern directions, is called self-assembly.[32-37] Thermodynamically, this process is driven by minimization of the free energy in the system, which is mainly realized through limiting the interactions between hydrophobic blocks and water molecules. Such interactions are energetically unfavored, since they lead to rearranging of the water molecules surrounding the hydrophobic blocks, thus lowering the entropy of the system. As a result, the most common structure of micelle in water is a core-shell structure having a hydrophobic core

and a hydrophilic shell (Figure 2.3). The hydrated hydrophilic shell prevents further growth of the hydrophobic core and aggregation of the micelles. In pharmaceutical topics, the shell is usually used as a protection for the hydrophobic core, which encapsulates other substances e.g. hydrophobic drugs.[38]

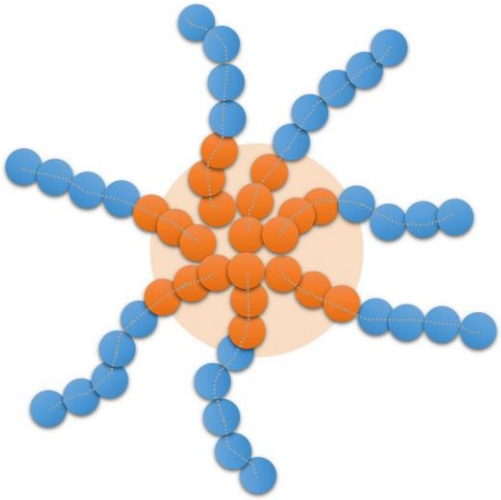

Figure 2.3: Schematic sketch of a micelle formed by block copolymers in aqueous solution. The orange shadow marks the hydrophobic core region.

At a given temperature, micelle formation takes place at a specific concentration which is called the critical micelle concentration (CMC). Below the CMC, there are only molecularly dissolved copolymer chains, which are called unimers, in solution. Above the CMC, micelles form and coexist with unimers. The CMC depends on temperature and can in many cases be affected by adding other substances to the system, e.g. salt or alcohol.

We concentrate now on a specific case of amphiphilic copolymers, namely random copolymers. These are copolymers having monomer units that are randomly distributed on the chain (Figure 2.1). Compared with block copolymers, which usually self-assemble into well-defined architectures having low dispersity in size, but are usually difficult and time-consuming to synthesize, random copolymers tend to form less well-defined self-assembled structures but are easier to synthesize.[39]

While the morphology of self-assembled block copolymers depends on the length of the hydrophilic and hydrophobic blocks, the morphology of self-assembled random copolymers is defined by their hydrophilic/hydrophobic balance. Therefore, in aqueous solutions, the self-assembly of random copolymers is often realized by using a high molar fraction of the hydrophobic monomers, or a relative low molar fraction but highly hydrophobic monomers.

For instance, it was observed that *N*-(2-hydroxypropyl) methacrylamide (HPMA) copolymers decorated by only 2 mol% highly hydrophobic cholesterol side groups form ellipsoidal micelles (nanoparticles) in aqueous solution.[9, 10]

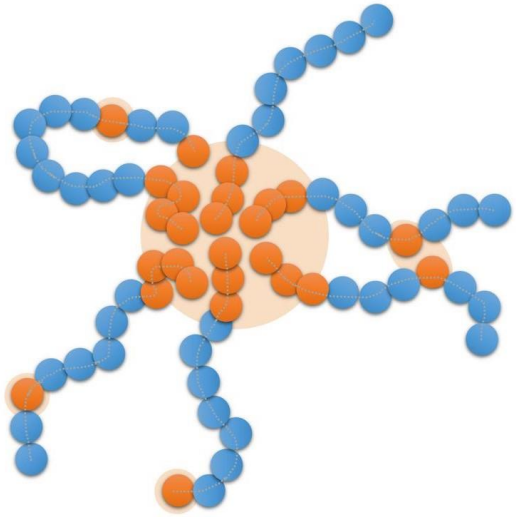

Figure 2.4: Schematic representation of a self-assembled micelle from random copolymers. A certain fraction of the hydrophobic monomers (orange) are included in the hydrophobic core. In addition, hydrophobic monomers may dangle in the outer hydrophilic shell, or form small hydrophobic sub-domains in the hydrophilic shell.

Another interesting aspect of random copolymers is the spatial distribution of the hydrophobic segments in the assembled structures. Self-assembled micelles formed by block copolymers usually have sharply phase-separated hydrophobic and hydrophilic domains. In contrast, in the case of random copolymers, the hydrophobic and hydrophilic domains may interpenetrate each other (Figure 2.4). For micellar structures in aqueous solution, this means that some of the hydrophobic segments may not be included in the hydrophobic core region, but are located in the outer part which are exposed to the aqueous media.[14] For drug delivery systems based on the self-assembly of random copolymers, this aspect must be considered carefully since the hydrophobic segments exposed to the blood stream may induce significant protein binding,[15] which can influence the functionality of the drug carrier.

The self-assembly of amphiphilic random copolymers is described by the flower micelle model developed by Sato et al.[40, 41] Let us consider the random copolymer having hydrophobic graft-chains presented in Figure 2.5. The main chain and graft chains consist of P_M monomer units and P'_G monomer units, respectively. We use x to denote the molar fraction of the graft chains, which are distributed along the main chain randomly. The total number of the graft-chain units

is $P_G = x\,P_M\,P'_G$. The total degree of polymerization of the whole chain is thus $P = P_M + P_G = P_M(1+ xP'_G)$. We assume that the main-chain and graft-chain units as well as the solvent molecules occupy lattice sites having size a.

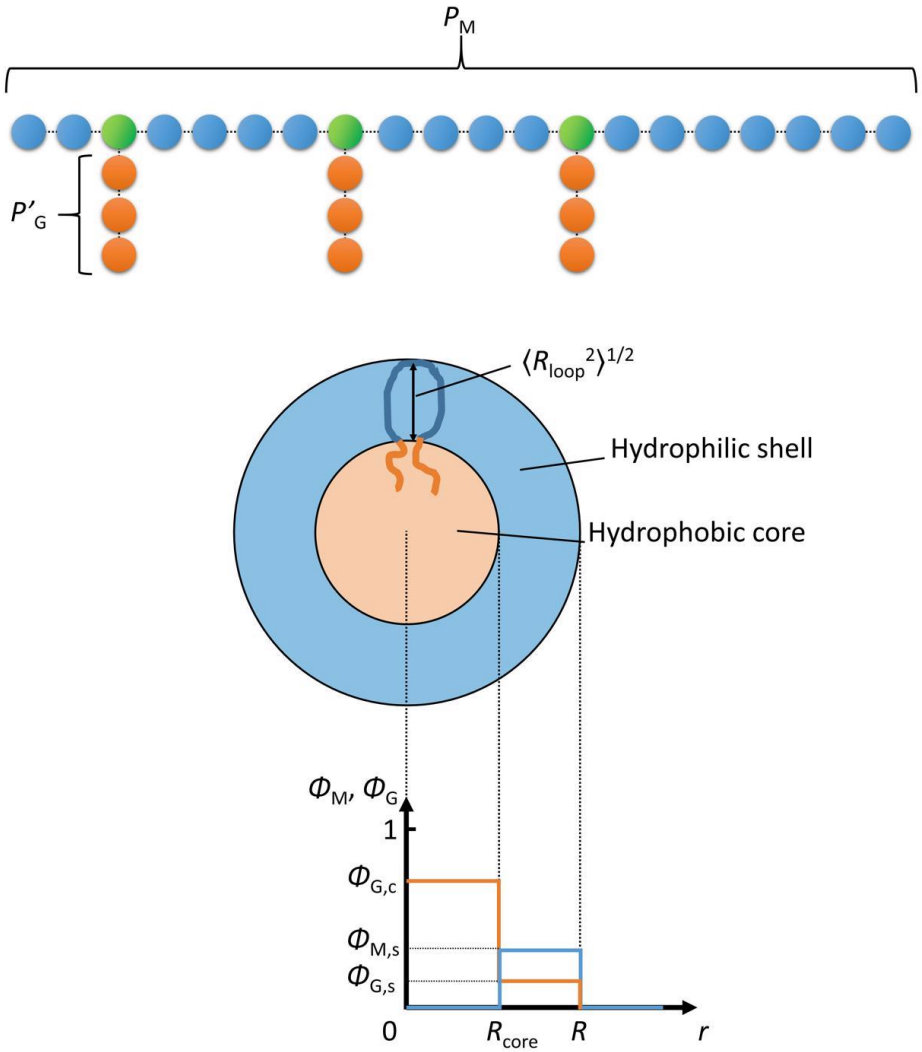

Figure 2.5: Schematic diagrams of a random copolymer chain bearing hydrophobic graft chains (upper) and a flower micelle formed by the copolymers (lower), together with the radial concentration profiles of the main-chain and graft-chain units (see text).

Provided that the graft-chain units are sufficiently hydrophobic, graft chains aggregate to form a hydrophobic core. When more than one graft chains are present on a single copolymer, the main chain of which tends to form a loop in aqueous medium. As a result, a flower micelle forms by a number of m copolymer chains (Figure 2.5). At this, only the graft chains at roots of the main chain can enter the hydrophobic core, and the remaining ones are in the shell. According to the wormlike chain model, [42-44] the probability of loop formation rapidly diminishes to zero when the chain contour length reducing to ca. $1.6q$, where q is the persistence

length. In other words, the portion of the chain shorter than $1.6q$ cannot form the loop due to chain stiffness. In the following discussions, we consider the flower micelle consisting of loop chains having this minimum loop size.[45] The number of main-chain units per minimum loop chain P_{loop}, and the number of loops per chain, n_{loop}, are given by

$$P_{loop} = \frac{1.6q}{a}, n_{loop} = \frac{P_M}{P_{loop}} \tag{2.9}$$

Hence the number of graft chains included in the hydrophobic core and in the shell, $x_c P_M$ and $x_s P_M$, respectively:

$$x_c P_M = \lambda n_{loop}, x_s = x - x_c \tag{2.10}$$

where λ denotes the number of graft chains included in the core at each root of the loop. It is assumed here that n_{loop} is much larger than unity.

Furthermore, we use a simplified model to demonstrate the flower micellar phase, of which radial volume fractions of the main-chain and graft-chain units are given by:

$$\emptyset_M = \begin{cases} 0, & 0 \le r < R_{core} \\ \emptyset_{M,s}, & R_{core} \le r < R \\ 0, & R \le r \end{cases}, \emptyset_G = \begin{cases} \emptyset_{G,c}, & 0 \le r < R_{core} \\ \emptyset_{G,s}, & R_{core} \le r < R \\ 0, & R \le r \end{cases} \tag{2.11}$$

A representative illustration of the radial volume fractions are given in Figure 2.5. R_{core} and R are the radii of the micelle core and the whole micelle, respectively. The solvent fraction is given by $\Phi_S = 1 - \Phi_M - \Phi_G$ at each radial distance r. Using the wormlike chain model, ${R_{core}}^2$ and the mean square distance from the end to the midpoint of the loop $\langle {R_{loop}}^2 \rangle$ are expressed in terms of the persistence length of the graft chain, q_G, and of the copolymer main chain, q, respectively:[42]

$$({R_{core}}/{a})^2 = \left(\frac{2q_G}{a}\right) {P'}_G - 2\left(\frac{2q_G}{a}\right)^2 (1 - e^{-{P'}_G a/q_G}) \tag{2.12}$$

$$\frac{\langle {R_{loop}}^2 \rangle}{a^2} = \frac{{P_{loop}}^2}{\sqrt{42.5 - 10.7\left(\frac{aP_{loop}}{2q}\right) + 16(aP_{loop}/2q)^2}} \tag{2.13}$$

The radius of the whole micelle, R, is given by:

$$R = R_{core} + \langle {R_{loop}}^2 \rangle^{1/2} \tag{2.14}$$

The flower micelle model demonstrates clearly the presence of hydrophobic units in the shell of the micelle. And the fraction of these hydrophobic units, which are not included in the core, is dependent mainly on two conditions: the abundance of the graft-chain units on the main chain,

and the total length of the main chain, which determine the stiffness of the copolymer chain and the probability of loop formation. However, it is important to note that the flower micelle model is a simplified model, which considers only spherical micelles. In reality, random copolymers may form micelles having different shapes and structures. For instance, Tian et al. observed wormlike rods formed by poly(hydroxyethyl methacrylate) (*p*HEMA) randomly modified by the hydrophobic 2-diazo-1,2-naphthoquinone in solution.[46] It was reported by the authors that these rods were thermodynamically unstable, and thus cannot be treated in the present theory which is on the basis of statistical thermodynamics.

2.2. Polymer therapeutics and drug delivery

In this chapter, we discuss the motivation of delivering drugs using polymers and give introduction into some developed polymeric drug delivery systems, followed by an introduction to the enhanced permeability and retention (EPR) effect, which is of key importance in antitumor drug delivery.

2.2.1. Modern polymeric drug delivery systems

In conventional therapeutics, drugs having low molar mass are widely used, conferring them the capability to access various parts in the body and enter and affect numerous cell types.[47] These drugs are thus effective against many diseases. However, their wide and uncontrollable distribution in the body leads to side effects. Depending on the desired position of drug action, higher doses of the drug may be required to achieve a satisfactory pharmacological response. Moreover, low molecular weight usually results in a rapid renal clearance, hence more frequent administration is necessary. Therefore, a potential drug delivery system must fulfill the following aspects: (i) Drugs are protected from interactions with other substances before they reach the action site; (ii) The carrier itself does not induce interactions with other macromolecules in the body, e.g. proteins. With respect to these factors, many attempts were made to use polymeric systems as drug carrier. As one of the pioneering works, in 1955, Jatzkewitz attached a drug to the water-soluble polymer polyvinylpyrrolidone, which is used as a plasma expander.[48, 49] In the following years, more water soluble polymer-drug conjugates were synthesized by Ushakov et al.[50, 51] In 1975, Helmut Ringsdorf first reported an analysis of a complete polymeric drug delivery system and presented the first clear concept of using polymers for drug targeting.[52] In Ringsdorf's model, a polymeric drug delivery system consists of five components: (i) polymer backbone, (ii) drug, (iii) spacer, (iv) targeting moiety and (v) solubilizing agent. As the most important component, the polymer backbone should be water-soluble, non-toxic, non-immunogenic and can be eliminated from body, e.g. through biodegradation.[53] The most commonly used and studied polymer backbone types, namely polyethylene glycol (PEG),[54-57] *N*-(2-Hydroxypropyl) methacrylamide (HPMA)[3-8] and polyglutamic acid (PGA),[58-61] are summarized in Figure 2.6 together with their main features.

The drug is either directly conjugated or linked via a stimuli-responsive bond to the polymer backbone, which allows the drug release. Several types of stimuli can be utilized to trigger the drug release, e.g. through a change of pH value,[62-65] temperature,[66-68] external electric field,[69, 70] or ion concentration.[71]

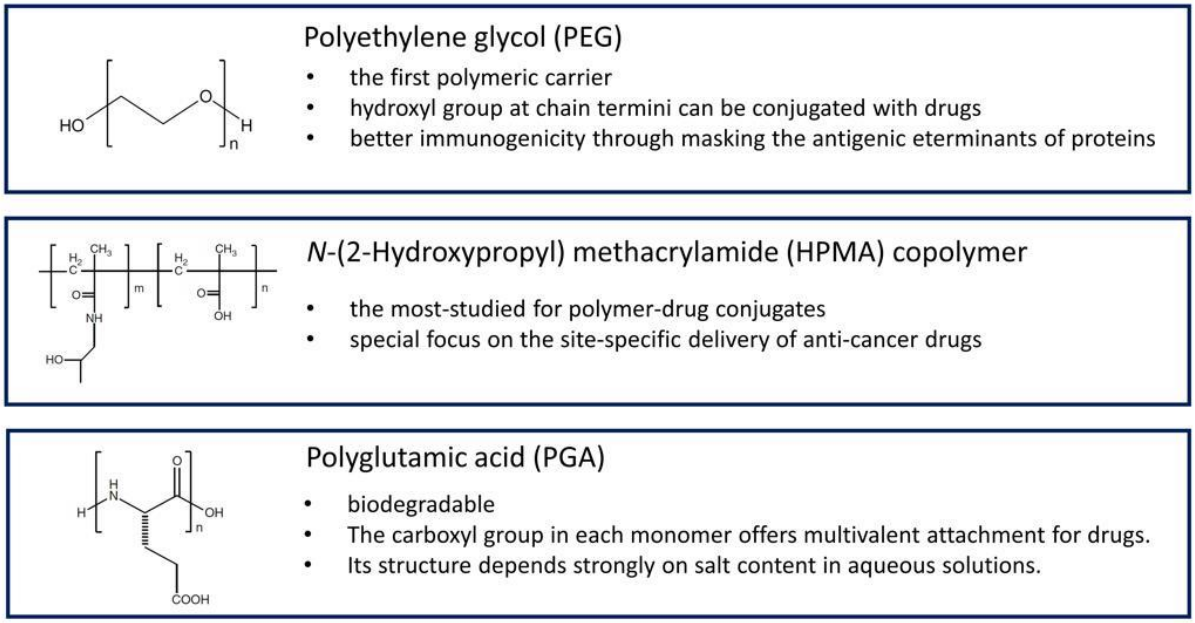

Figure 2.6: A summary of the most commonly used polymer backbones for drug delivery, giving the chemical structures with a brief introduction. Adapted from ref. 1.

Moreover, several common structures of drug carriers have been commonly used, namely linear polymers, micelles, dendrimers and hyperbranched polymers (Figure 2.7). Among these, micelles, especially the self-assembled ones from amphiphilic copolymers, have developed great potential in polymer therapeutics.

Amphiphilic copolymers are known to self-assemble into micellar structures in aqueous media (see Chapter 2.1). The formed unique structures having a narrow size distribution. These characteristics makes amphiphilic copolymer a good choice to be used as a platform of potential drug delivery systems: The hydrophobic core region are supposed to carry drugs, whereas the hydrophilic outer shell protects these from the exterior.[72]

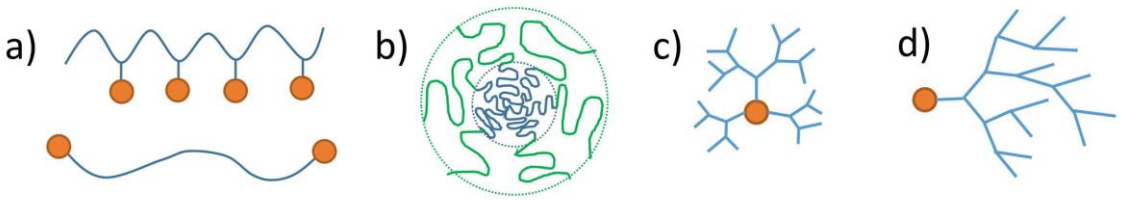

Figure 2.7: A sketch of different architectures of drug carriers. (a) Multivalent (upper) or divalent (lower) linear polymer. In either cases, a single polymer backbone forms a random coil

structure. (b) Micelles formed by amphiphilic copolymers through self-assembly. (c) A dentrimer consisting of a central core and branched units which repeat in the same order. (d) Hyperbranched polymer, which differs from a dentrimer due to its random branched structure.

2.2.2. The EPR effect

This chapter is based on refs. 73, 74.

One of the greatest breakthroughs, which leads to a more general understanding for the targeted antitumor drug delivery, was the discovery of the EPR effect. Most solid tumors have defective blood vessels, which usually result in an increased vascular permeability to ensure a sufficient supply of nutrients for the tumor's rapid growth. The EPR effect exploits this unique feature of solid tumors to facilitate transport of drugs: Macromolecules having a molar mass larger than 40000 g mol^{-1} can selectively leak out of blood vessels into tumor tissues and accumulate in them (Figure 2.8a).[75] In contrast, due to the relative high molar mass and hence large size, these macromolecules cannot pass through blood vessel walls in the healthy tissues, which have a much lower permeability than the tumor tissues (Figure 2.8b). The molar mass of the macromolecules which are transported in solid tumors has thus become the first and most important consideration in the framework of the EPR effect. Sometime, this requirement in molar mass is also expressed by means of molecular size which should range from 10 to 200 nm.[76]

However, there are also other aspects which must be taken into account to make the EPR effect occur. Biocompatibility is commonly regarded as the second condition for the EPR effect. Because drugs, which are mostly chemically modified substances and denatured proteins, are rapidly cleared from the circulation. This results in too short plasma half-lives that are not enough for the EPR effect.

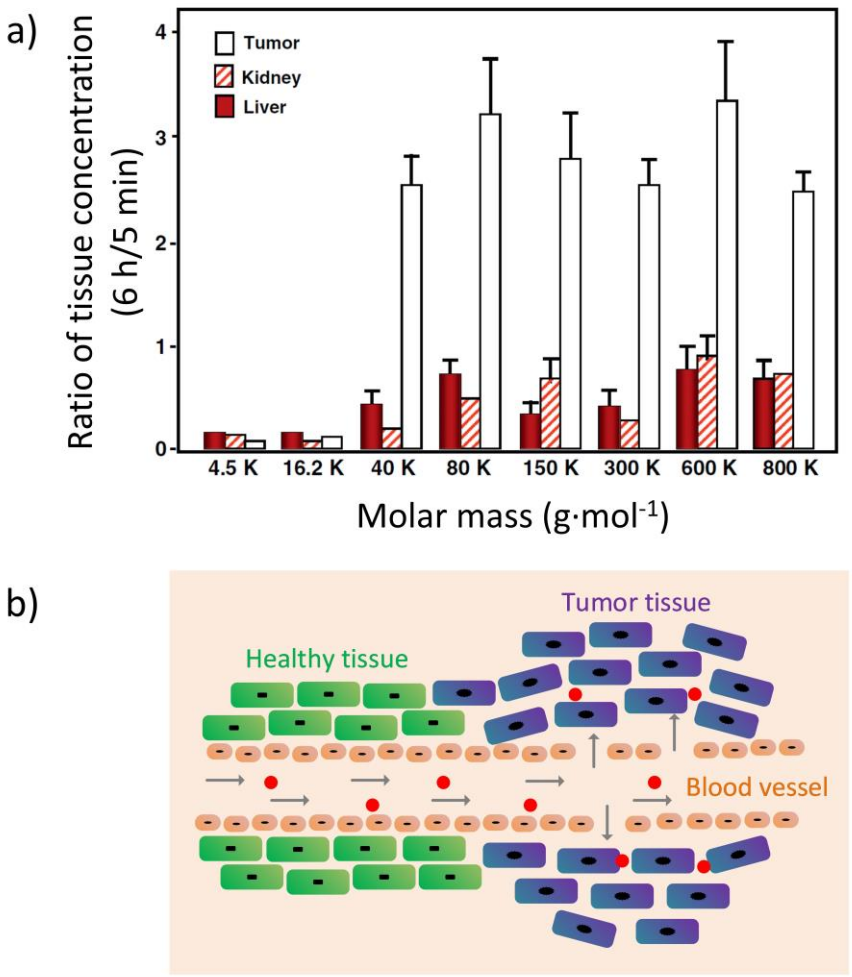

Figure 2.8: (a) Tumor uptake of the macromolecular HPMA copolymers having various molar mass. The amount of uptake is shown as the ratio of the concentration in the tumor between at 6 h and 5 min. A strong increase of the tumor uptake is seen when the molar mass is above 40000 g·mol^{-1}. Reprinted from ref. 74 with permission from Elsevier. (b) Sketch of the EPR effect. Macromolecules (red) leak from the blood vessel to the tumor tissue.

Based on these discussions, two important conclusions in designing drug carriers against solid tumors can be made: (i) The system must have an easily tunable molar mass, which is equivalent to tunable particle size in case of drug delivery system based on self-assembly. (ii) The materials being used have to be biocompatible and have optimal plasma half-lives.

2.3. Interaction between nanoparticles and blood proteins

This chapter is based on refs. 15, 77.

From a biological and medical point of view, nanoparticles (NPs, including self-assembled micelles) have extensively developed their applications in drug delivery, because their size can be tuned to access different targets. It is a well-known fact that the surfaces of biomaterials (implants, medical devices, etc.) are immediately covered by biomolecules (proteins, enzymes, etc.) when they are introduced into a biological environment. In comparison with these bulk materials, NPs have an extremely high surface-to-volume ratio and much more active surface chemistry. For medical applications, more specifically for targeted drug delivery, injection of NPs is normally required. Therefore, the injection of NPs into blood stream results in a surface being covered by adsorbed blood proteins, which is the so-called "protein corona".[25, 77-91]

2.3.1. Composition and development of protein corona

The adsorption of proteins on the NP's surface is determined by the binding affinity between the proteins and the NP, as well as by the protein-protein interactions.

Formation of the protein corona is a dynamic and competitive process, as a result of different protein binding affinities: Upon dispersion of the NPs in blood stream, they are rapidly covered by the abundant proteins which may have low affinity but high mobility. Subsequently, these proteins may be replaced by the ones having low mobility but higher affinity, which is known as the Vroman effect. It is notable that this replacement does not necessarily mean completely dissociation of the low-affinity proteins, since it has been shown that different layers of proteins may be present simultaneously: A hard corona consisting of the high-affinity proteins at the inner layer and a soft corona consisting of the loosely bound ones at the outer layer (Figure 2.9).[82] The presence of multiple layers of a protein corona is also supported by the size of a protein corona, which is in the range of 3–15 nm, which is too thick to result from only a single layer of adsorbed proteins.

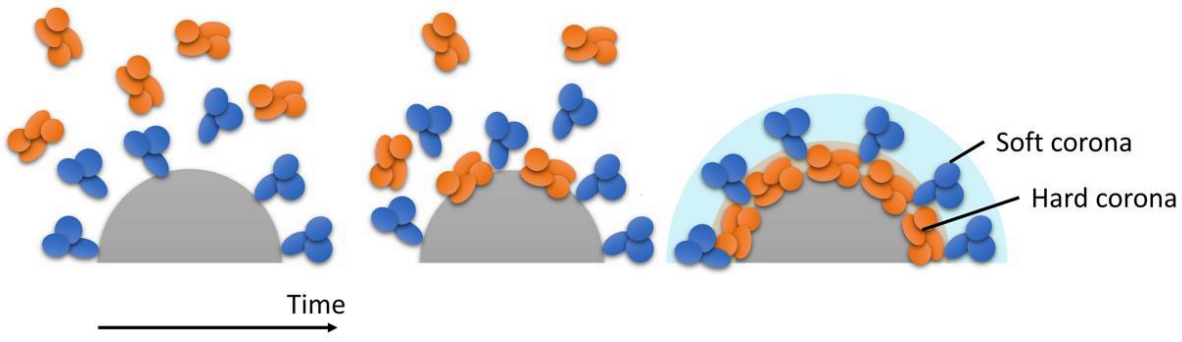

Figure 2.9: Representative sketch of formation of a protein corona. The NP (grey) is rapidly covered by one type of proteins (blue) having high mobility and exchange rate, which is subsequently replaced by another type of proteins (orange) having higher binding affinity but lower exchange rate. The result is the formation of a hard corona and a soft corona.

The exact interaction type between different layers of a protein corona is still not completely understood. In one study, it is assumed that the hard corona interacts with the NP's surface, while the soft corona proteins interact with the hard corona via protein-protein interactions.[88] A similar model was proposed by Simberg et al., in which the corona proteins were divided into "primary binders" and "secondary" binders:[92] The "primary binders" recognize directly the NP's surface and adsorb on it, followed by the subsequent association of the "secondary binders" with the "primary binders" via protein-protein interactions. Moreover, it was reported that the soft and the hard corona can also be characterized by their different exchange times: The hard corona usually shows very long exchange times, of the order of several hours.[93]

Another important issue in corona formation is its development with time. Let us ignore the corona composition for a moment, or in other words, in which layer one type of protein is exactly located, and concentrate only on how the total adsorbed amount of the protein varies with time. A study on kinetics of protein adsorption was reported by Jansch et al. in 2012, which shows exemplarily how the adsorbed amount of different proteins may vary with time. In this work, the relative amount of different types protein adsorbed to the superparamagnetic iron oxide NPs was analyzed in dependence on incubation time, ranging from 0.5 to 240 min (Figure 2.10). It was found, that after 0.5 min incubation time, fibrinogen is already the dominant protein adsorbing onto the NP's surface, and this original amount seems to remain constant with increasing incubation time. The amount of adsorbed immunoglobulins, however, increases significantly after 30 min, in contrast to apolipoproteins, which seem to partially desorb after 30 min. Interestingly, the most abundant protein, albumin, does not show any obvious adsorption over the whole incubation time. One plausible explanation is that the majority of the adsorbed albumin was replaced by other proteins in the first several seconds via the Vroman effect.

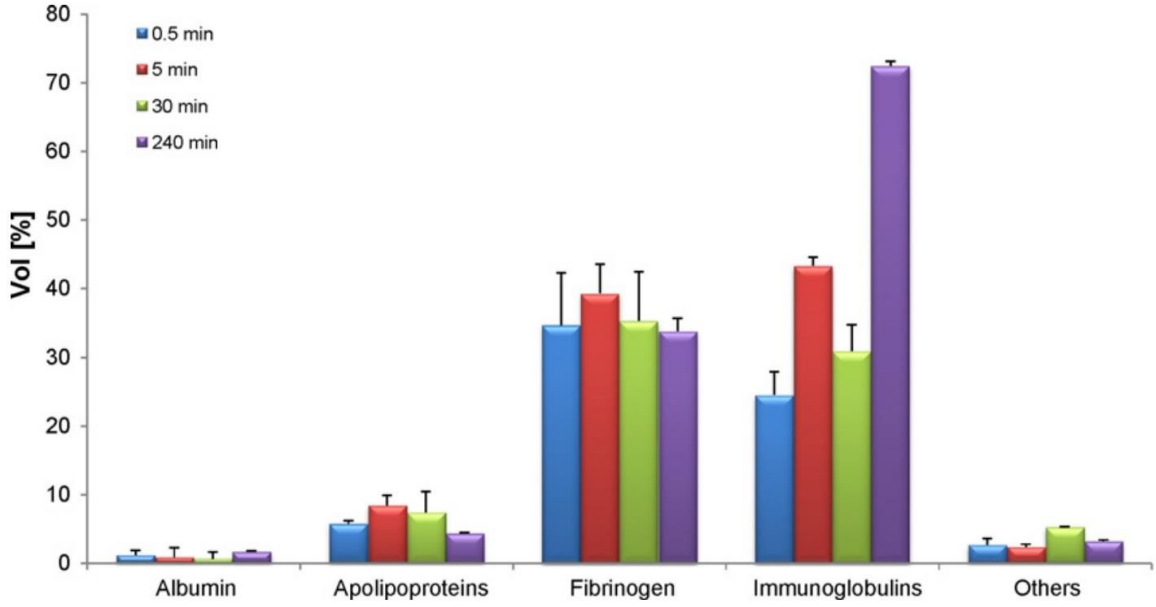

Figure 2.10: Relative volume of major proteins from human blood plasma adsorbed onto the superparamagnetic iron oxide NPs in dependence on different incubation times. Reprinted from ref. 94 with permission from Elsevier.

2.3.2. Protein conformation

It is well known that binding of proteins to a planar surface normally induces significant structural changes in the secondary structure of proteins. The high curvature of the surface of NPs is thus assumed to help proteins to maintain their structure. However, studies of a variety of NP surfaces and proteins indicate that structural changes in proteins may still be present. These structural rearrangements of proteins upon adsorption to NPs are called "conformational changes". If there are hydrophobic or electrostatic interactions between a sequence of the protein and the NP, the conformational changes are usually thermodynamically favorable. For example, bovine serum albumin rapidly adsorbs on Au surfaces, which causes conformational changes at both the secondary and the tertiary structure level.[95] Moreover, these conformational changes are mostly irreversible. For instance, such changes in the iron-transport protein transferrin are not recovered when they desorb from iron oxide NPs.[96]

2.3.3. Parameters affecting the protein corona

There are numerous investigations characterizing the binding of protein and NPs, which were observed to depend on the NP's size,[97] shape,[98] crystallinity,[99] surface area,[100] and surface hydrophobicity.[25] These parameters have been reviewed by various groups.[12, 15, 85, 101] Among

these parameters which affects the NP-protein binding and formation of protein corona, the surface properties such as hydrophobicity and surface charge play a more significant role than the other parameters.[102] In the following part, we will concentrate on these two most important parameters.

The surface charge of the NPs is widely regarded as the most important factor affecting protein-NP interaction. It has been reported that protein binding increases with the surface charge of NPs. Proteins with low isoelectric points (pI < 5.5), e.g. albumin, prefer to adsorb on positively charged NPs, whereas the negatively charged NPs favors the adsorption of proteins with high isoelectric points (pI > 5.5) such as immunoglobulin G (IgG).[102] Besides, a surface charge may as well denature the adsorbed proteins, as reported in a study where protein adsorption to gold NPs were studies with positive, negative and neutral ligands. It was found that the proteins denature in the presence of both positive and negative ligands, but maintain their structure with the neutral ligand.[12]

The hydrophobicity influences both the amount of bound proteins as well as the composition of the formed protein corona. There is a general rule for surface hydrophobicity: the higher the hydrophobicity, the stronger the adsorption of proteins, as was clearly presented by Cedervall et al. in a study using ITC, where human serum albumin (HSA) was titrated into solutions of copolymeric NPs of 70 nm diameter but have different hydrophobicity, which was tuned through variation of the ratio between the hydrophilic and hydrophobic monomers (Figure 2.11). Much higher binding enthalpy was observed in case of the titration of HSA to more hydrophobic NPs. However, a higher surface hydrophobicity does not necessarily mean a higher binding affinity for the proteins. In other words, NPs with higher hydrophobicity may present other factors which facilitate protein adsorption in addition to affinity. For example, it was reported that hydrophobic NPs still adsorb more albumin proteins than hydrophilic NPs, even though the affinity of the albumin to both NP types are roughly the same. This stronger adsorption was attributed to the presence of more binding sites in the hydrophobic NPs, which may result from “clustering” of the hydrophobic segments forming “islands” that serve as binding sites.[79]

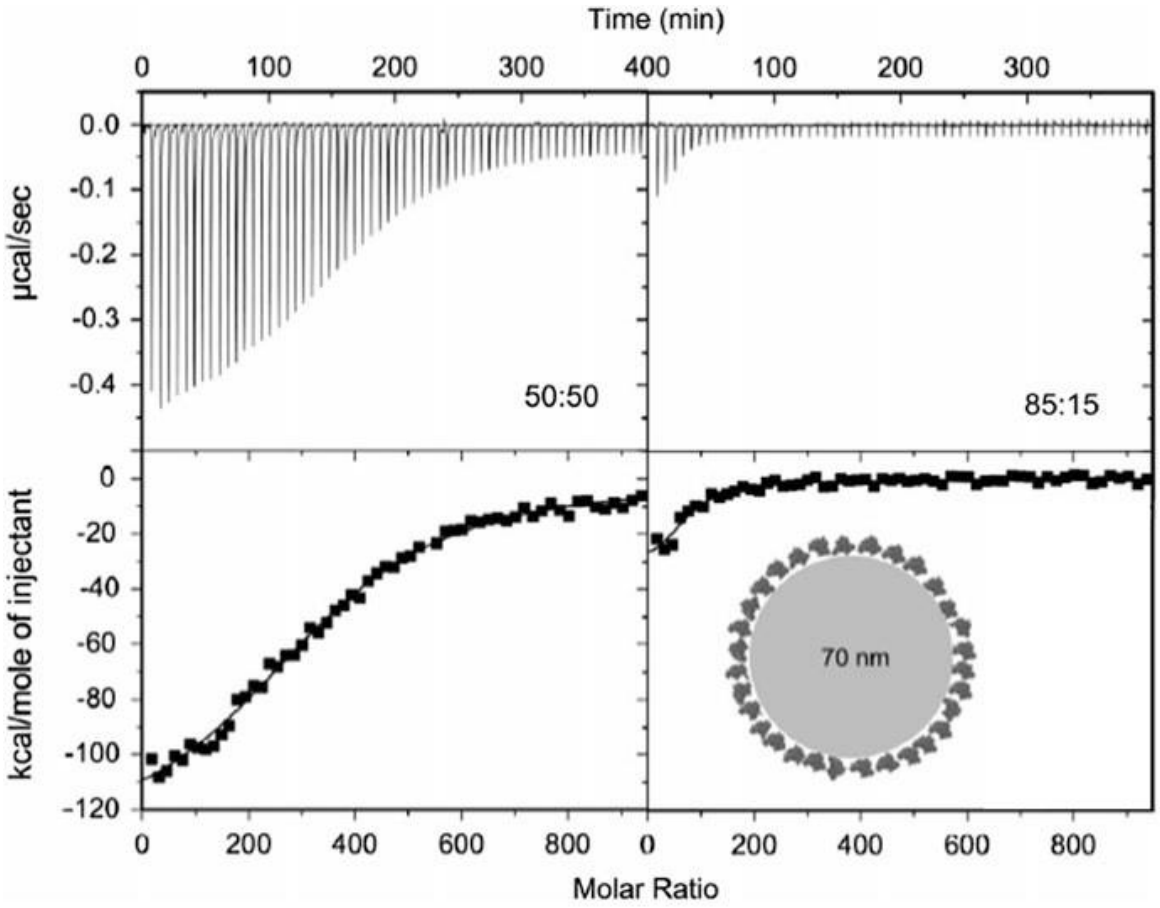

Figure 2.11: ITC results of HSA titrated into solutions of copolymeric NPs from hydrophilic *N*-isopropylacrylamide (NIPAM) and hydrophobic *N*-*tert*-butylacrylamide (BAM). The hydrophobicity of the NPs was tuned through variation of the copolymer ratio between NIPAM and BAM, which is indicated in the figure. Inset: Size comparison of albumin and a NP of 70 nm diameter. Adapted from ref. 25 with permission.

Recently, additional factor such as temperature, starts to draw attention and is proven to strongly affect the composition of protein corona. A better understanding of the role of each above-mentioned physiochemical parameter on the protein-NP binding is promising for the design of targeting drug carriers. In investigations of complex systems containing NPs and proteins, due to the interplay of parameters, it is a widely used strategy to study only one variable using single protein type.

2.3.4. Fate of drug delivery systems based on NPs

For drug delivery systems based on NPs, the formation of a protein corona can be dramatic: It was reported that strong aggregation of NPs was induced by protein adsorption to the NP's surface.[103] Moreover, a dense corona is very likely to hinder the release of the drug after the NP

reaches the target location. Therefore, it is important to optimize the NPs for drug delivery, in a way that protein corona formation and protein binding are minimized. This is the so-called "stealth" effect of nanocarriers: [104] On one hand, the stealth NPs remain unaltered by the blood proteins and their function is thus unaffected. On the other hand, stealth also means that the proteins are not influenced by the NPs, that is, the proteins which are exposed to the NPs should not undergo conformational changes, which is linked to proteins' functions explicitly.

3. System under investigation

3.1. Previous results

Cancer treatment with a polymeric drug carrier has been in the focus of investigations over the last few decades.[1, 72, 105] Drug delivery is usually a two-step process, which involves the transport of the drug from the injection point to the tumor tissue and the subsequent release of the drug. A potential system must ensure a minimum contact between the anti-cancer drug and healthy tissues during the transport and an optimum drug release rate once targeted.

As one of the most studied and promising polymeric drug delivery system, poly(*N*-(2-hydroxypropyl)-methacrylamide) (*p*HPMA) has been shown to feature both site-specific delivery and excellent biocompatibility.[3-8] In the very early designs, the drug monomers were directly copolymerized with HPMA monomers.[106] Due to a lack of hydrophobicity, these copolymers usually form single chain confirmation in solution, the size of which may still not be high enough for an optimum EPR effect. Moreover, the drug is not protected from contact with other biological systems, which may lead to side effects. To solve these issues, a commonly used strategy is to decorate the copolymer by additional hydrophobic groups, which induces the self-assembly of several copolymer chains. Depending on the type, quantity and position of the additional hydrophobic substance on the copolymer chain, different nanostructures may form through self-assembly. The early developments of the HPMA drug delivery system are summarized in Figure 3.1.

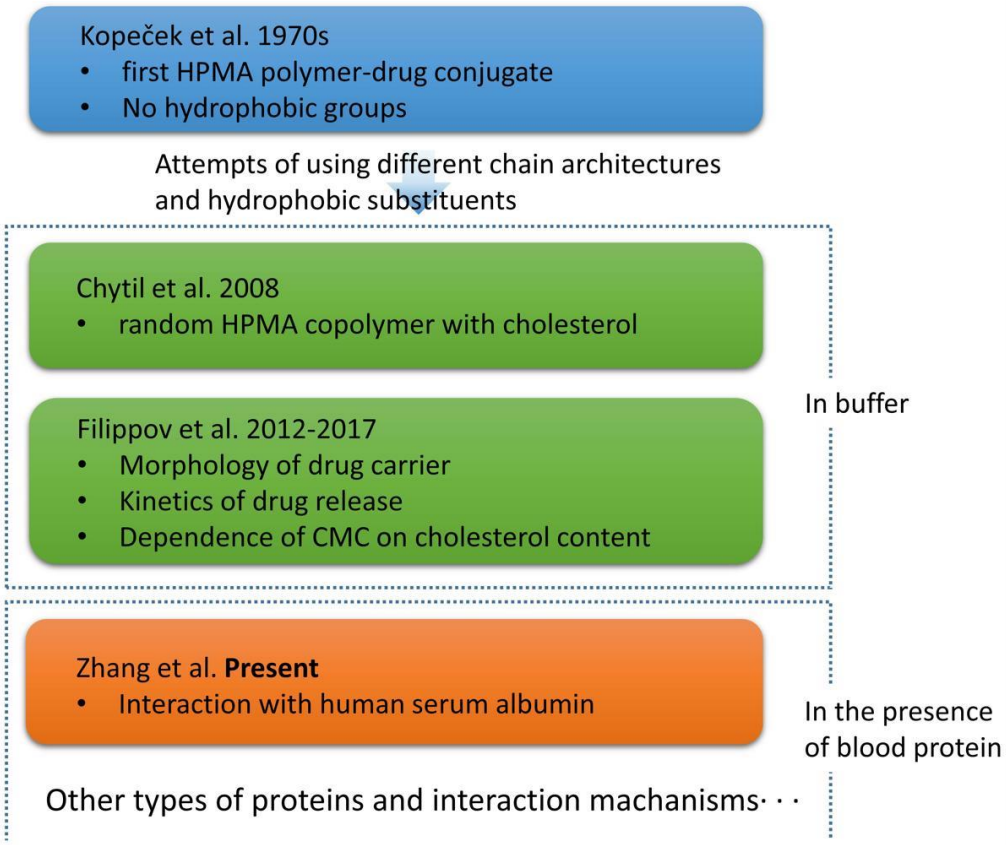

Figure 3.1: An overview of the ongoing research of the drug delivery system based on *p*HPMA copolymer bearing cholesterol side groups.

In 2008, *p*HPMA copolymers bearing different hydrophobic substituents (dodecyl, oleoyl and cholesterol) were synthesized by solution radical polymerization, and investigated in phosphate buffered saline (PBS) by Chytil et al. (Figure 3.2).[9] The anti-cancer drug doxorubicin (Dox) was bound to the backbone of the copolymers via a pH-cleavable hydrazone bond. Using dynamic light scattering (DLS), NPs having hydrodynamic radius ranging from 10 to 100 nm were observed. Among the three copolymers, the *p*HPMA copolymer bearing cholesterol groups was observed to form NPs having an average hydrodynamic radius at 10 nm, which is still in the optimal range for the EPR effect (Chapter 2.2.2). This is in contrast to the NPs formed by the copolymers bearing dodecyl and oleoyl, which had a smaller hydrodynamic radius (below 10 nm) and were inappropriate to be used as drug carriers. Meanwhile, it was proven that the type of the hydrophobic substituents did not influence the release of Dox. Therefore, cholesterol was chosen as an ideal hydrophobic substituent for the formation of NPs. However, it was by then still unclear, how much and which type of cholesterol should be used, and what mesoscopic structure the self-assembled NPs has.

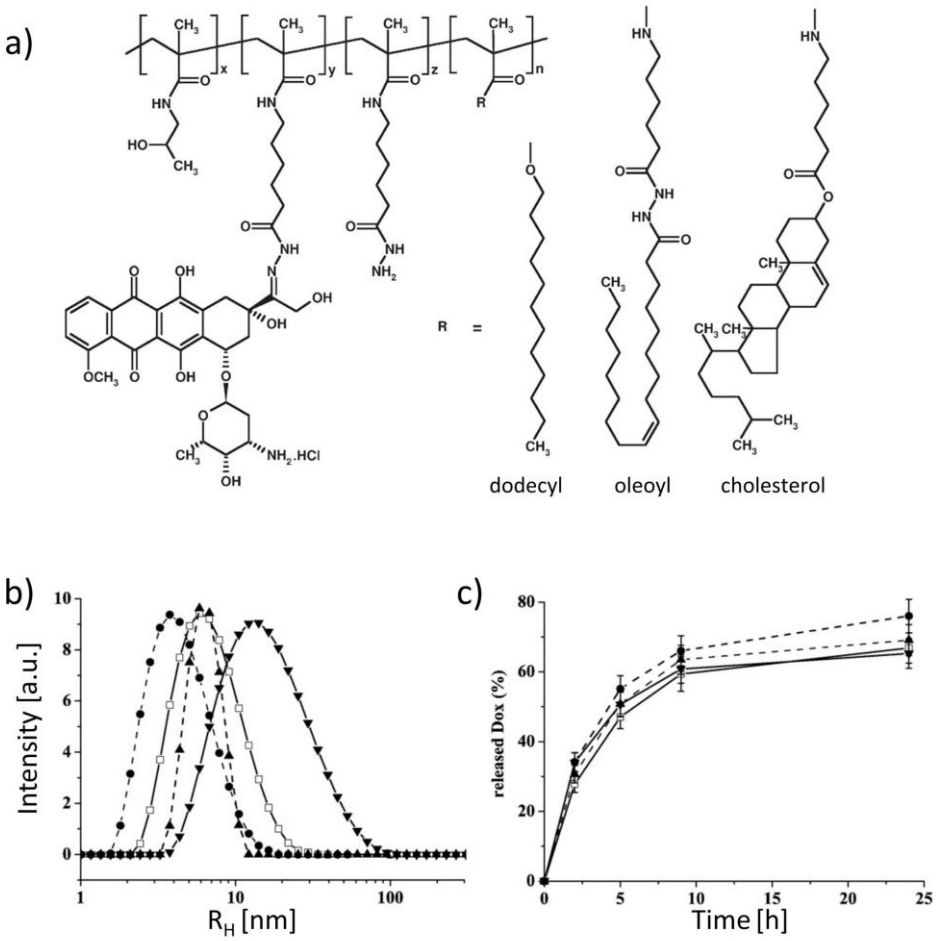

Figure 3.2: (a) Chemical structures of the *p*HPMA copolymers bearing dodecyl, oleoyl and cholesterol groups. Dox is connected to the polymer backbone through a pH-cleavable hydrazone bond. (b,c) Size distribution of (b) and release of Dox from (c) the *p*HPMA copolymers bearing hydrazide groups (●), dodecyl (□), oleoyl (▲) and cholesterol (▼). Adapted from ref. 9 with permission from Elsevier.

To answer these questions, Filippov led a study on a similar *p*HPMA system having cholesterol groups using fluorescence correlation spectroscopy (FCS) and small-angle X-ray scattering (SAXS).[10] It was found, that in aqueous solution, elongated nanoparticles (NPs) are formed by self-assembly of the cholesterol moieties above the critical micelle concentration (CMC). These cholesterol moieties are located in the core of the NPs, which is surrounded by a shell formed by *p*HPMA chains (Figure. 3.3 inset). Based on static light scattering (SLS) data, an optimal cholesterol content was found at 2.1 mol% (Figure. 3.3).

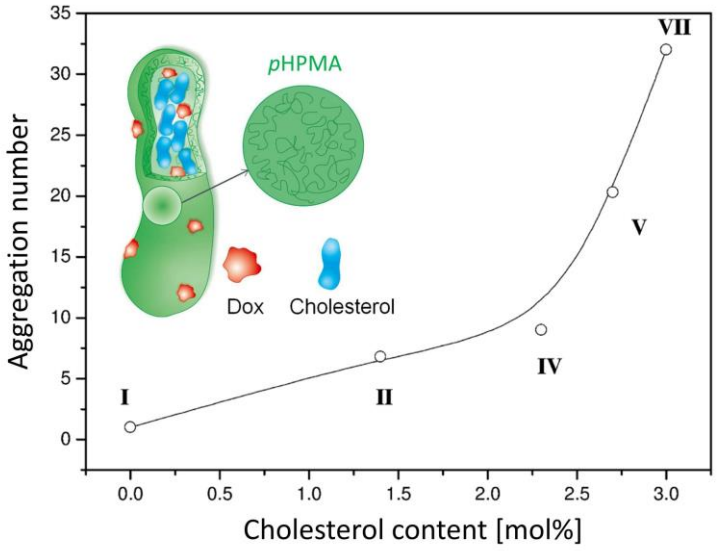

Figure 3.3: Dependence of the aggregation number of the *p*HPMA NPs (without Dox) on the cholesterol content. Inset: Suggested structure of the *p*HPMA NPs as indicated by SAXS data. Adapted from ref. 10 with permission.

In a subsequent study, the release kinetics of the anti-cancer drug Dox from the *p*HPMA NPs in response to pH changes was investigated in dependence on cholesterol content and type using time-dependent SAXS and SANS.[11] In this study, both Dox and Cholesterol moieties were bound to the *p*HPMA backbone via a pH-cleavable hydrazone bone. A pH jump was induced by adding HCl to the solutions of the NPs, to simulate the NP being transported from blood (pH = 7.4) to a tumor environment (pH = 5.0). For all the four *p*HPMA NPs differing in the cholesterol derivative, it was observed, that a vast majority of Dox was released from the NPs in the first 12 h after the pH jump. It is also worth noting that the size of the NPs did not shrink, but instead increased during 12 h, when the cholesterol derivative 5α-cholestan-3-one was used. This phenomenon was attributed to the accumulation of cleaved cholesterol moieties in the hydrophilic shell of the NPs. In contrast, the cholesterol derivative cholest-4-en-3-one does not escape from the hydrophobic core due to its conjugated double bonds. This study shed more light on the role of the hydrophobic substituent and revealed the release kinetics of Dox from the *p*HPMA NPs. Last but not least, the results indicated that the size of the NPs may no longer be well controlled when the cholesterol moieties are bound via a cleavable hydrazone bond. Covalently bound cholesterol moieties are thus better suited for fundamental studies.

In 2017, controlled radical RAFT polymerization was for the first time used to synthesize the *p*HPMA copolymers bearing cholesterol moieties, resulting in much lower polydispersities (from ca. 1.8 using free radical polymerization to ca. 1.2 using RAFT polymerization), hence

better defined systems.[107] The size and CMC of the *p*HPMA NPs were investigated in dependence on the molar mass, cholesterol content and chain architecture (random or block) of the copolymers. It was found, that the CMC depends mainly on the cholesterol content, whereas the chain architecture, namely block or random, neither alters the CMC nor the size of the NPs.

Meanwhile, similar *p*HPMA copolymers synthesized by RAFT polymerization were used in the present study, where these copolymers were mixed with proteins from human blood plasma, as a first step towards a more realistic environment.

3.2. General ideal of the present study

The previous chapter gave an overview on the *p*HPMA based drug delivery system investigated in buffered aqueous solutions. However, additional aspects must be evaluated before application: When the NPs are injected into the human blood vessels, (i) the strong dilution of the polymer may destabilize the structure of the NPs; (ii) hundreds of different types of proteins are present and may interact with the NPs by adsorbing onto the surface of the NPs,[108] and (iii) the adsorption of proteins may lead to their denaturation, such as unfolding, which depends on the concentration of the NPs.[13] Therefore, investigations in blood environment are of great interest. Uncountable therapeutic studies using drug delivery systems on laboratory animals were reported, however, to the best of our knowledge, only partial studies addressed the interaction mechanism in dependence on protein type and concentration have been attempted.[25, 79] Moreover, blood proteins–which differ in their structure and function–may continuously associate with the NPs and subsequently be replaced by other proteins being present at lower concentrations or having slower exchange rates (the Vroman effect, see Chapter 2.3.1.),[25, 78, 80] resulting in an extremely complex situation. Therefore, experiments, where the effect of a single protein species is studied, are more appropriate to further the knowledge.

The key role of interactions between proteins from human plasma and various types of NPs has emerged in the last two decades.[12, 15, 79, 102, 109] For instance, the interaction between plasma proteins and latex NPs was investigated in dependence on the surface hydrophobicity of the NPs. It was reported, that the amount of adsorbed proteins decreases with decreasing surface hydrophobicity.[109] Other studies have addressed self-assembled micelles (NPs) from amphiphilic block copolymers.[110, 111] The self-assembled micelles from the block copolymer *p*nBA-*b*-*p*AA (*p*nBA and *p*AA stand for poly(*N*-butyl acrylate) and poly(acrylic acid)) and the thermo-responsive block copolymer *p*nBA-b-*p*NIPAM-COOH (*p*NIPAM stands for poly(*N*-*iso*-propylacrylamide)) were investigated in the presence of lysozyme, and the core-shell micelles (having a *p*AA or a *p*NIPAM shell) were observed to form complexes with lysozyme, which accumulates in the hydrophilic shell of the micelles. A recent study addressed a new drug delivery system based on the copolymer poly(2-oxazoline), which features excellent biocompatibility.[112] In aqueous solutions, the copolymers self-assembled into micelles, which formed larger aggregates, the size of which was found to be temperature-dependent. In solutions of bovine serum albumin (BSA), it was found that accumulation of BSA occurred due to hydrophobic interaction between the hydrophobic domain of the copolymeric aggregates and

the protein.[113] These studies indicate that the hydrophobicity of the outer part of the self-assembled NPs plays a vital role in the interactions between NPs and proteins.

As for the NPs which are potential candidates for drug delivery, the hydrophobic core is admittedly of great importance because it is commonly used for encapsulation of hydrophobic drugs.[72, 114-116] On the contrary, fewer efforts were made in understanding the role of the hydrophilic shell, which is supposed to make the NPs water-soluble. Moreover, the shell may suppress binding of proteins during the drug transport to the target. Finally, the question arises how thick the hydrophilic shell has to be to accomplish this task and which type of the hydrophilic monomer is appropriate: Despite a high fraction of the hydrophilic content in the copolymeric NPs, strong binding may still occur. This is shown in a study where copolymer NPs composed of NIPAM and *N*-*tert*-butylacrylamide (BAM) were investigated in dependence on their composition in solutions of HSA.[79, 80] Strong protein adsorption was observed even at a fraction of hydrophilic NIPAM as high as 85 wt%. For drug delivery, binding of blood proteins and the formation of a protein corona can have strong effects: The overall size of the NP may increase in an unpredictable way, which hinders their uptake by tumors. This phenomenon was, for instance, reported by Hemmelmann et al.:[103] Self-assembled NPs from the random copolymer *p*(HPMA-co-lauryl methacrylate) were observed to aggregate strongly in the presence of lipid proteins. However, the aggregation was completely hindered when the NPs were loaded with a hydrophobic drug, namely domperidone (Dom). Furthermore, if the protein corona is dense, it may hinder the drug release. Therefore, in the present study, it is of interest to what extent proteins bind to the *p*HPMA NPs which contain a very high fraction of the hydrophilic *p*HPMA, and in which way protein binding is altered by the presence of Dox in the *p*HPMA shell.

In this work, we focus on the interactions between the NPs based on *p*HPMA copolymer having cholesterol side groups, and HSA, which is the most abundant protein in human blood plasma. HSA has the vital function of transporting hydrophobic ligands, e.g. lipids, hormones and cholesterol.[117, 118] Thus, it is of interest in which way HSA interacts with the NPs containing cholesterol. We use synchrotron SAXS and isothermal titration calorimetry (ITC) to investigate the morphology of the NPs and their structural changes due to interactions with HSA in dependence on their respective concentrations in a wide range in PBS. The polymer concentration is chosen above the CMC, which was determined recently using fluorescence correlation spectroscopy (FCS).[107] The observed binding from SAXS and ITC, if there is any, will be further analyzed using fluorescence methods, in which the respective components, i.e.

the NPs and HSA, are fluorescence labeled and can thus be distinguished, as a complementary to SAXS results, in which these components cannot be resolved due to overlap of scattering curves in the observation window.

The results contribute to an understanding of the interaction between *p*HPMA-based NPs and HSA. Furthermore, based on these results, our present work is devoted to propose general rules for designing future polymeric NPs for drug delivery in humans.

3.3. Strategy for the present study

As discussed in the previous chapter, the focus of the present study is to investigate the behavior of the *p*HPMA NPs in the presence of HSA, which is a complex system consisting of at least two components: the *p*HPMA NPs and HSA. In addition, complexes may form by the NPs and HSA, which would result in a third component.

To investigate a complex system with up to three components, appropriate methods must be chosen carefully, so that each component can still be distinguished and analyzed independently of the presence of other components. Now let us call the *p*HPMA system component A, and HSA component B. When A forms a complex with B:

$$A + B \leftrightarrow [A'] + [B'] \leftrightarrow [\mathrm{A'B'}] + Q \tag{3.1}$$

A' and *B*' are the modified *A* and *B* species after the complex formation, respectively. *Q* is the heat released upon formation of the complex [*A*'*B*']. For clearness, it is schematically presented in Figure 3.4.

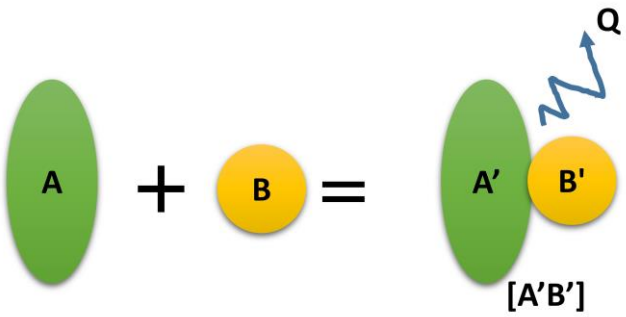

Figure 3.4: Illustration of the complex system under investigation in the present study. *A* and *B* stand for the *p*HPMA NPs and HSA, respectively, whereas *A*' and *B*' denote the modified *A* and *B* in a formed complex [*A*'*B*']. Q is the heat released upon formation of the complex [*A*'*B*'].

Given all probable elements which are involved in the complex formation, the following questions arise in the present study:

- *Are [A'B'] complexes formed?*

To verify the formation of [*A*'*B*'], methods which are sensitive to morphological changes are required, such as small-angle X-ray scattering (SAXS). In case of the formation of [*A*'*B*'], the mixed solutions of *A* and *B* give scattering curves that can never be modeled by a sum of the curves of the pure *A* and *B*. However, this method may reach its limit when the abundance of

[*A*'*B*'] is very low, since the scattered intensities of different components overlap in the whole *q* range. Therefore, we exploit the factor *Q*, which is directly proportional to the total number of [*A*'*B*'], and does not depend on its abundance. A direct measurement of *Q* is realized through isothermal titration calorimetry (ITC).

- *Are the original components altered after the complex formation (A=A' and B=B')?*

It is undoubtedly challenging to characterize a complex system, where appropriate labelling and masking methods are usually employed to distinguish the behavior of the individual components (*A*' and *B*' in the presence of *A*, *B* and [*A*'*B*']). Several attempts were made in the present study: An additional fluorescent dye was bound to the NPs covalently to label them for fluorescence spectroscopy. HSA is fluorescence labelled due to its intrinsic fluorescence emission. Moreover, a small-angle neutron scattering (SANS) experiment was carried out, where the NPs were masked by matching the scattering length density (SLD) of the solvent to the one of the NPs.

Polymers which meet the requirements of the above-proposed methods were synthesized by Dr. Petr Chytil at the Institute of Macromolecular Chemistry, Prague. Their characteristics are given in the next section.

3.4. System under investigation

The characteristics of the polymer samples used for the present study are compiled in Figure 3.5 and Table 3.1. The content of hydrazide groups about 5 mol% was found as sufficient for attachment of about 10 wt% of anthracyclines or other anticancer drugs by pH-sensitive hydrazone bond.[119]

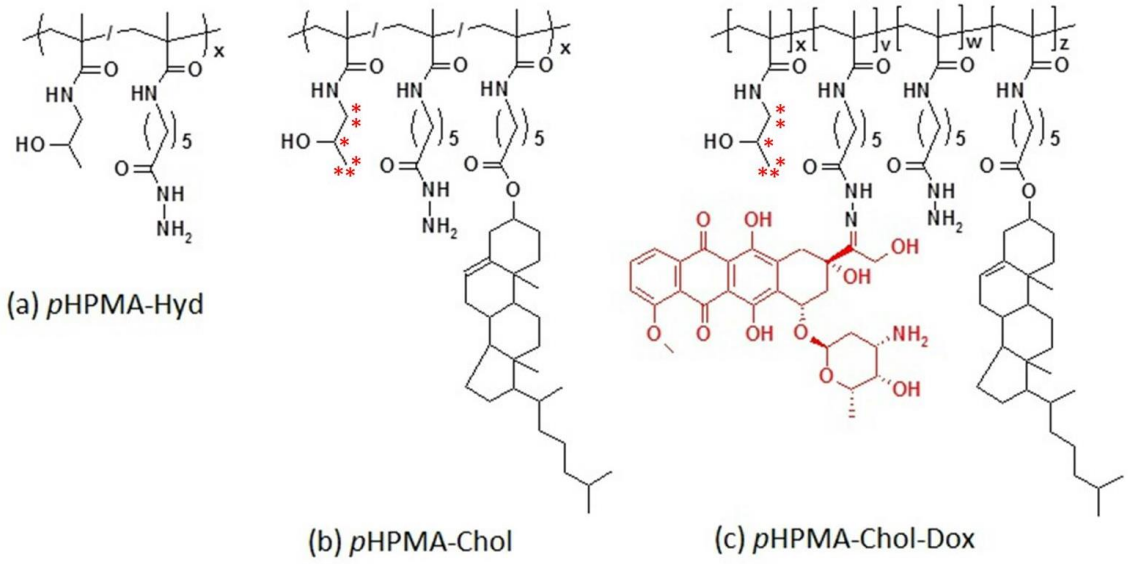

Figure 3.5: Schematic structures of polymer samples. (a) Cholesterol-free *p*HPMA-based copolymers bearing hydrazides groups randomly distributed along the polymer chain (***p*HPMA-Hyd**). (b) Cholesterol-containing *p*HPMA-based copolymers (***p*HPMA-Chol**). The cholesterol side groups are randomly distributed along the polymer chain. (c) Cholesterol-containing *p*HPMA-based copolymers carrying the anti-cancer drug Dox (***p*HPMA-Chol-Dox**). The red stars in (b) and (c) mark the deuterated position in the cases of *p*HPMA-Chol-d6 and *p*HPMA-Chol-Dox-d6.

For FLCS measurements, the fluorescence labelled amphiphilic copolymer (*p*HPMA-Chol*) was synthesized (Figure 3.6). The molecular weight and dispersity of *p*HPMA-Chol* could not be determined due to the presence of the dye and its interference with the laser of the multiangle light scattering detector. However, since the refractive index chromatogram of *p*HPMA-Chol* is similar to that of *p*HPMA-Chol, we do not expect differences in M_w, M_n and $Đ$, and used the same values for the calculation of molar concentrations of *p*HPMA-Chol and *p*HPMA-Chol*.

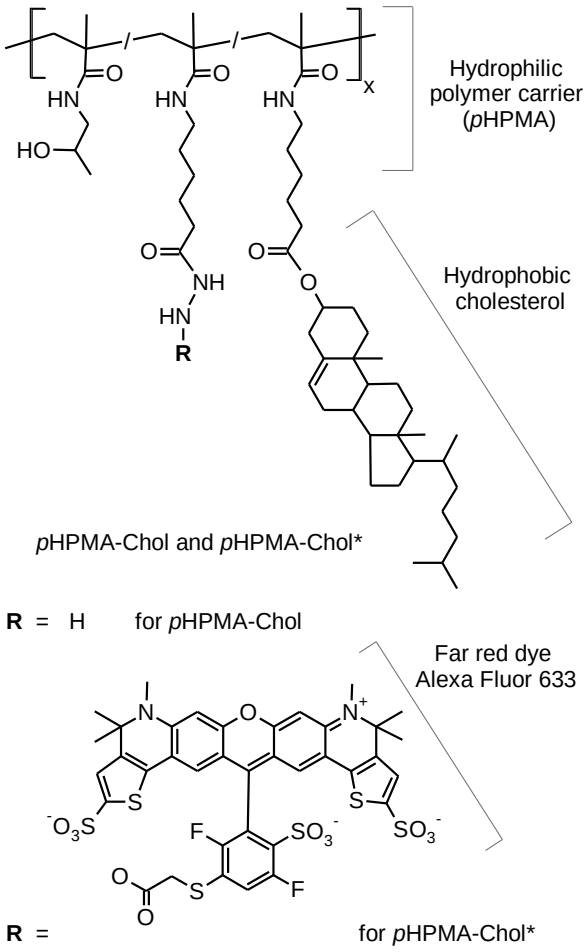

Figure 3.6: Schematic structures of the copolymer containing cholesterol groups randomly distributed along the polymer chain (*p*HPMA-Chol) and its fluorescence labelled analogue (*p*HPMA-Chol*).

Table 3.1. Characteristics of the copolymer samples

Sample	M_w (g·mol^{-1}) [(a)]	$Đ$ [(b)]	Cholesterol content (mol %) [(c)]	Dox content (wt %) [(d)]
*p*HPMA-Hyd	41800	1.29	0	0
*p*HPMA-Chol-1	33290	1.16	2.1	0
*p*HPMA-Chol-2	28600	1.15	2.1	0
*p*HPMA-Chol-Dox-1	50000	1.39	2.1	6.0

*p*HPMA-Chol-Dox-2	43500	1.17	2.1	6.3
*p*HPMA-Chol-Dox-3	41500	1.11	2.1	7.9
*p*HPMA-Chol-d6	30500	1.11	2.1	0
*p*HPMA-Chol-Dox-d6	35300	1.09	2.1	7.3
*p*HPMA-Chol*	-	-	2.1	0

Human serum albumin (HSA) is the most abundant protein found in human blood plasma, with a molar mass of 66500 g mol^{-1}. The physiological range of HSA in blood is 35–52 mg mL^{-1}.[120] Its crystal structure is known as "heart shaped" (Figure 3.7). HSA has important functions in transporting substances in human body, such as fatty acids, lipids, lipase and hydrophobic drugs.[16-24] For our research, two types of HSA of different purity grade were purchased from Sigma Aldrich: (i) HSA[i], lyophilized powder, 97%; (ii) HSA[ii], lyophilized powder, 99%, fatty acid free, globulin free.

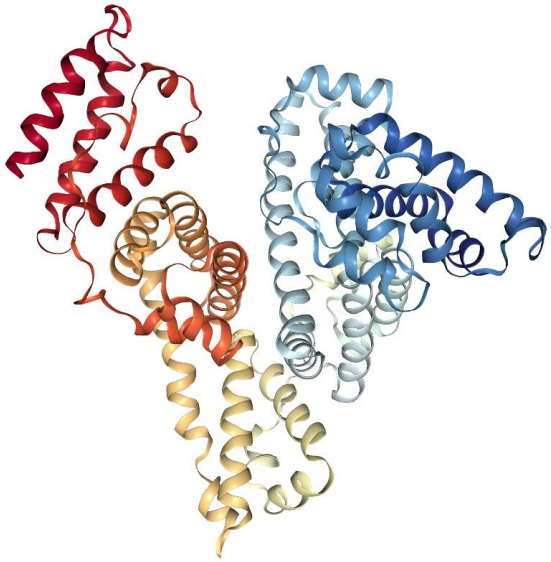

Figure 3.7: Crystal structure of HSA based on the crystal structure 1e78 from protein data bank.[121, 122]

4. Characterization techniques

4.1. Small-angle scattering

This chapter is based on ref. 123.

X-ray and neutron scattering are both very powerful methods for studying the structure of particles in a continuous medium. X-ray photons and neutrons both interact with atoms in the sample, but with the difference that X-rays interact with the electrons and neutrons with the nuclei. Although the physics of X-ray and neutron scattering is different, they can be described by the same mathematical model. Therefore, to best understand these two techniques, we discuss them in this chapter together starting with basic theoretical aspects.

4.1.1. Elastic scattering of X-ray and neutrons

To understand the elastic scattering of X-ray and neutrons, which carries the structural information on the sample, we consider in the following both X-ray photons and neutrons as waves. The wavelengths of X-rays are given by $E = hc/\lambda$, whereas the wavelengths of neutrons are given by de Broglie's relationship, $E = h^2/(2m_n \lambda^2)$ with m_n the mass of a neutron. For structural investigations, relatively hard X-rays (λ about 0.10–0.15 nm) and thermal neutrons (λ about 0.10–1.0 nm) are normally used.

The elastic scattering of X-ray photons or neutrons is illustrated in Figure 4.1. The distance between the scatterers in the sample, r, is typically in the nanometer range, and the wavelength of the X-ray or neutron radiation is even smaller. A 2D detector is typically placed at a distance of several meters to the sample, to record the scattered intensity. This geometry leads to a Fresnel number much larger than unity, and the incident and scattered waves can thus be considered as planar waves. As a result, the two scatterers become sources of spherical waves which have the same modulus as the incident one; only the direction of the incident wave is altered by 2θ. $\vec{\boldsymbol{q}}$ is the momentum transfer, which is the difference between the scattered wave, $\overrightarrow{\boldsymbol{k'}}$, and the incident wave, $\vec{\boldsymbol{k}}$. The modulus of $\vec{\boldsymbol{q}}$ is given by:

$$q = \frac{4\pi}{\lambda} sin\theta \tag{4.1}$$

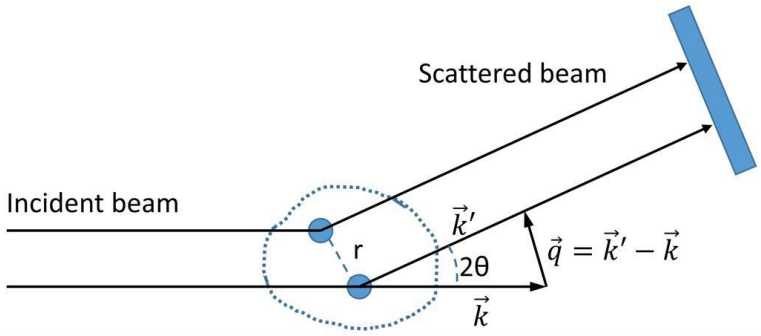

Figure 4.1: Schematic representation of elastic scattering. The incident beam is scattered by two scatterers through the angle 2θ at a distance r. The scattered waves have the same wavelength as the incident beam and are thus capable of interfering in a detector.

4.1.2. Scattering cross-section and scattering length

We use the so-called differential scattering cross-section to describe the strength of the interaction between the incident beam and the sample (Figure 4.2). The differential scattering cross-section is defined as the ratio between the scattered energy/(unit solid angle × unit time) and the incident energy/(unit area × unit time), which gives the dimensions of an area.

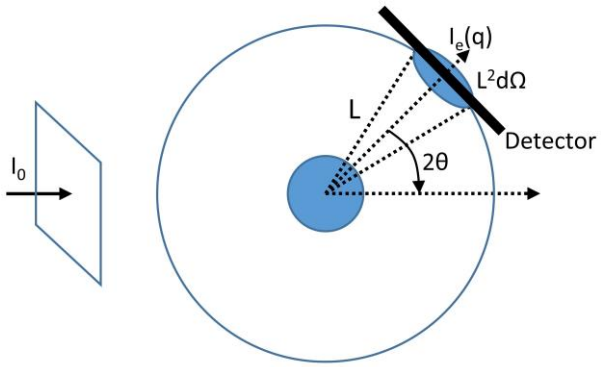

Figure 4.2: Schematic representation of the scattering cross-section. $I_e(q)$ and I_0 are the scattered beam and the incident beam, respectively, the ratio between which has the dimension of an area. L is the sample-detector distance.

Now we assume that there are N scatterers at positions $\boldsymbol{r}_i$ ($1 \leq i \leq N$), which coherently scatter. The total scattering amplitude is the sum of the individually scattered waves. The total scattered amplitude can be expressed as:

$$A(\boldsymbol{q}) = \sum_{i=1}^{N} b_i \exp(i\boldsymbol{q} \cdot \boldsymbol{r}_i) \tag{4.2}$$

where b_i is called the scattering length, and has the dimension of length (normally expressed in cm). The exponent term is called the phase factor. This equation elucidates an important concept in small-angle scattering of both X-rays and neutrons: The scattering amplitude is the Fourier transform of the distribution of the scatterers. If these N scatterers have random orientations, the phase factor is rewritten as:

$$\langle \exp(i\boldsymbol{q} \cdot \boldsymbol{r}_i) \rangle = \frac{\sin(qr)}{qr} \tag{4.3}$$

$\langle \cdots \rangle$ denotes the spherical average.

The case discussed above is based on discretely distributed scatterers. It is in many cases more convenient to use a continuous distribution of the scattering length, $\rho(\boldsymbol{r})$, which is called the scattering length density and represents the total scattering length per unit sample volume. For an atom with radial electron density $\rho(r)$, its atomic X-ray scattering length can be written as:

$$b_x(q) = 4\pi r_0 \int \rho(r) r^2 \frac{\sin(qr)}{qr} dr \tag{4.4}$$

r_0 is the scattering length of a single electron, i.e. 2.82×10^{-13} cm. Note that $\lim_{x\to 0} (\sin(x)/x) = 1$; thus, the scattering length in the forward direction ($q = 0$) is Zr_0, where Z is the atomic number. Equation 4.4 expresses two important points: (i) X-rays interact more strongly with heavier atoms than with lighter ones. (ii) The X-ray scattering length is wavelength-independent. Although the latter one is invalid when the X-ray wavelength is close to the absorption edge of the atom (anomalous scattering), this special case is not relevant for this work and will not be discussed further.

Neutrons interact with the nuclei instead of with electrons. The neutron scattering length consists two terms, namely the nuclear potential term and the nuclear spin term, hence $b_n = b_p + b_s$. It is important to note that none of these quantities increases regularly with atomic number, which differs strongly from the case of X-rays. Instead, b_p depends strongly on the isotopic composition. Therefore, in structural studies of biological systems containing mainly lighter atoms e.g. H (D), C, O, and N, neutrons are often more sensitive than X-rays (Table 4.1). Moreover, the neutron scattering length may even be negative, e.g. for deuterium. This feature of neutron scattering length is extensively exploited in structural studies of soft matter, enabling investigation methods, such as contrast variation (solvent matching),[124-128] which was also used in this research and will be discussed further in Chapter 5.

Table 4.1: X-ray and neutron scattering lengths of atoms that are often seen in biological systems. Adapted from ref. 123.

Atom	**H**	**D**	**C**	**N**	**O**
Atomic mass	1	2	12	14	16
Number of e^-	1	1	6	7	8
b_x, 10^{-12} cm	0.282	0.282	1.69	1.97	2.16
b_n, 10^{-12} cm	-0.374	0.667	0.665	0.940	0.580

4.1.3. Contrast variation

As discussed in the previous chapter, small-angle scattering originates from either difference in electron density in case of X-rays, or difference in neutron scattering length density (SLD). For macromolecules in solution, the difference between the scattering length of the particle and that of the solvent having equivalent volume, is called the excess scattering length density, $\Delta\rho(\boldsymbol{r}) = \rho(\boldsymbol{r}) - \rho_s$. The scattering amplitude given by equation 4.2 can thus be rewritten as:

$$A(\boldsymbol{q}) = \int_V \Delta\rho(\boldsymbol{r}) exp(i\boldsymbol{q}\cdot\boldsymbol{r})\, d\boldsymbol{r} \tag{4.5}$$

V is the volume of the particle. Experimentally, one cannot directly measure $A(\boldsymbol{q})$ because it is a complex number. Instead, one measures the scattered intensity which is a product of $A(q)$ and its complex conjugate $A^*(q)$. For a monochromatic incident beam, the intensity is equivalent to the number of photons or neutrons being scattered in the direction 2θ per unit time and unit area. The general expression of the scattered intensity with respect to the excess scattering length density is given by Stuhrmann and Kirste[124]:

$$I(q) = (\Delta\rho)^2 I_C(q) + 2\Delta\rho I_{CF}(q) + I_F(q) \tag{4.6}$$

Where $I_C(q)$, $I_F(q)$ and $I_{CF}(q)$ are the scattering from the particle, fluctuations of scattering length density around its average value, and the cross-term. These quantities can be experimentally determined by variations of $\Delta\rho$, which is normally realized by changing the H/D ratio of the solvent in a SANS experiment.

When investigating multi-component systems using SANS, it is also possible to "mask" specific component of the particle, by matching the scattering length density of the solvent to the one of the component that needs to be hidden, i.e. $\Delta\rho = 0$ for the hidden part (Figure 4.3). This way, only the remaining part of the particle contributes to the total scattered intensity, and the scattering pattern carries only the structural information of this remaining part. In practice, this is usually realized by mixing H_2O and D_2O in the solvent at a predefined ratio. Due to the fact that the scattering length densities of most biological macromolecules lie between the one of H_2O and D_2O (Table 4.1), an appropriately mixed solvent can contrast match most biological systems.

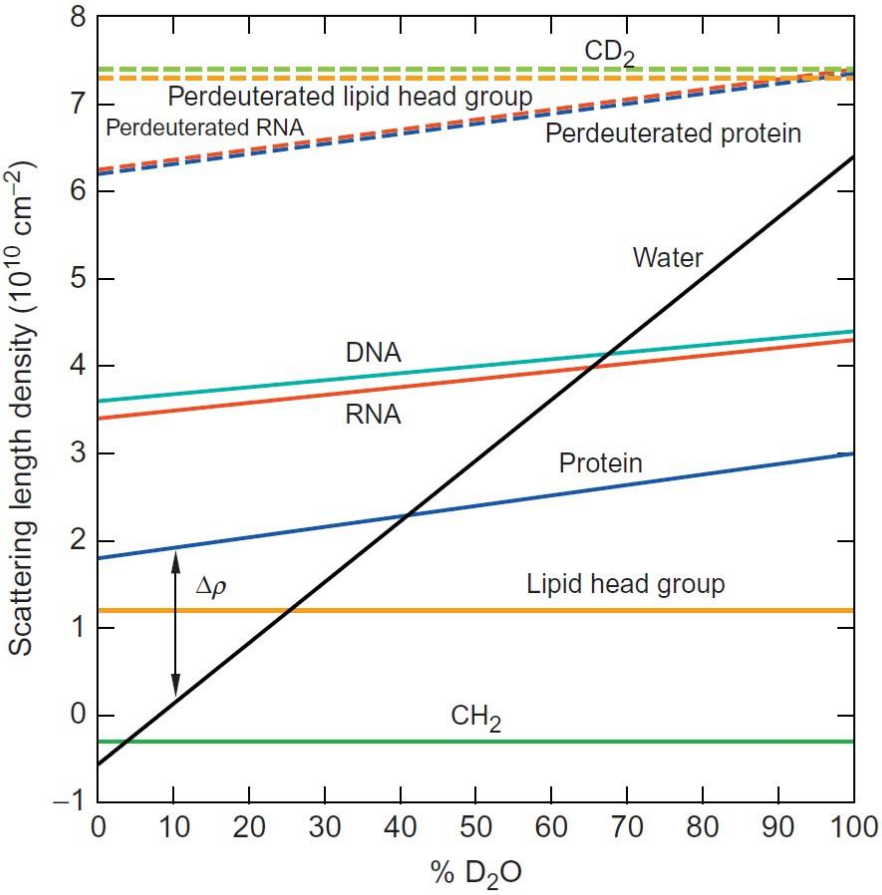

Figure 4.3: Average scattering length density of some important biological macromolecules as a function of D_2O content (vol %) in the solvent. The arrows mark the matching conditions for the respective macromolecules. Taken from ref. 129 with permission from Elsevier.

4.1.4. Instruments and protocol

4.1.4.1. Instruments and protocol of SAXS measurements

SAXS measurements were performed at the high brilliance synchrotron beamline P12 at the European Molecular Biology Laboratory (EBML) at DESY, Hamburg.[130]

In biological SAXS experiments, sample loading and subsequent cleaning of the exposed capillary are normally time-consuming, which has been a bottleneck towards efficient use of beamtime. At P12, extremely fast manipulation of samples is realized through a fully automated robotic sample changer, which is programmed for each measurement in the following sequence (Figure 4.4): (a) cleaning of the capillary where the sample is exposed to X-ray; (b) transport of the predefined next sample to the capillary; (c) opening of the shutter; (d) flow of the sample through the capillary to minimize radiation damage; (e) Collection of data including sample scattering images, beam intensity and transmission, etc.; (f) closing of the shutter; (g) removal of the exposed sample. The programming of sample sequence, and the corresponding loading volume, flow speed, exposure time etc. is integrated in the user interface BECQUEREL.

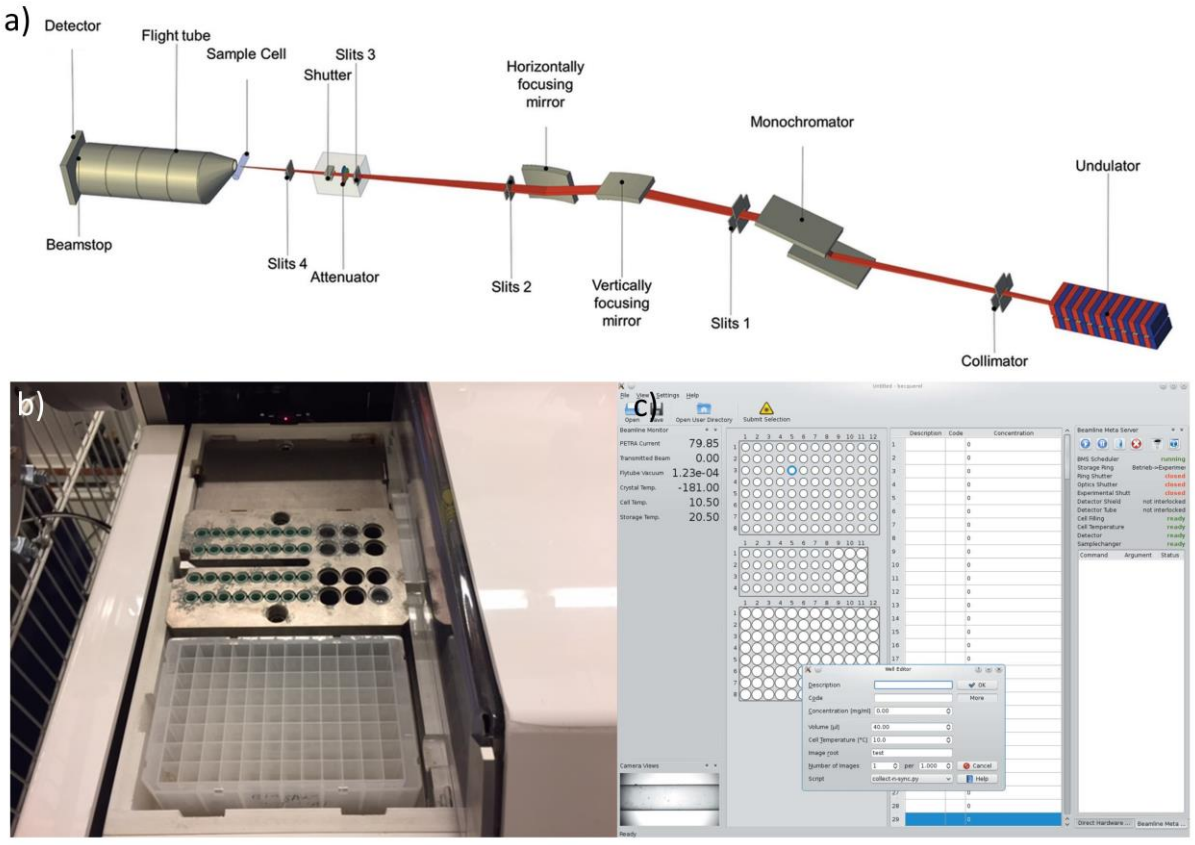

Figure 4.4: (a) Schematic representation of the components of the P12 beamline. Taken from ref. 130. (b) The automated robotic sample changer, having arrays of sample positions. (c) A screenshot of the user interface BECQUEREL. Taken from ref. 130.

The X-ray wavelength was λ = 1.24 Å. A 2D Pilatus 2M detector was placed at a sample-detector distance of 3.00 m, resulting in a q range of 0.003–0.5 $Å^{-1}$. 20 frames having exposure times of 45 ms were measured as 50 µL solution flowed through a quartz capillary within the exposure time. The sample volume exposed to the X-ray beam is thus unchanged from sample to sample. Radiation damage was excluded by comparing these frames and by keeping only those where no damage was evident. These were azimuthally integrated and averaged, resulting in scattering curves $I(q)$ vs q. The background from PBS buffer and the quartz capillary was subtracted using the program AUTOSUB,[131, 132] after normalization of the scattering curves to their respective transmissions and exposure times. The corresponding scattering curves were then normalized by their concentrations.

The noisy data points at both very low q values and very high q values were discarded, resulting in a valid q range of 0.005 - ca. 0.3 $Å^{-1}$. All measurements were performed at 37 °C, mimicking physiological body temperature. The modeling of SAXS curves was performed using the NCNR package in the Igor Pro environment[133] and the Oligomer software in the ATSAS 2.6.0 package.[134]

The time-resolved SAXS experiments were carried out at P12 using the same instrument setup as described above. Prior to SAXS measurements, a droplet (16.6 µL) of 1 M HCl was added to the solutions of 2 mL volume, to change the pH from 7.4 to ca. 5. This defined the time zero, and SAXS measurements were started. The amount of the required HCl solution was calibrated by titrating 1 M HCl to PBS. For each sample, a total number of 34 SAXS measurements were carried out in a 14 hour period, within which, a 15 min interval was used in the first 180 min, followed by a 30 min interval till the end of the measurement. The same procedures as described above were used for the raw data treatment, namely the radiation damage check, the 2D data reduction and the background subtraction.

4.1.4.2. Instruments and protocol of SANS measurements

SANS experiments were carried out at KWS-1 (Figure 4.5), which is a high-resolution SANS instrument thanks to its neutron velocity selector with $\Delta\lambda/\lambda$ = 10%. The accessible wavelengths of the incident neutrons can be chosen between 4.5 and 42 Å. Neutron beam is collimated in a 20 m-long collimation line, which consists of 18 carriages (a 1 m-long neutron guide of 50 ×

50 cross section) and five active apertures, which are positioned at 2, 4, 8, 14 and 20 m from the sample. The scattered beam is recorded by a position sensitive ^{6}Li scintillation detector with a 64 × 64 cm^2 area.

A neutron wavelength of 5 Å was used. All samples were measured at sample-detector distances (SDDs) of 1.5 m, 4 m and 14 m, with the corresponding exposure times of 1800 s, 3600 s and 11500 s, respectively, resulting in a *q*-range of 0.004-0.3 Å^{-1}. All samples were measured in Hellma cells (2 mm sample thickness) at 37 °C. Boron carbide was used for measurement of the dark current, poly(methyl methacrylate) for the detector sensitivity and calibration of intensity. The scattered 2D images were azimuthally integrated and averaged, and subsequently corrected for the background from the same sample cell with PBS buffer with the software QtiKWS provided by JCNS.

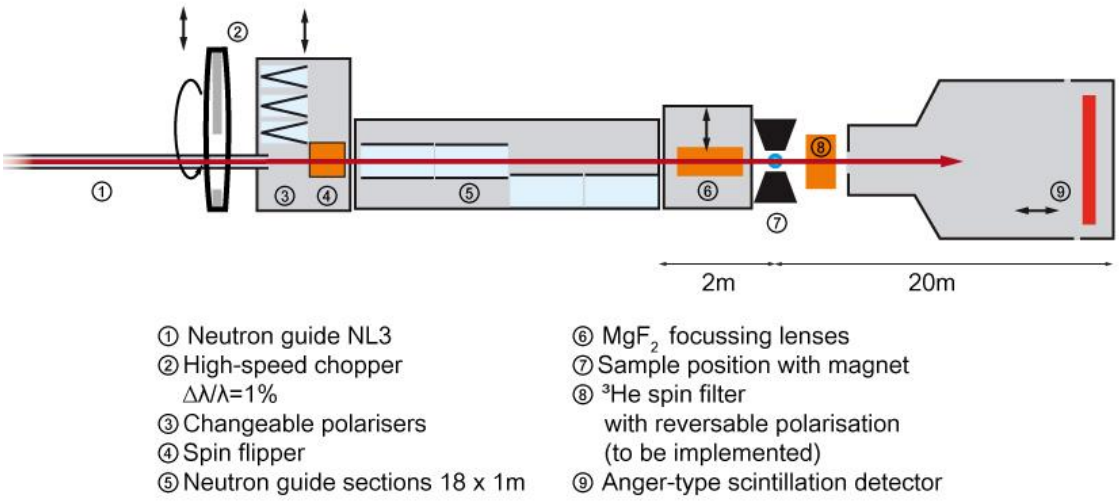

Figure 4.5: Schematic representation of the instruments at the KWS-1 beamline. Taken from ref. 135.

4.1.5. Data analysis

4.1.5.1 Modeling of the mixed solutions of the NPs and HSA

The SAXS curves from the mixed solutions were fitted by a linear combination of two terms, i.e. the scattering from *p*HPMA-Chol-1 or *p*HPMA-Chol-Dox-1 and from HSA, with the same concentrations as in the mixtures. The following expression was fitted by ignoring the cross-terms:

$$I(q) = \nu_{HPMA} I_{HPMA}(q) + \nu_{HSA} I_{HSA}(q) \quad (4.7)$$

where ν_{HPMA}, ν_{HSA}, $I_{HPMA}(q)$ and $I_{HSA}(q)$ denote the volume fractions ($\nu_{HPMA} + \nu_{HSA} = 1$) and the scattering intensities of the individual components, i.e. of the polymer solution (*p*HPMA-Chol-1 or *p*HPMA-Chol-Dox-1) or of HSA.

Given the fact that the exposed sample volume in the X-ray experiment, V_{exp}, is constant, the volume fraction of HSA is given by:

$$\nu_{HSA} = \frac{\frac{c_{HSA} \cdot V_{exp}}{\rho_{HSA}}}{\frac{c_{HPMA} \cdot V_{exp}}{\rho_{HPMA}} + \frac{c_{HSA} \cdot V_{exp}}{\rho_{HSA}}} = \left(1 + \frac{c_{HPMA}}{c_{HSA}} \cdot \frac{\rho_{HSA}}{\rho_{HPMA}}\right)^{-1} \quad (4.8)$$

where c_{HPMA} and c_{HSA} denote the concentration of the polymer and HSA, respectively. ρ_{HPMA} and ρ_{HSA} are the mass densities of the *p*HPMA system (with or without Dox) and HSA. Their values are not a priori known, and their ratio was determined in the fits of equation 4.8 to the scattered intensity of the mixed solutions.

4.1.5.2. Modeling of the scattering from HSA

The radius of gyration, R_g, of HSA was determined by fitting the Guinier approximation:

$$I(q) = I_G \, exp\left(\frac{-R_g^2 q^2}{3}\right) \quad (4.9)$$

where I_G is a scaling factor. At this, only data points which meet the condition $qR_g \leq 1.24$ were used to ensure a good approximation.

4.1.5.3. Modeling of the scattering from the NPs

The modeling of the scattering from the NPs require a proper form factor, which describes their overall shape and size, together with a structure factor describing the correlation of the polymer chains.

As discussed in Chapter 2, amphiphilic copolymers may self-assemble into various structures in aqueous solutions, e.g. spheres, cylinders, ellipsoids, etc. Among these structures, sphere is the most commonly seen structure, since it has the lowest surface-to-volume ratio among all 3D configurations for a given volume, which is in favor of minimizing the free energy of the system. The form factor for a monodisperse spheres is given by:

$$P_S(q) = 3\left[\frac{sin(qr) - qrcos(qr)}{(qr)^3}\right] \quad (4.10)$$

where *r* denotes the radius of the spherical particle. Figure 4.6a illustrates the scattered intensity profile of spherical particles with various sizes. The distribution of the particle size is often

modeled by the Schulz distribution, which describes moderately polydisperse systems. It is given by:[136]

$$G(r_c) = \frac{r_c^Z}{\Gamma(Z+1)}\left(\frac{Z+1}{\bar{r}_c}\right)^{Z+1} \times exp\left[-\frac{r_c}{\bar{r}_c}(Z+1)\right]. \quad (4.11)$$

where $\bar{r}_c$ is the mean value of the particle size and Z is a parameter related to the polydispersity σ_c with the expression:

$$\sigma_c = \left(\frac{1}{Z+1}\right)^{\frac{1}{2}} \quad (4.12)$$

$\Gamma(Z+1)$ is the gamma function:

$$\Gamma(t) = \int_0^\infty x^{t-1}e^{-x}dx \quad (4.13)$$

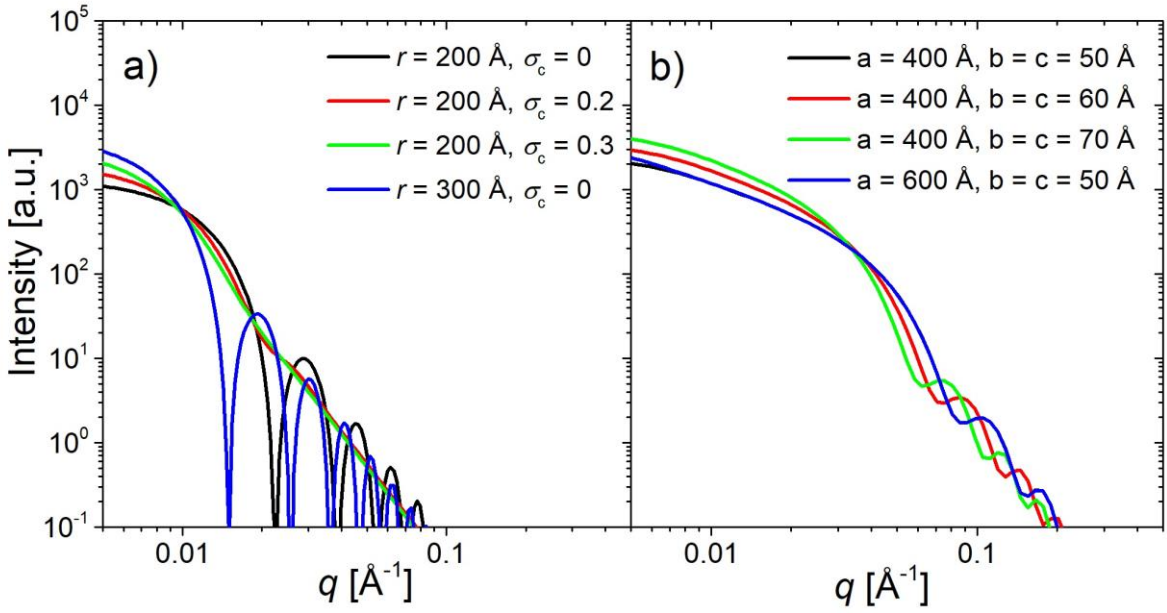

Figure 4.6: Representative plot of scattering curves of spherical (a) and ellipsoidal (b) particles. The geometry of the particles is given in the figure: (a) *r*: radius of the sphere. σ_c: polydispersity. (b) *a*: semi-major axis. *b* and *c*: semi-minor axes.

The best fits of the SAXS curves of the *p*HPMA system are obtained by the form factor of monodisperse ellipsoidal particles, $P_{ell}(q)$ (Figure 4.6b):[137]

$$P_{ell}(q) = \frac{1}{V_{ell}}\int_0^1\int_0^1 \Phi^2\left\{q\left[a^2cos^2\left(\frac{\pi x}{2}\right) + b^2sin^2\left(\frac{\pi x}{2}\right)(1-y^2) + c^2y^2\right]^{\frac{1}{2}}\right\}dxdy \quad (4.14)$$

where V_{ell} is volume of the ellipsoidal particle. a, b and c are three semi-axes of the ellipsoidal particle with the condition $a \geq b \geq c$. To simplify the fitting model, the condition $b = c$ was used for all scattering curves. The function Φ(x) is defined as:

$$\Phi(x) = 3\left(\frac{\sin x - x\cos x}{x^3}\right) \tag{4.15}$$

The radius of gyration of the ellipsoid, R_g, is given by:[137]

$$R_g = \left(\frac{a^2+b^2+c^2}{5}\right)^{\frac{1}{2}} \tag{4.16}$$

The scattering from concentration fluctuations of the swollen *p*HPMA chains located in the shell of the NPs was modeled by the Ornstein-Zernike structure factor:[138]

$$S_{OZ}(q) = \frac{I_{OZ}}{1+(\xi q)^2} \tag{4.17}$$

I_{OZ} is a scaling factor, and ξ represents the range of spatial correlations of concentration fluctuations.

4.2. Isothermal Titration Calorimetry

This chapter is based on ref. 139.

For almost three decades, isothermal titration calorimetry (ITC) has been a routinely used method for investigating molecular interactions, e.g. ligand binding of biochemical reactions.[32] In a typical ITC experiment, the interaction is triggered by changing the chemical composition of the system through incremental titration of a ligand. Therefore, the initial concentration of the ligand is an independent variable which is controlled experimentally. As a standard procedure in ITC data analysis, the measured reaction heat is plotted against the ligand concentration, which carries information including the binding constant, stoichiometry, etc.

4.2.1. Principle of ITC

The components of a typical power compensation ITC are illustrated in Figure. 4.7 There are two identical cells (the reference cell and the sample cell) surrounded by an adiabatic shield. Prior to titration of ligand, a constant power is applied to the reference cell. A feedback power is applied to the sample cell, so that the temperature difference between the two cells, ΔT, is kept constantly at zero.

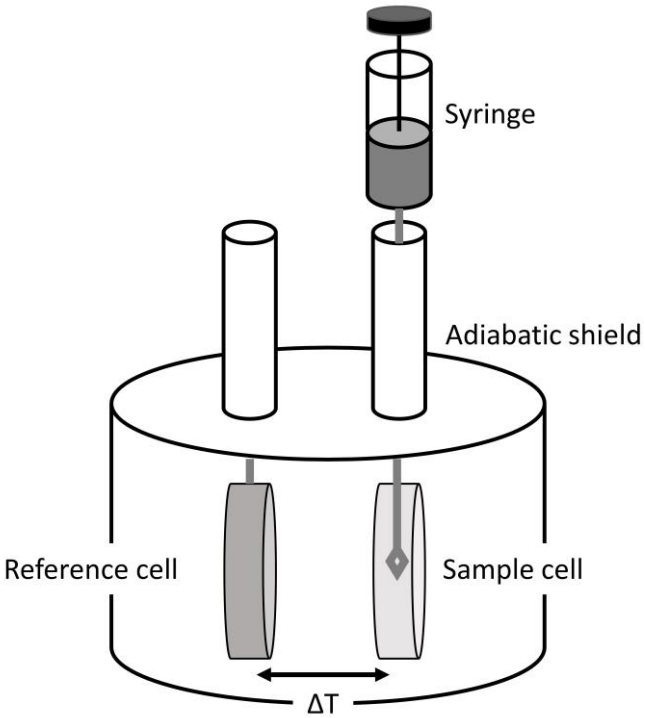

Figure 4.7: Representative illustration of a typical instrument for ITC. A sample cell and a reference cell are placed in an adiabatic shield. A syringe is used to titrate ligand into the sample

cell. Normally, there is a stirrer at the tip of the needle of the syringe, which rotates and mixes the titrated ligand with the sample.

Upon titration, the heat input (positive or negative) resulting from the molecular interaction is sensed and the feedback power applied to the sample cell increases or decreases, such that ΔT always remains zero (Figure 4.8a). The raw signal in this case is the power applied to the sample cell that is required to keep ΔT at zero. The interaction heat (Figure 4.8c) can then be calculated by integrating the feedback power over the time with respect to a baseline value (Figure 4.8b), which was calculated using the software NICPIC. An elaborate description of the computational method of the baseline is given in ref. 140.

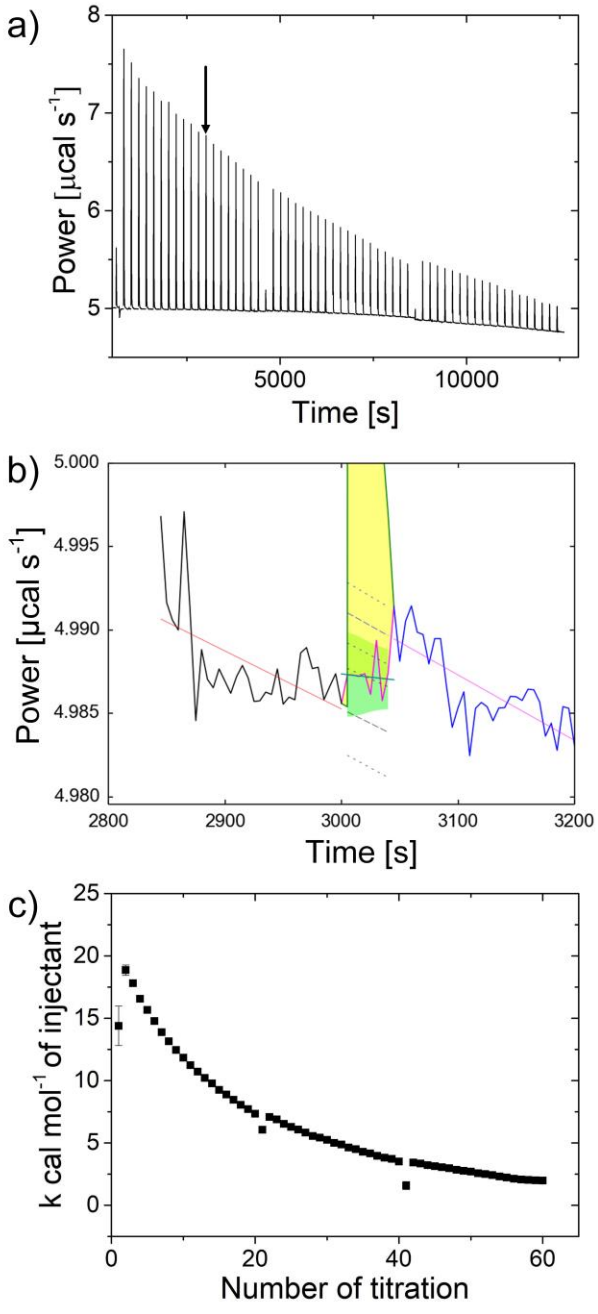

Figure 4.8: Exemplary ITC data representation. (a) Power peaks plotted against time. The arrow marks the 13th titration peak. Its baseline computational method, which is integrated in the NITPIC software, is shown in (b): Black and blue lines: Experimental before- and after-injection baselines. The calculated before- and after-injection baselines are shown as red lines. The dark green line underneath the peak is the calculated baseline for integration, the area of which is marked in yellow. The green areas at the bottom of the peak are related to the error of the integration, which is determined by extrapolations of the red lines. These extrapolations are shown as dashed lines. Further explanations of all legends are given in ref. 140. (c) Resulting titration enthalpy by integrating the peaks in (a) according to their baselines, respectively. The three data points, which deviate from the curve, are due to unavoidable experimental errors in a typical ITC measurement.

4.2.2. Thermodynamics of ITC measurement

This chapter is based on ref. 139.

In terms of biochemistry and biophysics, the ligand refers to molecules, e.g. substrate, inhibitor, drug, protein, which noncovalently interact with a specific site of another molecule, which act as a receptor for the ligand (Figure 4.9).

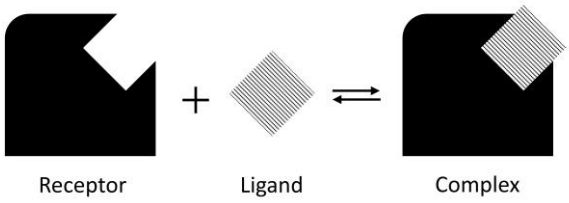

Figure 4.9: Representative illustration of a ligand binding reaction.

Obviously, there are three species in equilibrium in ligand binding. The equilibrium association constant, K_a, is given by:

$$K_a = \frac{[Complex]}{[Receptor][Ligand]} = \frac{1}{K_d} \tag{4.18}$$

[···] denotes the molar concentration of the species. K_d is the equilibrium dissociation constant. The two equilibrium constants are related to the Gibbs energy of binding, ΔG_b, through:

$$\Delta G_b = -RTlnK_a = RTlnK_d = \Delta H - T\Delta S \tag{4.19}$$

where T is the absolute temperature and R the gas constant. ΔH and ΔS denote the enthalpy and entropy change, respectively. Obviously, the larger the association constant, the smaller the dissociation constant, hence a more negative Gibbs energy of binding is obtained, referring to the formation of a more stable complex.

4.2.3. Instrument and measurement protocol

ITC measurements were performed using a MicroCal 200 isothermal titration calorimeter. The experiment was performed by consecutively injecting a concentrated HSA solution into the calorimeter cell, which contained 280 µL of the polymer solution of either *p*HPMA-Chol-2 or *p*HPMA-Chol-Dox-1. The HSA solution was mounted in a 40 µL injection syringe, the tip of which was modified by a stirrer. The injection volume was 2 µL, and the time between two injections was 150 s or 200 s, with an additional 200 s initial delay. The stirring speed was 750 rpm. The dilution of HSA (blank titration) was measured by titrating HSA into PBS buffer using the above-mentioned setups.

To cover a wide concentration range, the HSA concentration in the syringe was chosen as high as possible, so that a wide concentration range can be covered. Therefore, the concentration was chosen at 50 mg mL^{-1}, which is close to the upper limit of the physiological value (52 mg mL^{-1}).[120] The polymer concentration in the cell was chosen at 1 mg mL^{-1}, which is safely above the CMC and correlates with typical polymer doses in drug delivery. The titration series described above was repeated 3 times in a row for each sample as well as for the blank: After each titration series, the empty syringe was refilled by HSA solution at 50 mg mL^{-1}. In the meantime, the excessive solution in the cell was removed to reset the sample volume in the cell to be again 280 µL. Then, the next titration was started. At this, a final HSA concentration of ca. 16 mg mL^{-1} was reached in the cell. Each peak in the raw thermogram was integrated, and the dilution experiment (blank) was subsequently subtracted point by point. As usual, the first peak of each of the three titration series was discarded, since its value was always influenced by unavoidable experimental errors. All the data were recorded at 37 °C and were analyzed using the NITPIC software.[140]

4.3. Fluorescence lifetime correlation spectroscopy

Fluorescence correlation spectroscopy (FCS) is a well-established technique for characterizing NPs and a large variety of biomolecules, based on their diffusion behavior.[141-144] In FCS experiments, a fluorescent dye is associated with the investigated particle, either chemically or physically, e.g. through the hydrophobic effect. From the autocorrelation function of the time-resolved fluorescent signal from the dye, its diffusion behavior – and thus the one of the particle – is characterized in detail. However, FCS is limited with regard to the following aspects: (i) It cannot probe a system where, apart from the dye used as a label, another component is also fluorescent, if their emission spectra overlap, which leads to a complex autocorrelation function. This addresses the case where the fluorescence labelled *p*HPMA NPs are investigated in solutions of HSA, which is fluorescent as well. (ii) The afterpulsing of the detector and the inevitable fluorescence background contaminate the time-resolved intensity profile. Even though the contribution of afterpulsing can be suppressed to a large extent by cross correlating the signal of two detectors, into which the signal is fed simultaneously, the fluorescence background is still present.

Fluorescence lifetime correlation spectroscopy (FLCS) has been shown to offer new solutions to these problems.[145] FLCS makes use of the lifetime decay properties of different fluorescent species to eliminate the afterpulsing and the background and to separate FCS autocorrelation functions for samples containing more than one fluorescent species. The lifetime analysis can be included into traditional confocal FCS instruments provided that a pulsed laser is in use.[145-147] In recent years, FLCS has demonstrated its great potential in studying, among others, NPs,[148] lipid bilayers[149] and the dynamics of DNA chains.[150] Here, it was used to distinguish HSA and the fluorescence labeled *p*HPMA NPs in solutions using their different lifetims.

Figure 4.10 shows a typical setup for a confocal FCS. A laser beam is focused by a microscope objective to a very tiny volume inside the sample, which is called the confocal volume having a typical volume of the order of several femtoliters. Due to Brownian motion, fluorescent particles enter the confocal volume and are excited by the laser, emitting a fluorescence signal. These emitted fluorescence light is collected by the same objective and passes through a dichroic mirror and an emission filter. A confocal pinhole is used to block the fluorescence light from regions outside the confocal volume, and the remaining fluorescence signal is detected by a single photon counting device, namely an avalanche photo diode (APD).

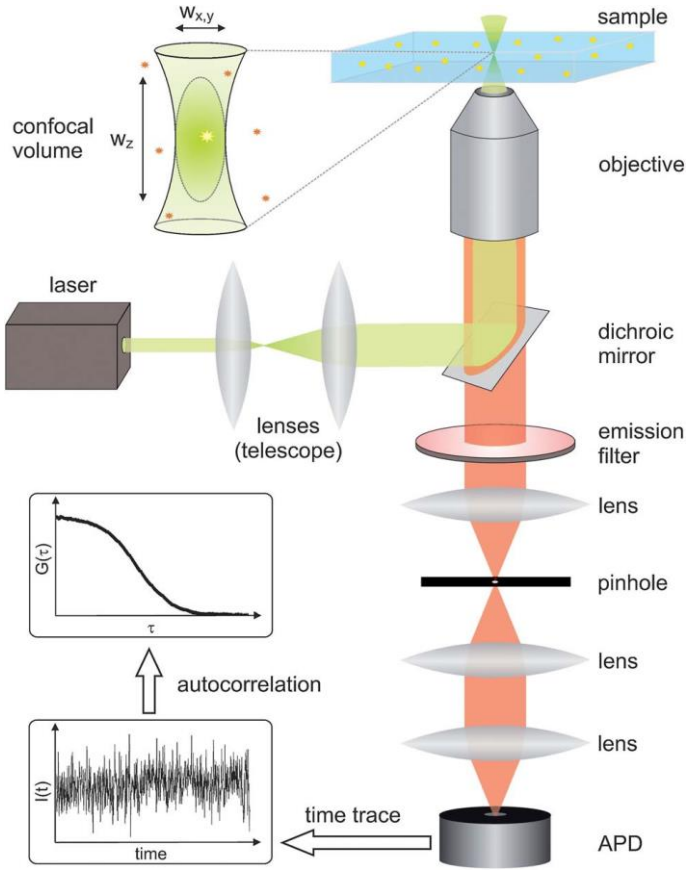

Figure 4.10: Schematic illustration of a confocal FCS. Reproduced from ref. 144 with permission from the Royal Society of Chemistry.

The fluctuations of the fluorescence intensity versus time, which are caused by diffusion of the fluorescent species through the confocal volume, are characterized by an autocorrelation function:

$$G(\tau) = \frac{\langle \delta I(t) \cdot \delta I(t+\tau) \rangle}{\langle I(t) \rangle^2} = \frac{\langle I(t) \cdot I(t+\tau) \rangle}{\langle I(t) \rangle^2} - 1 \tag{4.20}$$

Here $\delta I(t) = I(t) - \langle I(t) \rangle$ and $\langle \cdots \rangle$ denotes the time average. In the following, we discuss the working principle of fluorescence lifetime correlation spectroscopy, which is derived from a normal confocal FCS and is able to distinguish different fluorophores by making in addition use of their lifetimes. Therefore, we start with lifetime of fluorophores in the next chapter.

4.3.1. Quantum yield and fluorescence lifetime

The fluorescence lifetime and quantum yield are regarded as the most important two characteristics of a fluorophore. Here, we use a simplified Jablonski diagram to represent the quantum yield and the lifetime (Figure 4.11).

The fluorescence quantum yield is the ratio of the number of emitted photons and the number of absorbed photons. By defining the emissive rate of the fluorophore, Γ, and its rate of non-radiative decay to the ground state S_0, k_{nr}, the quantum yield is given by:

$$Q = \frac{\Gamma}{\Gamma + k_{nr}} \tag{4.21}$$

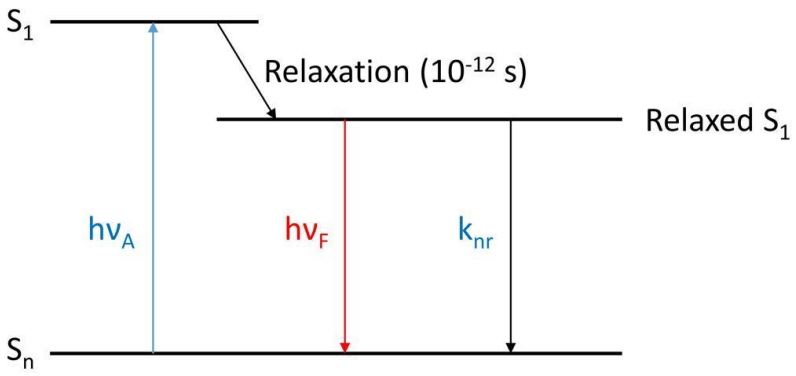

Figure 4.11: A simplified Jablonski diagram. S_n and S_1 denote the ground state and the first excited state. $h\nu_A$ and $h\nu_F$ denote the energy differences of the excitation and the fluorescence, respectively. k_{nr} is the non-radiative decay rate constant. The individual relaxation process resulting in the relaxed S_1 state is not explicitly presented here.

The lifetime of the excited state refers to the average time the molecules stay in the excited state before returning to the ground state. For the case illustrated in Figure 4.11. The fluorescence lifetime is given by:

$$\tau = \frac{1}{\Gamma + k_{nr}} \tag{4.22}$$

In the absence of non-radiative processes, the lifetime becomes:

$$\tau_n = \frac{1}{\Gamma} \tag{4.23}$$

τ_n is called the intrinsic or natural lifetime.

Normally, the fluorescence intensity decays exponentially. The fluorescence decay of a single exponential mode is described as:

$$I(t) = I(0) \cdot \exp(-\frac{t}{\tau}) \tag{4.24}$$

$I(t)$ and $I(0)$ denote the fluorescence intensity at a given time, t, and the one measured directly after the excitation, respectively. $I(t)$ is also called a lifetime decay pattern. In practice, equation

4.24 is usually rewritten as a sum of multiple exponential decays to determine the fluorescence lifetime experimentally, which will be discussed further in Chapter 4.5.4.

4.3.2. Principle of fluorescence lifetime correlation spectroscopy

This chapter is based on ref. 151.

To understand the working principle of FLCS, we compare it with a conventional FCS which was described at the beginning of Chapter 4. FCS gives a standard result–the autocorrelation function of the intensity fluctuations, using a continuous laser excitation and single channel detection. In FLCS, the excitation is a pulsed laser instead, and there are two independent timings recorded for each detected photon's arrival time: A macroscopic and a microscopic one. The macroscopic arrival time refers to the same one as measured in a conventional FCS, which is the arrival time of the detected photon on a microsecond scale, with respect to the beginning of the experiment. The microscopic arrival time is the time difference between the detection and the latest laser pulse, which carries information on the fluorescence decay on a nanosecond scale. These two independent timings enable FLCS to separate autocorrelation functions of a component with specific lifetime.

We will discuss FLCS using a simple example where two fluorescent components with different lifetimes, A and B, are diffusing in a system. After each laser pulse, the nanosecond time scale is binned into channels encoded by the channel number, *i*, which typically ranges up to 100–1000. The overall lifetime decay curve of the mixture of A and B can be obtained by histogramming the frequency of various channel numbers, which is illustrated in Figure 4.12a.

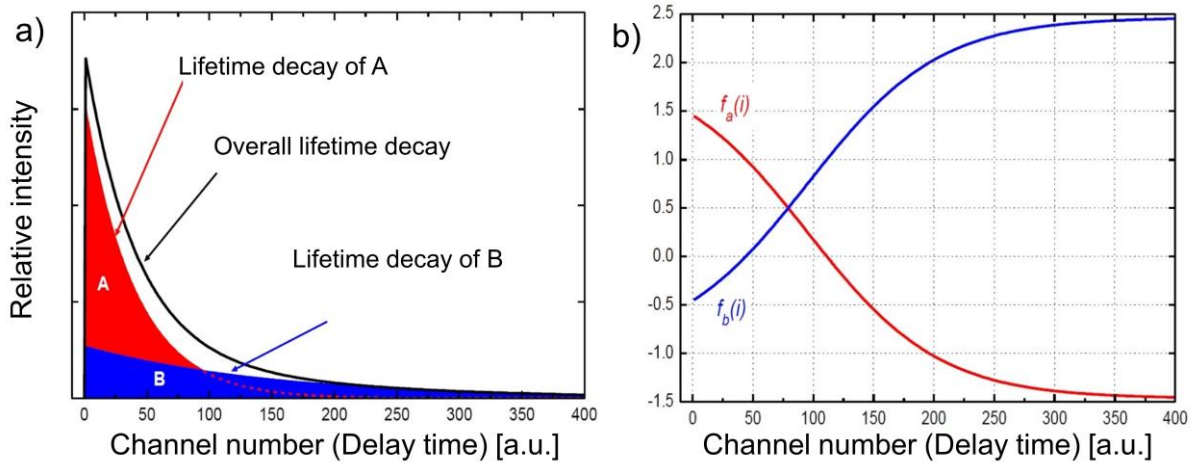

Figure 4.12: (a) Illustration of a histogram of a system where two fluorescent components, A and B, are present. The channel number is equivalent to the delay time on nanosecond scale

(see text). The 0 channel denotes the end of the laser pulse. (b) Filter functions calculated from the lifetime decay of A and B and the overall lifetime decay in (a). These functions are used to separate autocorrelation functions of A and B. Adapted from ref. 151 with permission from Springer Nature.

Now we assume that the lifetime decays of the pure components A and B are a priori known by reference measurements on pure A and B, individually. We denote these intensity decays as $A(i)$ and $B(i)$, where i is again the channel number. We normalize $A(i)$ and $B(i)$ by $a(i)= A(i)/\Sigma A(i)$, $b(i)= B(i)/\Sigma B(i)$, so that $\Sigma a(i) = \Sigma b(i) = 1$. These normalized lifetime decays are intensity-independent and are thus called decay patterns. The experimentally measured overall decay curve, $D(i)$, can then be described as a sum:

$$D(i) = w_a \cdot a(i) + w_b \cdot b(i) \tag{4.25}$$

where w_a and w_b are the number of photons emitted by A and B, respectively. We can now define two digital filter functions, $f_a(i)$ and $f_b(i)$, which will be used subsequently to separate the autocorrelation functions of component A and B, respectively. The filter functions fulfill the following expression:

$$\langle \sum f_a(i) \cdot D(i) \rangle = w_a, \ \langle \sum f_b(i) \cdot D(i) \rangle = w_b \tag{4.26}$$

$\langle \cdots \rangle$ denotes averaging over an infinite number of measurements. As indicated by the above expression, the digital filter functions act as weighting functions. By applying them to the overall decay curve $D(i)$, one obtains the number of photons contributed by A and B, respectively.

These filter functions can be numerically calculated using matrix calculations:

$$\begin{matrix} f_a(i) \\ f_b(i) \end{matrix} = \left(\begin{bmatrix} a(i) \\ b(i) \end{bmatrix} \cdot D \cdot \begin{bmatrix} a(i) \\ b(i) \end{bmatrix}^T \right)^{-1} \cdot \begin{bmatrix} a(i) \\ b(i) \end{bmatrix} \cdot D \tag{4.27}$$

D is a diagonal N×N matrix calculated from the corresponding values of $D(i)$:

$$D = \begin{bmatrix} \frac{1}{D(1)} & \cdots & 0 \\ \vdots & \ddots & \vdots \\ 0 & \cdots & \frac{1}{D(N)} \end{bmatrix} \tag{4.28}$$

The obtained filter functions are illustrated in Figure 4.12b. Finally, the separated autocorrelation functions for components A and B are given by:

$$G_a(\tau) = \frac{\langle \sum_i f_a(i) D(i,t) \cdot \sum_i f_a(i) D(i,t+\tau) \rangle}{\langle \sum_i f_a(i) D(i,t) \rangle^2} - 1$$

$$and\ G_b(\tau) = \frac{\langle \sum_i f_b(i)D(i,t) \cdot \sum_i f_b(i)D(i,t+\tau) \rangle}{\langle \sum_i f_b(i)D(i,t) \rangle^2} - 1 \quad (4.29)$$

4.3.3. Instrument and data analysis

FLCS measurements of the *p*HPMA-Chol-2/HSA mixed solutions were performed using a confocal laser scanning microscope Olympus IX83 (Olympus Corporation, Japan) extended by the FLIM/FLCS upgrade kit and the SymPhoTime64 software (PicoQuant GmbH, Berlin, Germany). For all measurements, a Plan Apochromat 60x (NA 1.20) water immersion objective was used. The fluorescence lifetime properties were obtained using a pulsed laser head having a wavelength of 640 nm and a pulse frequency of 40 MHz. The laser was coupled into a polarization-maintaining single-mode optical fiber. The system was controlled by a PicoHarp 300 unit using a time-correlated single-photon counting (TCSPC) protocol with a time resolution per channel of 4 ps. The detection unit consisted of two hybrid PMA detectors with a quantum yield of 45 % (at 500 nm). A bandpass filter at 690 ± 35 nm was mounted in front of the detector to suppress the fluorescence emission from HSA. The confocal volume was calibrated by measuring the fluorescent dye Atto655, the diffusion coefficient of which is known to be 426 ± 8 $\mu m^2\ s^{-1}$.[152]FLCS measurements of the *p*HPMA-Chol-Dox-2/HSA mixed solutions were performed using the same setup as described above.

For measurements of the mixed solutions, a droplet of solution (70 µL) was placed on a cover glass. For the *p*HPMA-Chol-2/HSA mixed solutions, each sample was measured 7 times for 600 s. For the *p*HPMA-Chol-Dox-2/HSA mixed solutions, each sample was measured for 300 s. The autocorrelation functions were calculated by excluding the time period, in which high intensity peaks originating probably from aggregates of dyes, were present. Moreover, autocorrelation functions, which deviated strongly, or which were not smooth at high correlation times, were discarded. The remaining autocorrelation functions were fitted one by one, as described below, and the resulting hydrodynamic radii were averaged. The background and detector afterpulsing were eliminated by applying a digital filter, which was generated separately using the lifetime decay pattern of the respective mixed solutions, to the autocorrelation function.

The selection of the time period for calculation of the autocorrelation function was used as implemented in the software SymPhoTime64. The obtained autocorrelation functions were fitted using the following function:

$$G(\tau) = \left\{1 + T\left[\exp\left(-\frac{\tau}{\tau_{trip}}\right) - 1\right]\right\} \times \frac{1}{N}\sum_{i=0}^{n_D-1} \frac{\rho_i}{\left(1+\frac{\tau}{\tau_{D,i}}\right)\left(1+\frac{\tau}{\tau_{D,i}\kappa^2}\right)^{1/2}} \quad (4.30)$$

N is the average number of fluorescent molecules inside the confocal volume. n_D refers to the number of fluorescent species having different diffusion times, which is denoted as $\tau_{D,i}$ for the i-th species. ρ_i is the fraction of the i-th species, and κ the structure factor, which is the height-to-width ratio of the confocal volume. κ was determined in a reference measurement of the fluorescent dye Atto655 in water, which has a diffusion coefficient of 426 ± 8 $\mu m^2\ s^{-1}$ at 25 °C.[152] T and τ_{trip} are the triplet fraction and time of the dye AF633, and have the value of 0.281 and 5.7 µs, respectively. These values were determined by a reference measurement of a pure solution of the dye AF633 at 10^{-8} M.

D_i, the diffusion coefficient of species i, is given by:

$$D_i = \frac{{\omega_0}^2}{4\tau_D}, \text{ with } \omega_0 = \left(\frac{V}{\kappa}\right)^{\frac{1}{3}}\pi^{-0.5} \quad (4.31)$$

V is the confocal volume which was determined together with κ in the reference measurement. The hydrodynamic radius R_H of each type of fluorescent particles was calculated using the Stokes-Einstein relation:

$$R_H = \frac{k_B T}{6\pi\eta D_i} \quad (4.32)$$

where k_B is Boltzmann's constant, T the absolute temperature, and η the viscosity of the solvent.

The lifetime decay patterns of HSA, the dye AF633, and their mixed solutions were measured using the same setup as used for FLCS measurements (Chapter 6.1). A bandpass filter at 690 ± 35 nm was used.

4.4. Fluorescence quenching

This chapter is based on ref. 153.

Fluorescence quenching is a widely used technique for studying interactions between a fluorophore and ligands which quench the fluorophore. In biophotophysics, fluorescence quenching has become an established method for investigations of the interaction between proteins and other chemical compounds, using the intrinsic fluorescence of the investigated proteins.[154-159] Here, we use it for characterization of the mechanism of the interaction between HSA and the *p*HPMA NPs.

Any process, that reduces the fluorescence intensity of a fluorophore, is called fluorescence quenching. It can result from various molecular interactions, e.g. excited-state reactions, molecular rearrangements, collisions and ground-state complex formation. In addition to these processes, high optical densities or sample turbidity can also reduce fluorescence intensities. However, little molecular information can be obtained from such types of quenching.

Fluorescence quenching has been thoroughly studied as a fundamental physical phenomenon. In practice, it is, however, often used as a mean to characterize molecular interactions in biochemical systems, in which fluorescence quenching usually occurs through two different mechanisms i.e. collisional (dynamic) and static quenching. For collisional quenching, the quencher must diffuse to collide with the fluorophore within the lifetime of its excited state. Upon collision, the excited fluorophore returns to the ground-state with no photon being emitted. In contrast to that, in the case of static quenching, the fluorophore forms a nonfluorescent ground-state complex with the quencher. It is noteworthy that both types of quenching require molecular contact between the fluorophore and quencher, which results in many applications for fluorescence quenching. For instance, quenching experiment can be used to characterize the molecular accessibility of a fluorophore to a quencher. It can also provide quantitative information regarding the local collisional frequency between the fluorophore and quencher when only collisional quenching occurs.

4.4.1. Theory of collisional quenching

Collisional quenching of fluorescence is described by the Stern-Volmer equation:

$$\frac{F_0}{F} = 1 + K_D[Q] = 1 + k_q\tau_0[Q] \tag{4.33}$$

where F_0 and F are the fluorescence intensities in the absence and presence of quencher, respectively. k_q is the bimolecular quenching constant, which is related to the Stern-Volmer

quenching constant K_D through $K_D = k_q \tau_0$, where τ_0 is the lifetime of the fluorophore in the absence of the quencher. [Q] is the molar quencher concentration.

A Stern-Volmer plot is typically used to present quenching data, where F_0/F is plotted versus [Q], because F_0/F should be linearly dependent on [Q] when only collisional quenching occurs. At this, the slope of F_0/F versus [Q] is equal to K_D. If the lifetime of the fluorophore is a priori known, the bimolecular quenching constant can be determined.

The bimolecular quenching constant, k_q, can be understood as the collisional frequency between freely diffusing molecules, namely fluorophores and quenchers. However, it is important to note that k_q only refers to those collisions which result in quenching. The frequency in terms of the total number of collisions is described by the Smoluchowski equation:

$$k_0 = \frac{4\pi RDN}{1000} = \frac{4\pi N}{1000}(R_f + R_q)(D_f + D_q) \tag{4.34}$$

k_0 is the diffusion-controlled bimolecular rate constant. R denotes the collision radius which is usually assumed to be the sum of the molecular radii of the fluorophore (R_f) and the quencher (R_q). D_f and D_q are the diffusion coefficients of the fluorophore and the quencher, respectively. A constant 1/1000 is used to convert molarity to moles per cubic centimeter. The collisional quenching efficiency is thus defined as:

$$f_Q = \frac{k_q}{k_0} \tag{4.35}$$

In practice, it is possible to distinguish collisional quenching from static quenching using their different dependence on temperature: Higher temperature results in faster diffusion of both fluorophore and quencher, thus promoting collisional quenching. On the contrary, if the ground state complex is formed through weak binding between fluorophore and quencher, the complex is likely to be dissociated at higher temperatures, hence weaker static quenching. However, in a system where both collisional and static quenching occur, these two phenomenon may cancel each other, resulting in an ambiguous situation. Therefore, the distinction between collisional and static quenching is preferably through precise measurements of the lifetimes of the fluorophore at different quencher concentrations: If a quenching process is purely collisional, with increasing quencher concentration, the loss in lifetime should follow exactly the trend of the loss in fluorescence intensity. Mathematically this is expressed by (Figure 4.13):

$$\frac{F_0}{F} = \frac{\tau_0}{\tau} \tag{4.36}$$

Normally, if $F_0/F > \tau_0/\tau$ is observed, static quenching occurs in addition to the collisional one.

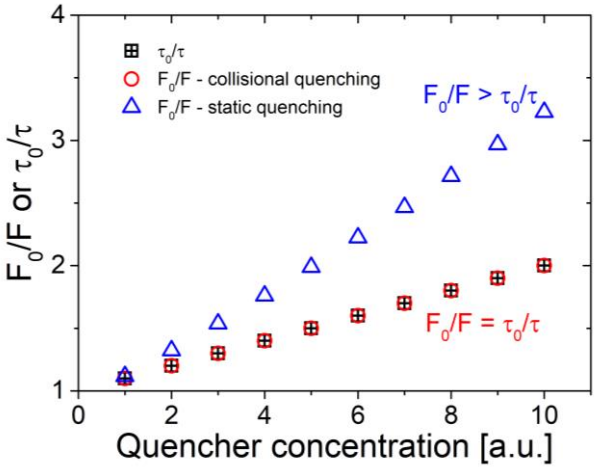

Figure 4.13: Representative illustration of the dependence of F_0/F on quencher concentration in case of collisional and static quenching. The data sets are arbitrarily generated.

4.4.2. Theory of static quenching

Static quenching refers to a process in which a fluorophore forms a ground-state complex with a quencher. When this complex absorbs light, it immediately returns to the ground state without photon emission. Therefore, to derive the dependence of the fluorescence intensity on quencher concentration, we must consider the association constant for complex formation which is given by:

$$K_S = \frac{[F\text{–}Q]}{[F][Q]} \tag{4.37}$$

Where [*F*–*Q*] is the concentration of the complex, [*F*] the concentration of the free fluorophore, and [*Q*] the concentration of quencher. Assuming that the fluorescence intensity is proportional to the fluorophore concentration, and recalling that the total fluorophore concentration equals [*F*] + [*F*–*Q*], Equation 4.37 can be rewritten as:

$$\frac{F_0}{F} = 1 + K_S[Q] \tag{4.38}$$

It is interesting to note that the dependence of F_0/F upon quencher concentration is linear, which is also seen for collisional quenching (Chapter 4.4.1.). Theoretically, a pure static quenching process features $\tau_0/\tau = 1$, that is, the lifetime of the fluorophore does not change with increasing quencher concentration.

4.4.3. Effects of sample geometry

We have discussed the dependence of fluorescence intensity on quencher concentration in both cases of collisional and static quenching. It is thus important to precisely determine the

fluorescence intensities experimentally, using a fluorescence spectrometer. Depending on the light-path of the sample, the main confounding factor in fluorescence quenching, the inner-filter effect, may occur, hampering the precise measurement of fluorescence intensity.

The inner-filter effect refers to a loss in the fluorescence intensity due to the absorbance of the incident light and the emitted light from fluorophore by the quencher molecules. Experimentally, the inner-filter effect is corrected using the empirical correction equation given by:

$$I_{corr} = I_{obs} \times 10^{(\frac{A_{ex}+A_{em}}{2})} \tag{4.39}$$

where I_{obs} is the observed intensity. A_{ex} and A_{em} are the absorbance of the sample at excitation and emission wavelengths, respectively. This equation was often used to correct for sample absorbance.[160-162] Other correction methods were reported, considering different geometries of the cuvettes in use. These methods are, however, difficult to realize experimentally.[163, 164]

4.4.4. Instruments and data analysis

Fluorescence emission measurements were performed using a Cary Eclipse Fluorescence Spectrometer (Varian Inc., Palo Alto, CA, USA). The excitation wavelength was 280 nm, and emission spectra were recorded from 300 nm to 480 nm. The excitation and emission slits were both set to 5 nm. The solutions were mounted in a 10 mm quartz cell (Hellma Analytics). Each measurement was repeated 6 times to detect variation of intensity due to e.g. bleaching. The resulting spectra, which did not deviate from each other in intensity, were averaged. For all measurements, the sample was kept in an isothermal stage at 20 °C, to avoid intensity variations due to e.g. quenching of diffusive oxygen at different temperatures.

UV-Vis absorption spectra were measured using a Specord 205 spectrophotometer (Analytik Jena AG) in the same quartz cell at room temperature. The entrance and exit slits were both set to 1 nm. The scan speed was 50 nm s^{-1}.

As mentioned previously (Chapter 4.4.1), to distinguish the collisional quenching from the static one, the fluorescence lifetime at each quencher concentration must be a priori known, by fitting the lifetime decay pattern of each fluorescent species with a sum of exponential decays:

$$\mathrm{I(t)} = \sum_{\mathrm{i=0}}^{\mathrm{n-1}} \mathrm{A}_i \exp(-\frac{\mathrm{t-t_0}}{\tau_\mathrm{i}}) + I_0 \tag{4.40}$$

I is the fluorescence intensity. A_i denotes the amplitude of each decay, t_0 the beginning of the decay, τ_i the lifetime of each decay, and I_0 the background. To avoid the influence of the laser

pulse shape, t_0 is fixed for all samples at 5.5 ns, which is ca. 1.5 ns after the end of the laser pulse.

The amplitude average lifetime is defined as

$$\langle \tau \rangle_a = \sum a_i \tau_i \tag{4.41}$$

where τ_i denotes the lifetime of each decay mode and a_i the corresponding fraction with $\sum a_i = 1$. In case of a heterogeneous lifetime ($n > 1$ in equation 4.40), τ_0 in equation 4.33 has the value of the amplitude average lifetime given in equation 4.41.

The HSA emission spectra were modeled using a Gaussian function:

$$I = I_0 + \frac{A\, exp(\frac{-4\ln(2)(x-x_c)}{\omega^2})}{\omega\sqrt{\frac{\pi}{4\ln(2)}}} \tag{4.42}$$

where A is the amplitude of the peak, x_c the peak center, ω the full width at half maximum and I_0 a constant.

In a few words, we use SAXS and SANS to characterize the mesoscopic structure of the *p*HPMA NPs in the absence and in the presence of HSA in aqueous solutions. Complex formation, which leads to an altered form factor of the NPs, can be identified by fitting the scattering curves of the mixed solutions by a linear combination of the form factors of the pure NP and HSA. Such complex formation typically results in a heat release, which can be measured by ITC. To reveal the origin of the complexation, fluorescence labeling was used. This way, the NP and HSA can be distinguished in the mixed solutions using FLCS and fluorescence quenching method.

5. Probing interaction between the *p*HPMA NPs and HSA

This chapter is based on ref. 165. Reprinted and adapted with permission. Copyright (2018) American Chemical Society.

To probe the interaction between the *p*HPMA NPs and HSA, a precondition is the constant presence of the self-assembled NPs in the mixed solutions of the NPs and HSA. Therefore, the concentration of *p*HPMA copolymers in the mixed solutions is chosen in a range safely above the CMC, namely 0.25–4.0 mg mL^{-1}. In previous studies using fluorescence correlation spectroscopy (FCS) along with doping the polymer solution using Rhodamine 6G (Rh6G), the CMC was found to depend mainly on the cholesterol content of the system:[10, 107] For 2.1 mol% cholesterol side groups, which is the value for all polymer samples in the present study, the CMC is at ca. 0.12 mg mL^{-1}. The lowest chosen concentration, i.e. 0.25 mg mL^{-1}, is thus safely above the CMC. This is also proven in the present work using SAXS, the results of which will be discussed in this chapter.

Attempts were made to investigate the mixed solutions of the copolymer *p*HPMA-Chol-1 and HSA by FCS as well. For *p*HPMA-Chol-1, the concentration was chosen above the CMC at 5.1 mg mL^{-1}. For HSA, the concentration was at 35 mg mL^{-1}, which is within the physiological range. HSA is fluorescent with an emission spectrum having a peak at ca. 330 nm, which is far away from the one of Rh6G (at ca. 560 nm).[166, 167] However, strong fluorescence emission from pure HSA solution was observed in the yellow to red region (see Chapter 6), which overlaps with the emission from Rh6G and was probably originated from other biomacromolecular impurities. The presence of the fluorescence emission from HSA solution hampers the clear distinction of the signal from the Rh6G, which is associated to the NPs. It is thus not possible to characterize the NPs in the presence of HSA using doping of Rh6G. Although major morphological changes induced by protein binding, e.g. formation of large aggregates, may also be detected using dynamic light scattering (DLS),[103] the adsorption of a small amount of proteins to the surface of the NPs can only be observed by combining the more sensitive methods, namely small-angle scattering and ITC (Figure 5.1). The reason is that DLS cannot resolve two different particles have close size due to overlap of signals in the full time range in the autocorrelation function.

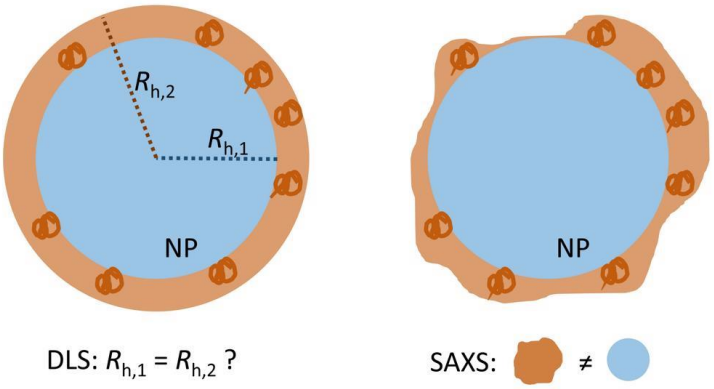

Figure 5.1: A sketch of the adsorption of a small amount of proteins to the surface of a NP. Left: DLS cannot resolve the adsorption due to minor increase in the overall size of the particle. Right: The morphological change resulting from protein adsorption can be resolved by small-angle scattering method such as SAXS.

In the present study, the interaction between *p*HPMA-based NPs and HSA was investigated instead using a combination of synchrotron SAXS and ITC. The reason for this choice of methods is based on the following: In SAXS, morphological changes, such as complexation of the investigated components, are expected to give a scattering curve which is not equal to the sum of the curves of the individual components (equation 4.7). Thus, SAXS allows us to detect the formation of a protein corona. However, in the case, where only a small fraction of HSA molecules is involved in the binding process, the free HSA molecules (unbound ones) still contribute to the scattering signal, and superpose the signal from the bound ones. In contrast, ITC (which is widely used in ligand binding studies) is sensitive to the heat generated through binding events, whereas there is almost no signal generated by the unbound molecules. Therefore, ITC is an ideal complementary method to SAXS, particularly when only a small fraction of HSA binds to the NPs.

5.1. Sample preparation

5.1.1. Sample preparation for SAXS, time-resolved SAXS and ITC measurement

All copolymer solutions for SAXS were prepared in PBS. HSA solutions were prepared by dissolution of HSA[i] (lyophilized powder, ≥ 97%) in PBS at concentrations of 70 mg mL^{-1} or below. Subsequently, the solutions of *p*HPMA-Chol-1 were mixed with the solutions of HSA, such that the resulting concentration of *p*HPMA-Chol-1 was 0.50, 1.0, 2.0 and 4.0 mg mL^{-1}. At each of these concentrations, the concentration of HSA was chosen at 0, 0.35, 3.5 or 35 mg mL^{-1}, the latter being the physiological value. A similar procedure was used for *p*HPMA-Chol-Dox-1, where HSA[ii] (lyophilized powder, 99%, fatty acid free, globulin free) was used. The resulting polymer concentration in the mixed solution was fixed at 4.0 mg mL^{-1} whereas the HSA concentration was chosen at 0, 3.5, 10, 20, 35 or 50 mg mL^{-1}. For time-resolved SAXS measurement, similar procedure was used to prepare the solutions of *p*HPMA-Chol-Dox-3 and HSA in PBS. The polymer concentration was chosen at 2 mg mL^{-1}, and the HSA concentration at 10 mg mL^{-1}. HSA[ii] was used for the time-resolved SAXS experiment.

All polymer solutions for ITC were prepared as well in PBS at 1 mg mL^{-1}. The titrant, i.e. the HSA solution, was prepared in PBS at 50 mg mL^{-1} by dissolution of powder. Prior to measurement, all prepared solutions were shaken for 24 h. HSA[ii] was used for ITC measurements.

5.1.2. Sample preparation for SANS measurement

Two backbone-deuterated copolymer samples were investigated in SANS experiment, namely a Dox-free copolymer *p*HPMA-Chol-d6 and a Dox carrying copolymer *p*HPMA-Chol-Dox-d6. The deuteration positions are shown in Figure 3.5. The buffer used for SANS has a D_2O/H_2O ratio of 59:41, which has a SLD of 3.5×10^{-6} $Å^{-2}$. This value matches the one of the *p*HPMA copolymer assuming a mass density of 1.1 g cm^{-3}. The volume ratio of D_2O/H_2O was calculated based on the weighted average of the SLDs of D_2O and H_2O, which are 6.3×10^{-6} $Å^{-2}$ and -5.6×10^{-7} $Å^{-2}$, respectively. The SLD of the such prepared buffer, matches the weighted averaged SLD of the entire copolymer system, i.e. including the backbone and the cholesterol side groups, so that they do not contribute to the overall scattering. The SLD variation due to the addition of 7.3 wt% Dox in case of *p*HPMA-Chol-Dox-d6 was ignored, since the SLD of pure Dox, which is ca. 2.6×10^{-6} $Å^{-2}$, is close to the one of the mixed solvent. HSA solution at 7.0 mg mL^{-1} was mixed 1:1 with solutions of pure polymers, resulting in mixed solutions having polymer concentrations of 0, 0.13, 0.5, 1 and 2 mg mL^{-1}, respectively. The HSA concentration

was thus the same at 3.5 mg mL^{-1} in all mixed solutions. This way, the scattering curves are expected to be resulting only from HSA. HSA^{ii} was used for SANS measurements.

5.2. Probing the interaction using SAXS

In this section, the results from SAXS method are shown. It is structured as follows: After giving a detailed characterization of the pure HSA and the pure *p*HPMA NPs, we discuss the results from the mixed solutions of these two components.

5.2.1. HSA solutions

To analyze the influence of HSA on the size and shape of the NPs in detail, solutions of pure HSA having concentrations of 0.35–35 mg mL^{-1} were measured as a reference (Figure 5.2a). All scattering curves feature a plateau at $q < 0.02$ Å^{-1}, together with a decay at $q > 0.06$ Å^{-1}. Since they follow a straight line in the Guinier representation (Figure 5.2b), we use the Guinier approximation (equation 4.9) to calculate the radius of gyration, R_g, of HSA. At 35 mg mL^{-1}, $R_g = 27.4 \pm 0.2$ Å, which matches the value of a HSA monomer. However, much higher values are observed at low HSA concentrations, namely $R_g = 36.0 \pm 0.5$ Å and 37.7 ± 0.3 Å for 0.35 and 3.5 mg mL^{-1}, respectively. We attribute these significantly larger sizes to the presence of HSA dimers, which forms preferably at low HSA concentration. Dimer formation of HSA has been reported before.[168]

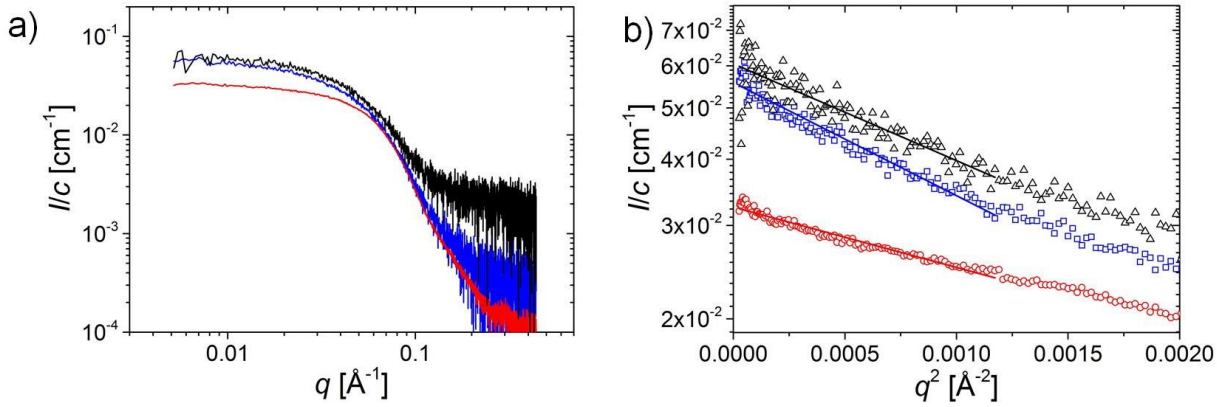

Figure 5.2: (a) SAXS curves of HSA solutions at concentrations of 0.35 mg mL^{-1} (black), 3.5 mg mL^{-1} (blue) and 35 mg mL^{-1} (red) and (b) the corresponding Guinier plots. The symbols are the experimental data and the straight lines the fits of the Guinier model (equation 4.9). Reprinted with permission. Copyright (2018) American Chemical Society.

One plausible explanation for the counterintuitive inverse relation between dimer abundance and HSA concentration is agitation of HSA by water-air interfaces in the solution, which can be caused by shaking of the solution. The protein molecules, which are near these interfaces, are partially denatured to expose their buried hydrophobic domains to the hydrophobic air phase. As a result, dimers may form due to hydrophobic interaction between two monomers. We can

now safely assume a constant area of the total water-air interfaces in the solutions since they all experienced the same shaking procedure. This assumption means, that the constant interface can influence only a limited number of HSA molecules and induce dimer formation. In other words, a much larger number of HSA molecules, i.e. higher concentration, will saturate these interfaces, resulting in HSA molecules which are not influenced by the interfaces and thus do not form dimers. Similar inverse relation of aggregation of globular protein and concentration was reported previously.[169] Moreover, the inverse relation of HSA dimer formation and concentration was clearly observed using analytical ultracentrifugation (AUC). Details of these AUC results are given in the Appendix A.

5.2.2. *p*HPMA-Chol-1 solutions.

To characterize the interaction between the NPs and HSA, we firstly investigate the structure of the cholesterol carrying copolymer *p*HPMA-Chol-1 in PBS without HSA. The SAXS curves of *p*HPMA-Chol-1 at concentrations ranging from 0.50 mg mL^{-1} to 4.0 mg mL^{-1} are shown in Figure 5.3a. For the curves with concentrations of 0.13 mg mL^{-1} and above, a pronounced decay in I/c is observed in the intermediate q range (0.01 Å^{-1} < q < 0.07 Å^{-1}), which we tentatively ascribe to the form factor of the NPs, along with the scattering from concentration fluctuations at higher q values. At low q values, the scattered intensity decays like $I \propto q^{-1}$, pointing to an elongated shape of the NPs. All curves overlap in the region up to 0.07 Å^{-1}, indicating similar values of both the semi-major and the semi-minor axis of the elongated NPs. Due to the increased noise level observed with decreasing polymer concentration, the curves with concentrations below 0.50 mg mL^{-1} are shown separately in Figure 5.3b. The decay is no longer present in the case of 0.06 mg mL^{-1}, presumably, because the concentration is lower than or close to the CMC. Compact particles and random coils can be distinguished using a Kratky plot, where $I\,q^2$ is plotted versus q (Figure 5.3c). For random coils, a smooth plateau is observed, whereas for compact particles, the curves are usually bell-shaped.[170] At 4.0 mg mL^{-1} and 8.0 mg mL^{-1}, the bell-shape is clearly identified at ca. 0.03 Å^{-1}, pointing to the formation of compact structures. In contrast, the presence of the plateau can be clearly observed in the red curve from *p*HPMA-Hyd, which does not have cholesterol side groups and thus cannot self-assemble into NPs, confirming the random coil chain conformation. Detailed analysis of the SAXS curve of *p*HPMA-Hyd is give in Appendix A. No conclusion is drawn due to the noise level of the curve at 0.06 mg mL^{-1} (inset of Figure 5.3c).

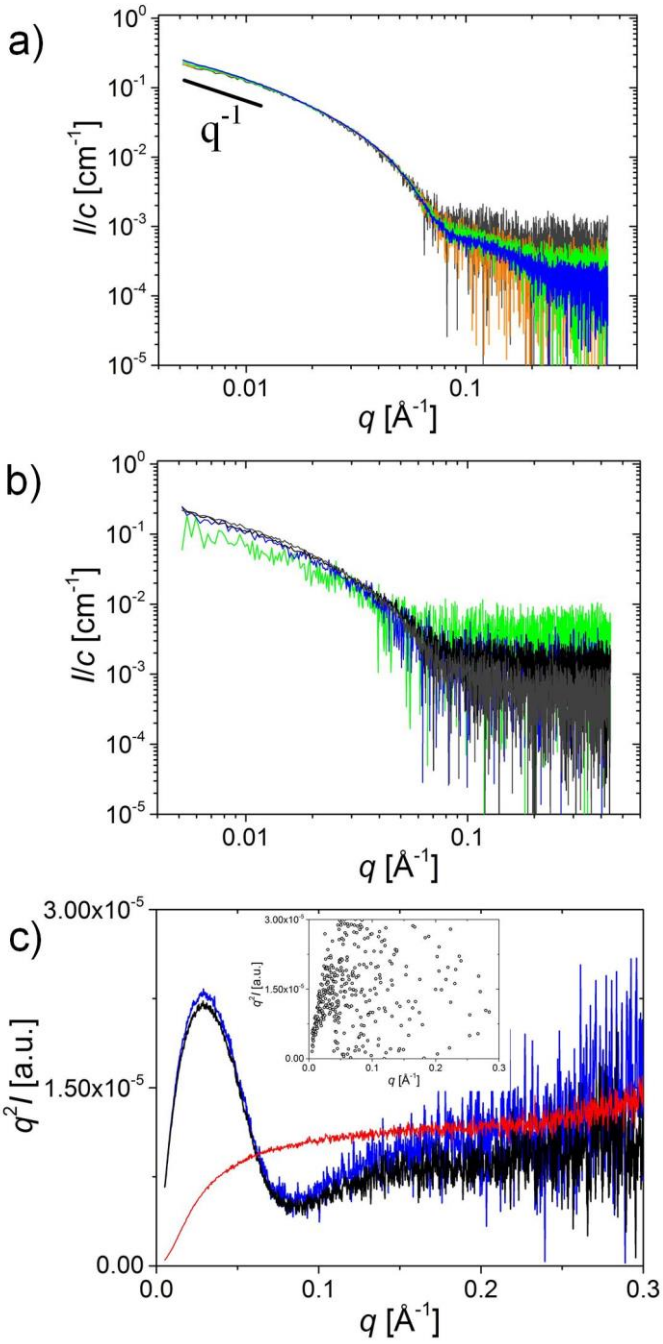

Figure 5.3: (a) SAXS curves of solutions of the *p*HPMA-Chol-1 copolymer in PBS having concentrations of 0.50 mg mL^{-1} (grey), 1.0 mg mL^{-1} (orange), 2.0 mg mL^{-1} (green) and 4.0 mg mL^{-1} (blue). (b) SAXS curves of solutions of the *p*HPMA-Chol-1 copolymers in PBS having concentrations of 0.06 mg mL^{-1} (green), 0.13 mg mL^{-1} (blue), 0.25 mg mL^{-1} (black) and 0.50 mg mL^{-1} (grey). In (a) and (b), the scattered intensity is normalized by the polymer concentration. (c) Kratky plot of SAXS curves from *p*HPMA-Chol-1 at 0.06 mg mL^{-1} (inset), 4.0 mg mL^{-1} (blue) and 8.0 mg mL^{-1} (black), and the one from *p*HPMA-Hyd at 20 mg mL^{-1} (red). Reprinted with permission. Copyright (2018) American Chemical Society.

In order to quantitatively analyze the size and shape of the NPs, the scattering curves were fitted using the following equation:

$$I(q) = I_0 P_{ell}(q) + S_{OZ}(q) + I_{bkg}, \quad (5.1)$$

where I_0 is a scaling factor, $P_{ell}(q)$ the form factor of monodisperse ellipsoidal particles, $S_{OZ}(q)$ the Ornstein-Zernike structure factor (see Chapter 4.1.5.3) and I_{bkg} the background. It comprises the form factor of ellipsoids, $P_{ell}(q)$ (equation 4.14), and the Ornstein-Zernike term, $S_{OZ}(q)$ (equation 4.17). The contributions to the model curve are shown in Figure 5.4. The choice of a form factor of ellipsoid is based on previous SAXS results on similar copolymers.[10] The form factor of ellipsoid was successfully fitted to the scattering curve of a *p*HPMA copolymer carrying 1.4 mol% cholesterol without Dox. An elongated ellipsoid-like structure of the NP was revealed by further 3D ab initio modeling.[10]

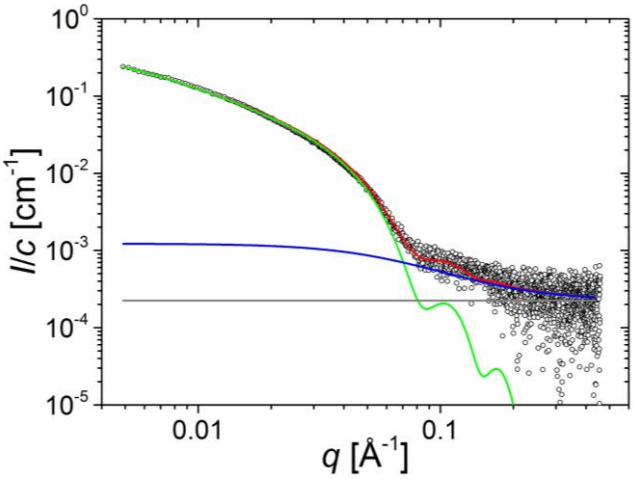

Figure 5.4: Model fit of the SAXS curve of *p*HPMA-Chol-1 having a concentration of 2.0 mg mL^{-1} together with the contributions (equation 5.1). The scattered intensity is normalized by the polymer concentration. Symbols: experimental curve. Red: fitting function; green: form factor of ellipsoid, $P_{ell}(q)$; blue: Ornstein-Zernike structure factor, $S_{OZ}(q)$; grey: background. Reprinted with permission. Copyright (2018) American Chemical Society.

The fit of this model is good over the full q range. The decay up to q = 0.06 Å^{-1} is well captured by the form factor of ellipsoid, and the scattering at high q values (q > 0.06 Å^{-1}) by the Ornstein-Zernike term together with the first fringe of the form factor of ellipsoidal particles. These fringes may be smeared due to size distribution of the ellipsoids. Fits are also good for concentrations in the range of 0.50–4.0 mg mL^{-1}. The curve at the lowest concentration measured, i.e. 0.06 mg mL^{-1}, cannot be reasonably fitted by model due to high noise level.

Above this concentration, the NPs are always observed, meaning that the CMC is lower than 0.13 mg mL^{-1}, which is in good agreement with the CMC values determined by FCS.[107]

Additional models, such as spherical particles, were tested to fit the scattering curves. However, the best and also simplest fit is obtained using the present model as shown above. Mathematically, this is mainly due to the presence of the decay of the scattered intensity following $I \sim q^{-1}$ in the low q range, pointing to elongated structures. This explains why the data cannot be described by form factors for symmetric particles, e.g. spheres (equation 4.10, for fitting see Appendix A).

Figure 5.5 shows the resulting structural parameters. Between 0.13 mg mL^{-1} and 1.0 mg mL^{-1}, the semi-major axis of the ellipsoids is found to be 400 ± 75 Å. Above 1.0 mg mL^{-1}, we observe a slight increase to 460 ± 20 Å. The semi-minor axis is found in the range of 50–60 Å, which is observed to be independent of the concentration in the full range. This means that the aggregation number, i.e. the number of unimers per NP, increases slightly when the concentration is above 1.0 mg mL^{-1}. The NPs mainly grow along the semi-major axis and forms a highly elongated structure having a ratio of semi-major axis to semi-minor axis at ca. 8, confirming previous findings.[10] We attribute this highly elongated structure to the 2-fold symmetry axis of the crystalline structure of cholesterol,[171] which presumably stack along their symmetry axis to form an elongated aggregate, namely the core of the NP. The correlation length ξ from the Ornstein-Zernike structure factor, $S_{OZ}(q)$, was fixed at 15 ± 3 Å for all concentrations, since no significant variation was observed. ξ describes the correlation length of the fluctuations in the shell formed by the *p*HPMA chains which surround the densely packed cholesterol cores.[10] To characterize the concentration dependence of the size of these NPs, the radius of gyration, R_g, is calculated from the values of the semi-major and the semi-minor axis using equation 4.16. The R_g value increases with concentration. This is due to the fact that the semi-minor axis of these NPs hardly changes.

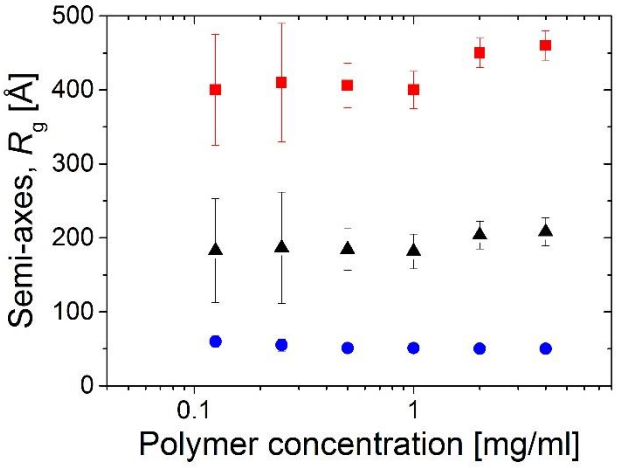

Figure 5.5: Resulting structural parameters for solutions of the *p*HPMA-Chol-1 copolymer in PBS. Semi-major axis (red squares), semi-minor axis (blue circles) and radius of gyration, R_g calculated using equation 4.16 (black triangles). Reprinted with permission. Copyright (2018) American Chemical Society.

5.2.3. Mixed solutions of *p*HPMA-Chol-1 and HSA.

As a reference for the drug-containing system, we first discuss the results of the drug-free *p*HPMA-Chol-1 in the presence of HSA. Figure 5.6 shows the SAXS curves of mixed solutions of *p*HPMA-Chol-1 and HSA in wide concentration ranges of both copolymer (0.50–4.0 mg mL^{-1}) and HSA (0.35–35 mg mL^{-1}). NP formation is justified in all these mixtures since all the chosen polymer concentrations are far above the CMC. The HSA concentrations are chosen in a wide range from a relative low value (0.35 mg mL^{-1}) up to the physiological value (35 mg mL^{-1}). For all copolymer concentrations, a shoulder in the range of 0.05–0.1 Å grows with HSA concentration, which is attributed to the increasing HSA volume fraction. For the highest HSA concentration, 35 mg mL^{-1}, the curves are characterized by a plateau in the low *q* region (0.005–0.05 $Å^{-1}$), and the scattering is thus dominated by HSA.

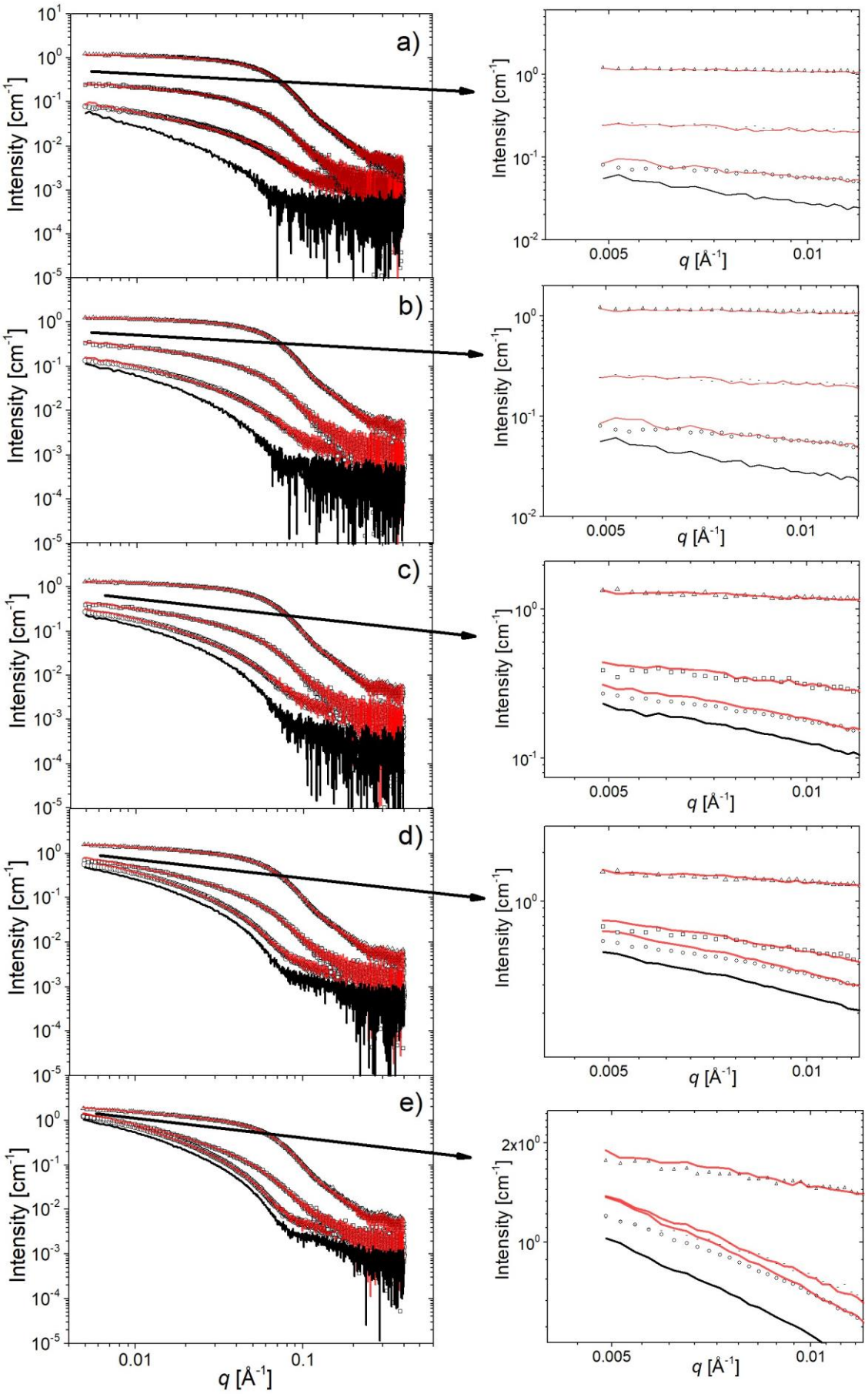
a)
b)
c)
d)
e)
Intensity [cm^{-1}]
q [Å^{-1}]
0.01
0.1
0.005

Figure 5.6: SAXS curves of mixed solutions of *p*HPMA-Chol-1 and HSA at various concentrations (symbols) together with the fits (red curves). The lowermost black curve in each plot is the scattering from pure *p*HPMA-Chol-1. The concentration of *p*HPMA-Chol-1 is 0.25 mg mL^{-1} (a), 0.5 mg mL^{-1} (b), 1.0 mg mL^{-1} (c), 2.0 mg mL^{-1} (d) and 4.0 mg mL^{-1} (e). In each graph, the HSA concentration is (from bottom to top) 0.35 mg mL^{-1}, 3.5 mg mL^{-1} and 35 mg mL^{-1}. The arrows mark the zoom-ins for the very low q regions visualizing the tiny mismatch in very low q region.

To analyze the influence of HSA on the NPs, we fit all the scattering curves shown in Figure 5.6 using the model in equation 4.7 with the volume fraction v_{HSA} as a fitting parameter. We note that equation 4.7 only holds true provided that the *p*HPMA NPs and HSA do not form complexes and that their form factors do not undergo major changes. To the best of our knowledge, binding of HSA to ligands in the NPs, namely cholesterol and Dox, only alters the secondary structure of HSA.[172, 173] These local changes are expected to affect the scattering curves mainly at very high q values, and not in the q-range investigated here using SAXS. Moreover, there is no evidence that the interaction between HSA is altered upon such binding.

Since the model fits are good over the full q range for all polymer and HSA concentrations, the scattering of the mixed solution is a linear combination of the scattering of *p*HPMA-Chol-1 and HSA, indicating the absence of strong interactions between the NP and HSA. A scenario where a hard HSA corona forms around the NPs can thus be excluded. However, it is noteworthy that a tiny mismatch is observed only at very low q values for polymer concentrations above 1.0 mg mL^{-1} (Figure 5.6c,d and e). A plausible explanation is that a small amount of HSA adsorbs onto the NPs and forms a complex. Nevertheless, these *p*HPMA/HSA complexes do not alter the overall scattering profile dramatically due to their small population compared with the ones of the free NPs and HSA.

The resulting volume fractions of HSA, v_{HSA}, are plotted in Figure 5.7a in dependence on HSA concentration and for the polymer concentrations studied. Considering a constant exposed volume of the mixed solutions in X-ray beam, which is determined by the diameter of the capillary, it is reasonable that v_{HSA} increases with the concentration of HSA. The model given in equation 4.8, which describes the relation between v_{HSA} and HSA concentration, is fitted to the data obtained at different polymer concentrations. The resulting density ratios between *p*HPMA-Chol-1 and HSA are shown in Figure 5.7b. The ratios assume the same value 0.79 ± 0.04 for all polymer concentrations, i.e. the volume fractions given by the fit by equation 4.8 are reasonable. Only at the highest polymer concentration, namely 4.0 mg mL^{-1}, the fit is less

good, probably because the binding of HSA is promoted when more NPs are present in the system.

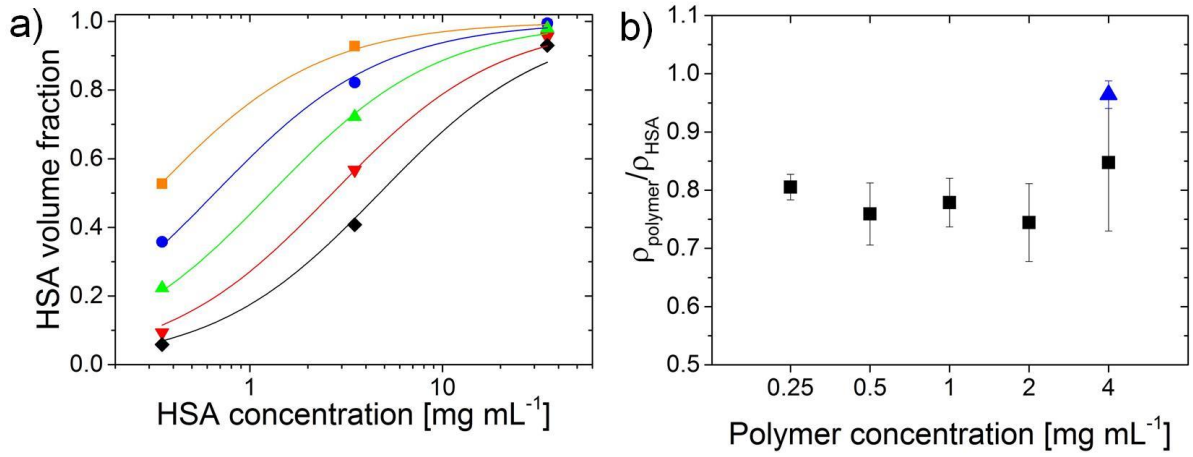

Figure 5.7: (a) HSA volume fraction obtained by fitting equation 4.7 for a mixed solution of *p*HPMA-Chol-1 and HSA in PBS. Symbols indicate different polymer concentrations: (■) 0.25 mg mL^{-1}, (●) 0.5 mg mL^{-1}, (▲) 1.0 mg mL^{-1}, (▼) 2.0 mg mL^{-1} and (◆) 4.0 mg mL^{-1}. The corresponding curves are the fits of equation 4.8. The error bars are not shown since all uncertainties are below 0.002. (b) Resulting density ratios of *p*HPMA-Chol-1 and HSA in dependence on polymer concentration (black squares). The blue triangle gives the density ratio of *p*HPMA-Chol-Dox-1 and HSA. Adapted with permission. Copyright (2018) American Chemical Society.

5.2.4. Mixed solutions of *p*HPMA-Chol-Dox-1 and HSA

To analyze the influence of Dox on the interaction between HSA and the NPs, a copolymer has cholesterol side groups as in *p*HPMA-Chol-1, but in addition 6.0 wt% Dox bound to the backbone via hydrazone bond, is mixed with HSA in PBS. The polymer concentration of *p*HPMA-Chol-Dox-1 is kept at 4.0 mg mL^{-1} which is safely above the CMC. The resulting SAXS curves are shown in Figure 5.8.

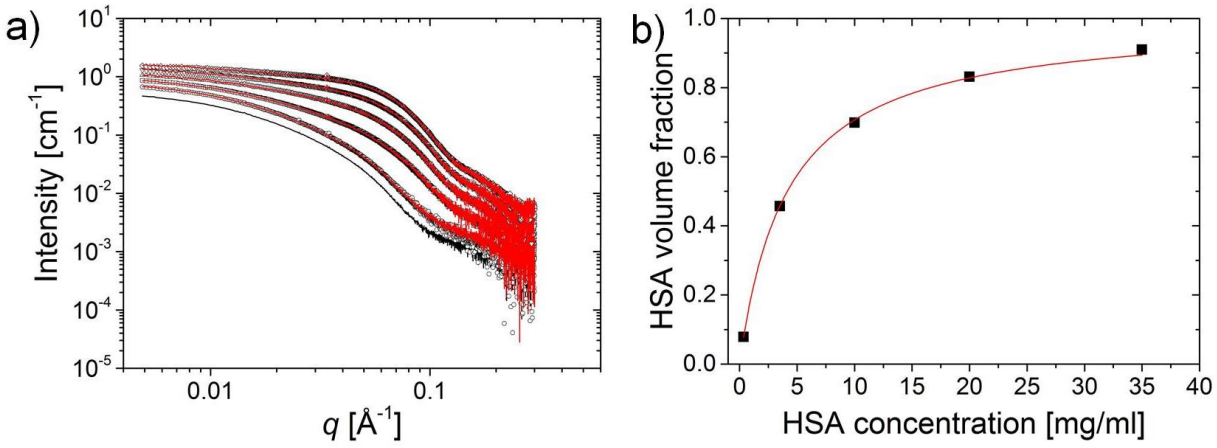

Figure 5.8: SAXS curves of mixed solutions of *p*HPMA-Chol-Dox-1 and HSA at various concentrations (symbols) together with the fits (red curves). The lowermost black curve is the scattering from pure *p*HPMA-Chol-Dox-1 having a concentration of 4.0 mg mL^{-1}. The HSA concentration is (from bottom to top) 0.35 mg mL^{-1}, 3.5 mg mL^{-1}, 10 mg mL^{-1}, 20 mg mL^{-1} and 35 mg mL^{-1}. (b) HSA volume fraction obtained by fitting equation 4.7 for a mixed solution of *p*HPMA-Chol-Dox-1 and HSA in PBS. The corresponding curve is the fit of Equation 4.8. The error bars are not shown since all the errors are below 0.001. Adapted with permission. Copyright (2018) American Chemical Society.

Similar to the mixed solutions of *p*HPMA-Chol-1 and HSA, a shoulder increases with HSA concentration in the q range 0.05–0.1 Å^{-1} due to an increase in HSA volume fraction. The SAXS curves are again fitted using the model given by equation 4.7. Unlike the *p*HPMA-Chol-1/HSA mixtures, where a slight mismatch appears at very low q values, the fits are perfect over the full q range for all the mixed solutions. Fitting the model given by equation 4.8 to the resulting HSA volume fractions gives the density ratio given in Figure 5.7. It is seen that *p*HPMA-Chol-Dox-1 has a higher relative density with respect to HSA than *p*HPMA-Chol-1.

To summarize, the scattering of both *p*HPMA-Chol-1/HSA mixtures and *p*HPMA-Chol-Dox-1/HSA mixtures are successfully modeled by a linear combination of the scattering from the pure polymer and HSA. Nevertheless, slight mismatches are seen in the *p*HPMA-Chol-1/HSA system, whereas the fit is perfect in case of *p*HPMA-Chol-Dox-1/HSA. We attribute this difference to the presence of additional Dox moieties, which are distributed uniformly over the whole NP, including the shell formed by *p*HPMA, and thus hinders HSA from getting in contact with the cholesterol core or entering meshes formed by the *p*HPMA chains. The influence of Dox is elaborated in the following chapter, where ITC was used as a complementary to SAXS.

The reason for this choice is, that ITC is sensitive only to the bound HSA molecules unlike SAXS, which monitors all HSA molecules, namely the bound and unbound ones.

5.3. Investigation of the interaction between the NPs and HSA using ITC

To test our hypothesis, we performed measurements on similar mixed solutions of polymer and HSA using ITC which is sensitive to binding events, even if their probability is low. This way, a possible binding of HSA to the NPs can be detected despite a low affinity. At this, a concentrated HSA solution (50 mg mL^{-1}) in PBS buffer was titrated into solutions of *p*HPMA-Chol-2 or *p*HPMA-Chol-Dox-1 in PBS buffer, respectively.

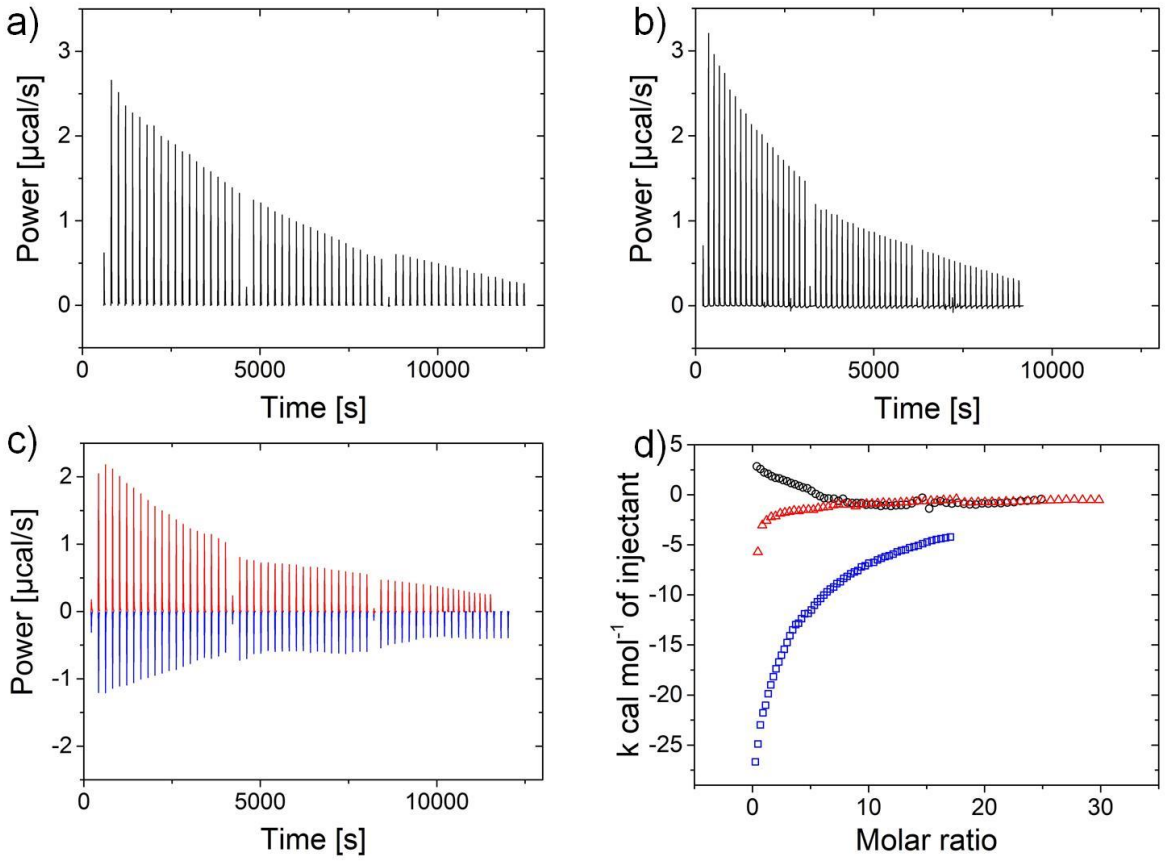

Figure 5.9: ITC thermogram where the heating power is plotted against time for the titration of HSA into PBS (a), *p*HPMA-Hyd (b), *p*HPMA-Chol-2 (c, blue line) and *p*HPMA-Chol-Dox-1 (c, red line), respectively. (d) Integrated ITC curves of the titration of HSA into pHPMA-Hyd (black circles), *p*HPMA-Chol-2 (blue squares) and *p*HPMA-Chol-Dox-1 (red triangles), respectively. In (d), the blank titration (HSA into PBS) is already subtracted.

Figure 5.9 illustrates the incremental heat per mole of added HSA as a function of the molar ratio i.e. [HSA]/[*p*HPMA-Chol-Hyd], [HSA]/[*p*HPMA-Chol-2] and [HSA]/[*p*HPMA-Chol-Dox-1]. Strong exothermic interaction (< -26 kcal/mol) is observed for the titration of HSA into *p*HPMA-Chol-2 (Figure 5.9d), pointing to a clear fact that HSA binds to the NPs formed by *p*HPMA-Chol-2. It is also seen from the same ITC curve that a higher HSA concentration,

namely above 16 mg mL^{-1} (which is the final concentration in the cell), is required, to saturate the binding to these NPs, since the enthalpy given by the last titration has a value of -4.23 kcal mol^{-1}, which is still in the kcal/mol region that is typical for protein/NP binding.[174] From previous SLS results on similar systems,[10] the aggregation number N_{agg} is found to be dependent mainly on the cholesterol content, which is 2.1 mol% in the present system. This cholesterol content corresponds to $N_{agg} \approx 10$. Based on this assumption, the last titration in the ITC curve points to a scenario, where there are maximum 1.7 HSA molecules bind to each NP on average,, which is far from being sufficient to form a protein corona.

For the titration of HSA into *p*HPMA-Chol-Dox-1, the ITC curve differs significantly from the one for *p*HPMA-Chol-2: A much weaker exothermic enthalpy (> -6 kcal mol^{-1}) is observed at the beginning of the titration series. The saturation is reached at the 20th titration, which corresponds to a molar ratio of ca. 0.8 HSA molecules pro NP (using again the assumption: $N_{agg} \approx 10$), meaning that some of the NPs are not bound by any HSA at all. We thus conclude that the interaction of HSA with the NPs formed by *p*HPMA-Chol-2 is much stronger than with those formed by *p*HPMA-Chol-Dox-1, which is in good agreement with our SAXS results: A tiny mismatch indicating weak interaction in case of *p*HPMA-Chol-1 (Figure 5.6); a perfect fit pointing to absence of any interaction in case of *p*HPMA-Chol-Dox-1 and HSA (Figure 5.8).

On the contrary, it must be noted that for the titration of HSA into *p*HPMA-Hyd, which lacks hydrophobic groups, weak endothermic enthalpy is seen instead of exothermic ones as seen in cases of *p*HPMA-Chol-2 and *p*HPMA-Chol-Dox-1. Recalling equation 4.19, the observed unfavorable endothermic enthalpy ($\Delta H > 0$) implies a large favorable entropy change ($\Delta S > 0$), to have a negative free energy of association ($\Delta G < 0$). Similar endothermic enthalpy change was reported on binding of various proteins to amphiphilic NPs.[175, 176]

Attempts were also made to analyze the ITC curve of *p*HPMA-Chol to obtain quantitative information such as stoichiometry and binding constant. However, the measured titration heat still did not reach the base line after 3 titrations in series, which makes fits of the ITC curve using mathematic models not applicable. Normally, two approaches are suggested to solve such a case, that the binding is not saturated after multiple titration series: (i) To reduce the polymer concentration in the cell, so that less titrant is needed to saturate the binding. (ii) To increase the concentration of the titrant in the syringe, so that a much higher final titrant concentration can be realized. However, in our system, neither (i) nor (ii) works. On one hand, the polymer concentration was 1 mg mL^{-1}, which must be safely above the CMC (ca. 0.12 mg mL^{-1}) and thus should not be further decreased. On the other hand, the concentration of HSA was 50 mg

mL^{-1} in the cell, which is only slightly below its physiological upper limit at ca. 53 mg mL^{-1} and should not be further increased to prevent protein aggregation caused by molecular crowding at high protein concentrations.[177]

In a few words, the ITC result shows a strong binding enthalpy between HSA and the Dox-free NPs. When Dox is present, the binding is significantly suppressed, which is in good agreement with the SAXS result discussed previously.

5.4. Complementary information obtained using SANS

As mentioned previously, despite the confirmed binding of HSA to the *p*HPMA NPs using SAXS and ITC, it was not possible to obtain structural information on the individual components, i.e. the NPs or HSA, due to overlap of the scattered intensity in the full *q* range. Therefore, SANS was used to characterize the behavior of HSA in the presence of the *p*HPMA NPs, by employing the method of solvent matching. At this, the scattering length density (SLD, see Chapter 4.1.3) of the polymer is matched by the buffer using a mixture of H_2O and D_2O. As a result, it is expected that only HSA contributes to the overall scattered intensity, and its behavior can thus be investigated independently of the NPs. Two pure copolymer solutions of *p*HPMA-Chol-d6 and *p*HPMA-Chol-Dox-d6 having a concentration of 4 mg mL^{-1} were measured to verify the solvent matching point.

It is seen in Figure 5.10a that both copolymer samples, *p*HPMA-Chol-d6 and *p*HPMA-Chol-Dox-d6, are successfully masked in the *q* range 0.04–0.4 $Å^{-1}$ since the scattered intensity is very close to the one of the PBS. On the contrary, the scattering from HSA is still clear visible in this region. However, in the *q* range 0.01–0.04 $Å^{-1}$, a strong forward scattering is observed for both *p*HPMA-Chol-d6 and *p*HPMA-Chol-Dox-d6, which is attributed to the cholesterol core of the NPs, the SLD of which was not matched using the prepared solvent.

It is observed in the solvent-matched SANS curves, that with increasing concentration of *p*HPMA-Chol-d6, the scattering from HSA also increases slightly (Figure 5.10b). On the opposite, it remains unaltered with increasing concentration of *p*HPMA-Chol-Dox-d6 (Figure 5.10c). This indicates that the secondary structure of HSA is slightly altered in the presence of *p*HPMA NPs without Dox due to a binding process, and thus supports the previous speculation made based on SAXS and ITC results: Dox hinders the binding of HSA to the NPs.

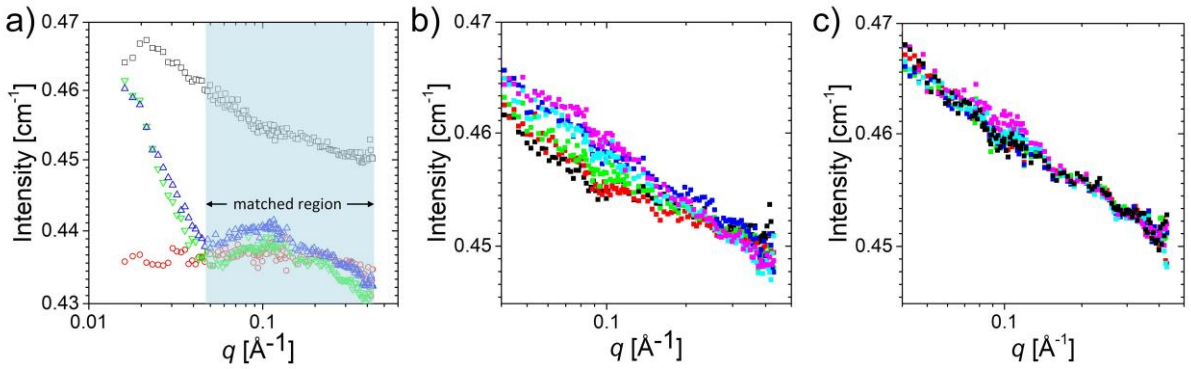

Figure 5.10: SANS curves from *p*HPMA copolymer solutions mixed with HSA. (a) Scattering curves of the reference solutions, to check the valid solvent match region: HSA, black squares;

*p*HPMA-Chol-d6, green down-pointing triangles; *p*HPMA-Chol-Dox-d6, blue up-pointing triangles; PBS, red circles. (b,c) Scattered intensity of *p*HPMA-Chol-d6 (b) and *p*HPMA-Chol-Dox-d6 mixed with HSA. The concentration of HSA is constant at 3.5 mg mL^{-1}. The polymer concentration is indicated by colors: 0 mg mL^{-1}, black; 0.13 mg mL^{-1}, red; 0.5 mg mL^{-1}, green; 1 mg mL^{-1}, blue; 2 mg mL^{-1}, light blue; 4 mg mL^{-1}, magenta. In (b) and (c), the scattering curves are shown for $q > 0.04$ $Å^{-1}$, in which the copolymers are completely masked.

5.5. Drug release from the NPs in the presence of HSA

There are of course additional aspects which should be considered. For instance, it is still not known whether the drug release from the NPs is affected by HSA, especially when binding of HSA to the NPs was observed. As a first step, the release of Dox from the *p*HPMA NPs from *p*HPMA-Chol-Dox-3 was monitored using time-resolved DLS over a period of 8 hours (inset of Figure 5.11a and b). Prior to the beginning of the DLS measurements, a droplet of 1 M HCl was added into the solutions to induce a pH jump from 7.4 to ca. 5, mimicking a scenario that the drug delivery NPs reach the tumor. DLS result shows a decrease in R_h after the pH jump, pointing to the release of Dox from the NPs (inset of Figure 5.11a inset). When HSA is present at a concentration of 28 mg mL^{-1}, similar decreasing trend of R_h was observed within the first 200 min after the pH jump, followed by fluctuations of R_h with time. Due to resolution limit of DLS (Figure 5.1), this fluctuation cannot be resolved. Therefore, time-resolved SAXS experiments were carried out on the same polymer sample mixed with HSA in PBS, as measured by DLS. To avoid a situation where the overall scattering signal is superposed by the one of HSA, a relative low HSA concentration was chosen, namely at 10 mg mL^{-1}, which is below its physiological value. The polymer concentration was 2 mg mL^{-1}, which is safely above the CMC.[107] A pH jump was induced at the time zero by addition of HCl as described above.

The time-dependent SAXS curves of the solution without and with HSA measured in 14 h time period are shown in Figure 5.11a and b, respectively. When HSA is absent (Figure 5.11a), a minor decrease in the forward scattering is seen, indicating a decrease of the NP size caused presumably by Dox release. However, when HSA is present (Figure 5.11b), little change is observed over the whole time range up to 14 h. There are two probable reasons, for which the scattering curve do not alter with time: (i) Dox release is hindered by HSA. The size of the NP thus remains, resulting in identical scattering curves with time. (ii) Dox is released from the NPs, and contributes to the overall scattering in a way that it compensates the change of the curve due to the decrease in NP size. Nevertheless, based on only the data obtained from time-resolved SAXS, no concrete conclusion can be made. Proper labels, e.g. fluorescence, must be used, to be able to resolve this complex system.

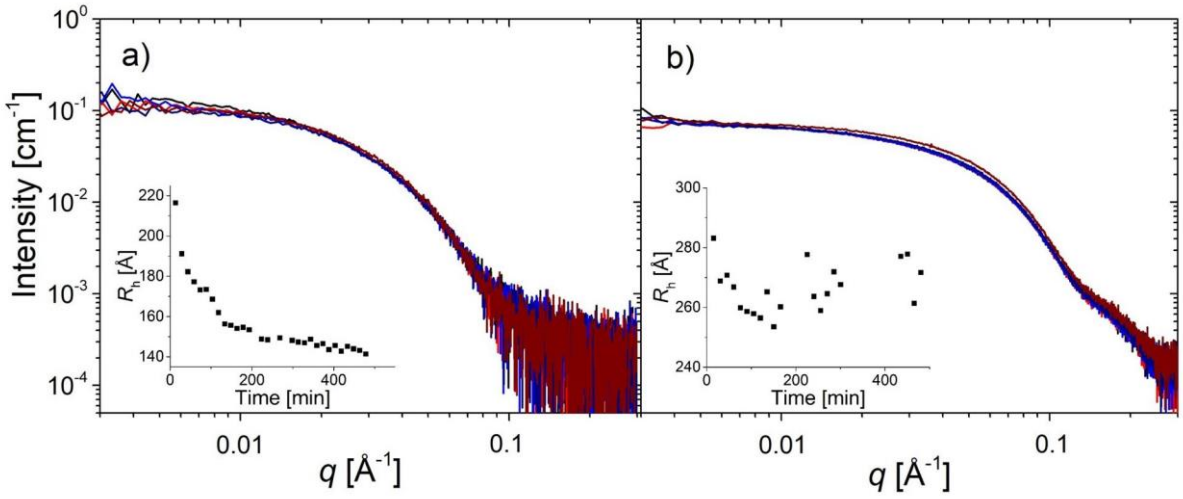

Figure 5.11.: SAXS curves *p*HPMA NPs carrying Dox without (a) and with (b) HSA. The polymer concentration was 2 mg mL^{-1}, and the HSA concentration was 10 mg mL^{-1}. Upon start of the SAXS measurement, a droplet of HCL was titrated into the solutions to make a pH jump from 7.4 to 5. SAXS images were recorded during a total period of 840 min with predefined intervals. The color of the curves indicates the time after the start of the experiment: Black, 15 min; Red, 75 min; Blue, 135 min; Dark blue, 450 min; Braun, 840 min. Inset of (a) and (b): Time-resolved R_h values of the NPs in the absence and in the presence of HSA obtained using DLS. A droplet of HCl was added into the solutions to change the pH from 7.4 to ca. 5 at the time zero.

5.6. Discussion and conclusion

In this chapter, we have discussed results of the mixed solutions of *p*HPMA NPs and HSA in PBS obtained using a combination of three methods, namely SAXS, SANS and ITC, which can be potentially applied to other studies involving possible complex formation through ligand binding. To check the presence of complex, we model the SAXS curves of the mixed solutions using a sum up of the curves of the individual components. This fit is model-free and independent of other physical parameters, e.g. concentration of the HSA and polymer. Nevertheless, SAXS may reach its limits in the case that only few HSA molecules bind to the NPs due to overlap of signals of the bound and unbound HSA molecules in the full q range. ITC served as a complementary method, because it is sensitive to the absolute number of bound HSA molecules.

The SAXS curves from the mixtures of HSA and *p*HPMA NPs with and without Dox are fitted successfully by a linear combination of the curves of the pure solutions, i.e. there are no significant structural changes such as formation of a protein corona or disassembly of the NPs. Such good fits also indicate that any structural change of HSA as well as of the NPs, if there is any, is also minor. Nevertheless, a tiny mismatch is observed at very low q values when Dox is absent, which is tentatively attributed to the binding of a small amount of HSA to the NPs. This not the case when the NPs contain Dox.

To prove that a small fraction of HSA binds to the NPs and to characterize the influence of Dox, similar mixtures of HSA and NPs are investigated using ITC. This way, the binding between HSA and the NPs can be observed regardless of the fraction of HSA which binds to the NPs. The ITC result shows a clear evidence of binding to the NPs from both *p*HPMA-Chol-2 and *p*HPMA-Chol-Dox-1. Furthermore, a much weaker binding enthalpy is observed in case of the latter one, meaning that the presence of Dox to some extent hinders the binding between HSA and the NPs.

We attribute these findings to the characteristic property of HSA, to transport hydrophobic ligands in the human body, e.g. fatty acids,[18] monoacylglycerol lipase,[19] bile acid and hydrophobic drugs such as digitoxin.[17] It was reported that HSA significantly promotes the efflux of ^{3}H-labeled cholesterol from human cells.[118] In another study, the binding between HSA and cholesterol was investigated quantitatively and it was reported that, on average, 0.98 cholesterol molecules bind to each HSA molecule.[178] Therefore, it is plausible that the HSA molecules interact with the NPs through the following two mechanisms (Figure 5.12): (i) HSA

binds to the cholesterol groups in an area which is covered by loose *p*HPMA chains, or to the cholesterol groups which are located in the shell of the NP. Recalling that the cholesterol groups are randomly distributed over the copolymer chains, a few cholesterol groups may not be included in the core. (ii) HSA interacts with the hydrophilic *p*HPMA shell of the NP and is confined in the meshes of *p*HPMA chains. It is important to note that both (i) and (ii) are likely to be dynamic processes, which do not necessarily refer to permanent binding between HSA and the NPs. Dox is far less hydrophobic than cholesterol because of its 5 hydroxyl groups and 1 amino group, thus not expected to be fully included in the core, as proven experimentally.[10] Therefore, it hinders both processes (i) and (ii) (Figure 5.12b). In a few words, the presence of Dox hinders the binding between the NPs based on *p*HPMA and HSA, which is the most abundant protein in blood plasma. This means that the delivery of Dox by the NPs in the human body should not be affected by the presence of HSA, because the structure of the NP remains intact in an environment where HSA is at its physiological concentration.

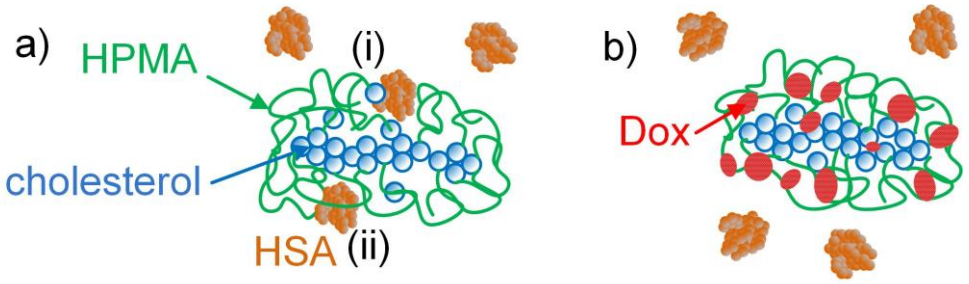

Figure 5.12: (a) Schematic illustration of binding of HSA to the cholesterol groups, a few of which may be in the near-surface area of the NP (i). HSA becomes confined in a mesh formed by the *p*HPMA chains (ii). (b) Dox is distributed uniformly in the *p*HPMA shell and hinders the binding. Adapted with permission. Copyright (2018) American Chemical Society.

These findings also confirm the previous result that the hydrophobicity of the NP plays an important role in determining the amount of protein binding to the NP.[25, 72, 79, 103, 114-116] Here we report that by introducing a hydrophilic shell from *p*HPMA of a very high molar fraction i.e. 97.9 mol%, only very weak binding of HSA is observed. The observed very weak binding is almost completely suppressed when the NP is loaded with 6.0 wt% of the anti-cancer drug Dox, which is much less hydrophobic than cholesterol. The importance of the hydrophobicity of the drug delivery NPs is previously known that it induces the NP formation and usually determines the drug load efficacy. In this study, however, we put emphasize on the hydrophilic components of the system, the importance of which can only be revealed when the system is tested in a more realistic environment containing blood proteins. Based on our experimental

data, we propose a general rule for future designs of copolymeric drug delivering systems: By using a small amount of highly hydrophobic segment along with a high fraction of the hydrophilic block, the latter prevents the undesirable interactions between the drug delivering NP and blood proteins.

Since binding of HSA to the NPs was observed, attempts were subsequently made, to study the release of Dox from the NPs induced by a pH jump in the presence of HSA using time-resolved SAXS. The preliminary result shows, that there is little change in the scattering curve in 14 h after the pH jump. However, due to the complexity of the system, no conclusion could be made based on the SAXS result solely.

Last but not lease, the mechanism of the observed binding is not yet thoroughly understood based on the presented data. Therefore, we use fluorescence labeling, which facilitates observation of the individual components in the system, to further investigate the origin of the binding. We will discuss these results in the next chapter.

6. Revealing the binding mechanism

In the previous chapter, using SAXS, a weak interaction between HSA and the NPs was detected in the *p*HPMA-Chol system without Dox, since the scattering from the mixed solution showed deviations from the sum of the scattering from HSA and the NPs. We attributed the observed interaction to the binding of a small fraction of the HSA molecules to the NPs. When 6 wt% of Dox was conjugated, i.e. *p*HPMA-Chol-Dox, the binding of HSA was suppressed. This difference in behavior in absence and presence of Dox was confirmed using isothermal titration calorimetry (ITC). However, the mechanism of such binding could not be fully resolved based on our SAXS results alone due to the following factors: (i) The small fraction of the HSA molecules which bind to the NPs is superposed by the dominating unbound ones. (ii) The scattering signals from HSA, the NP and the HSA/NP complex overlap in the full q range and cannot be discriminated properly. Therefore, to be able to further resolve the mechanism of the observed binding, proper labeling of the complex system is required.

Hence, we use FLCS to investigate the NPs formed by the amphiphilic *p*HPMA-Chol in HSA PBS solutions. To analyze the influence of HSA on the NP's structure, the copolymers were fluorescence labelled. To eliminate the fluorescence signal of HSA–which hampers the characterization of the labeled NPs–two different signal filtering methods were attempted: (i) an optical bandpass filter having a pass wavelength much higher than the emission wavelength of HSA; (ii) a digital filter which is generated based on the lifetime properties of all fluorescence components that are present. This way, the diffusion behavior of the NPs is distinguished and characterized successfully in the presence of HSA. In this chapter, we are going to treat the obtained FLCS data using both filters and discuss their applicability and limitation with respect to the complexity of the system.

Moreover, another commonly used fluorescence spectroscopic method was employed, namely fluorescence quenching. In a typical fluorescence quenching experiment, the intensity of the intrinsic fluorescence emission of a fluorophore is probed and used as a mean to characterize interactions between the fluorophore other ligands which may quench the fluorophore. In the past decade, it was used for investigations of the interactions between proteins and other chemical compounds, using the intrinsic fluorescence of the investigated proteins.[154-159] Therefore, in contrast to the FLCS measurements, where the intrinsic fluorescence of HSA is carefully removed by filtering, it is used in the quenching experiments to characterize the interaction between the HSA and NPs, by varying the concentration of the NPs. Moreover, a

quenching experiment where a polymeric quencher has been employed, which simultaneously quenches the fluorescence of HSA and self-assembles into NPs, is presented here. Combining the results from FLCS and from the quenching experiment helps to elucidate the origin of the HSA/NP interaction.

6.1. Sample preparation

6.1.1. Sample preparation for lifetime and FLCS measurements

The pure dye AF633 and the dye-labelled copolymer *p*HPMA-Chol* was dissolved in PBS at 0.05 μM, which corresponds to a dye concentration of AF633 of 0.01 μM. This dye-containing PBS (PBS*) was shaken for 24 h and used subsequently to prepare solutions of polymer and HSA.

For lifetime measurements of AF633 (free or attached to *p*HPMA-Chol) and HSA, the solutions were prepared by direct dissolution of powder of AF633 and *p*HPMA-Chol* in a pre-defined volume of PBS*. HSA[i] was used for all lifetime measurements.

For FLCS measurements, the copolymer *p*HPMA-Chol-2 was dissolved in PBS*, such that its resulting concentration was 70, 140, or 280 μM (the latter corresponds to 8 mg mL^{-1}). HSA[ii] was dissolved in PBS* at concentrations of 0, 10 and 104 μM. Then, the three HSA solutions were mixed 1:1 with the three polymer solutions, respectively, resulting in mixed solutions of *p*HPMA-Chol-2 and HSA, with the polymer concentration ranging from 35 to 140 μM (the latter corresponds to 4 mg mL^{-1}), and the HSA concentration ranging from 0 to 52 μM (the latter corresponds to 3.5 mg mL^{-1}). All prepared solutions were protected against bleaching using aluminum films and were shaken for 24 h to ensure a homogeneous distribution of *p*HPMA-Chol*. A similar procedure was used for preparation of the mixed solutions of *p*HPMA-Chol-Dox-2 and HSA, where HSA[i] (lyophilized powder, 97%) was used.

6.1.2. Sample preparation for fluorescence quenching experiments

In the fluorescence quenching experiment, *p*HPMA-Chol-2 was used to quench the intrinsic fluorescence of HSA. Mixed solutions of *p*HPMA-Chol-2 and HSA were prepared in PBS. The HSA concentration was kept constant at 15 μM in all mixed solutions. The concentration of *p*HPMA-Chol-2 was varied from 0 to 70 μM, which covers a wide range around the critical micelle concentration (CMC) which is ca. 5 μM as shown previously.[107] HSA[ii] was used for the fluorescence quenching experiment.

6.2. Lifetime property of AF633

In FLCS, the lifetime characteristic of the dye AF633 is used to separate different FCS autocorrelation function and to discriminate the fluorescence background. Therefore, right before discussions of FLCS and fluorescence quenching results, we first start with an investigation of the lifetime properties of the dye AF633 as well as of HSA.

For most of the fluorophores, the lifetime decays exponentially and can be described using equation 4.40 as discussed previously. However, in some cases, it may not be sufficient to use a single exponential decay to describe the lifetime of some fluorophores. This is often the case for the fluorescence lifetime of proteins, which have a much more complicated chemical environment surrounding the fluorescent ligands. In such cases, where the lifetime is complex, two methods may be used to describe the lifetime: Using a sum of multiple exponential decays or using a distribution function.

In reality, the choice between these two methods depends on the complexity of the lifetime: Most of the lifetimes can be fitted using a sum of maximal 3 exponential decays (n = 3 in equation 4.40). When a fourth exponential decay is needed, this method becomes unstable and less convincing due to overshooting of fitting parameters, and thus the second method, i.e. to fit the intensity decay using a distribution of lifetime, is thus preferred.

6.2.1. Fitting of fluorescence lifetime using single exponential

The fluorescence intensity decay of the pure AF633 dye solution (10^{-8} M) is given in Figure 6.1a together with the fit by a single exponential decay, giving a lifetime of 3.17 ± 0.002 ns. The fit is perfect over the full time range, meaning that there is only a single lifetime decay mode of the pure dye solution. Due to the very low dye concentration, the dye molecules are separated from each other and surrounded by a homogeneous aqueous media, resulting in a very low chance of secondary fluorescence emission, thus a well-defined lifetime. When the dye is covalently bound to *p*HPMA-Chol (*p*HPMA-Chol*, 10^{-8} M, Figure 6.1b), the fit by a single exponential decay is good over the whole time range, with only tiny mismatch at very low time values, giving a lifetime of 2.89 ± 0.008 ns, which is slightly smaller than the lifetime of the pure dye. A decrease in fluorescence lifetime is normally due to dynamic quenching processes of the dye caused by collisions with other molecules (see Chapter 4.4.1), which could be the *p*HPMA-Chol system in this case. Attempt was made to fit the intensity decay of *p*HPMA-Chol* at 10^{-8} M mixed with HSA at 45 mg mL^{-1} (Figure 6.1c), giving a lifetime at 1.7 ± 0.008 ns. However, it can be clearly seen that a single exponential decay is not enough to

resolve the lifetime in case of a complex system. In the following section, we will discuss the fitting results of the same system given by the lifetime distribution method.

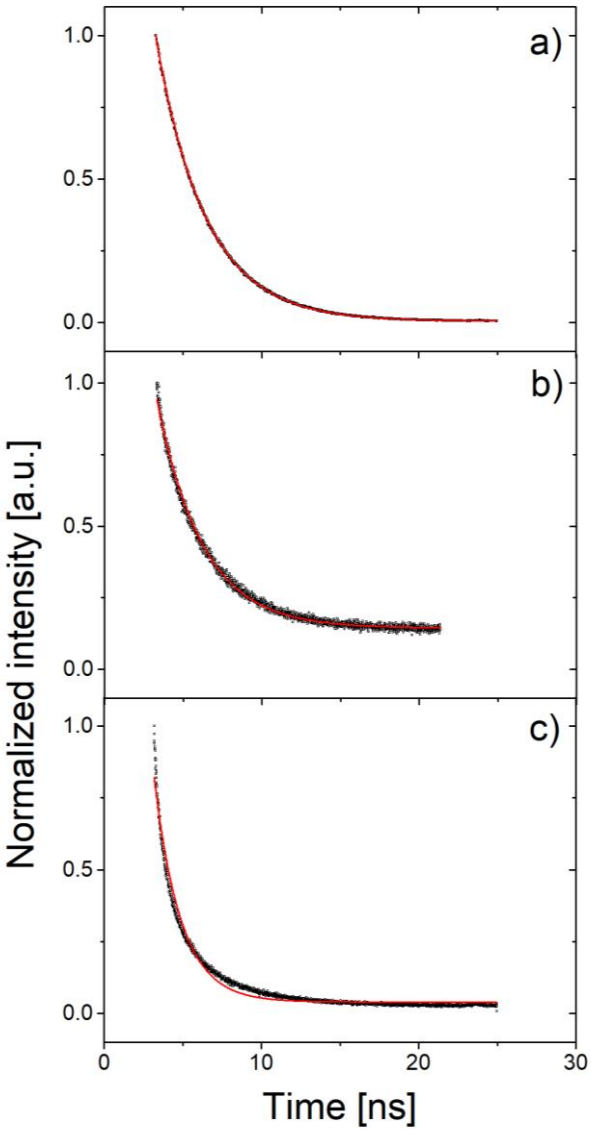

Figure 6.1: Fluorescence intensity decay of the dye AF633 (a) and of the dye AF633 covalently bound to *p*HPMA-Chol (*p*HPMA-Chol*) (b) both dissolved in PBS at a dye concentration of 10^{-8} M. The red curves are the fits using equation 4.40 with $n = 1$.

6.2.2. Fitting of fluorescence lifetime using lifetime distribution

It is a well-established method to fit fluorescence lifetimes using single or even as a sum of multiple exponential decays, this method, however, cannot resolve the phenomenon such as secondary emissions properly. Therefore, for the reference samples, i.e. the AF633, *p*HPMA-Chol* and HSA, we fit their lifetime decays by distributions, which helps elucidate both FLCS and fluorescence quenching results.

The lifetime decay pattern of AF633 is fitted with a lifetime distribution function which is given by:

$$\mathrm{I(t)} = \mathrm{A_1} \int_0^\infty f_{norm}(\tau) \cdot \exp(-\frac{t}{\tau}) d\,\tau + B_1 \tag{6.1}$$

A_1 is a scaling factor, and B_1 the background. t is the arrival time of photons, and τ the lifetime. $f_{norm}(\tau)$ is the normal distribution function:

$$f_{norm}(\tau) = \frac{1}{\sigma\sqrt{2\pi}} \exp(-\frac{(\tau-\tau_0)^2}{2\sigma^2}) \tag{6.2}$$

τ_0 is the peak of the lifetime distribution function and denotes thus the average lifetime of all lifetime modes. A direct fit to equation 6.1 is, however, very difficult to realize in practice due to infinite number of integrations. Therefore, two simplifications were made: The fit ranges between 0 and 20 ns; $d\tau$ is realized through fitting incrementally increasing τ values with a constant "step" in-between (Figure 6.2). The detailed algorithm and its corresponding codes are given in the Appendix B.

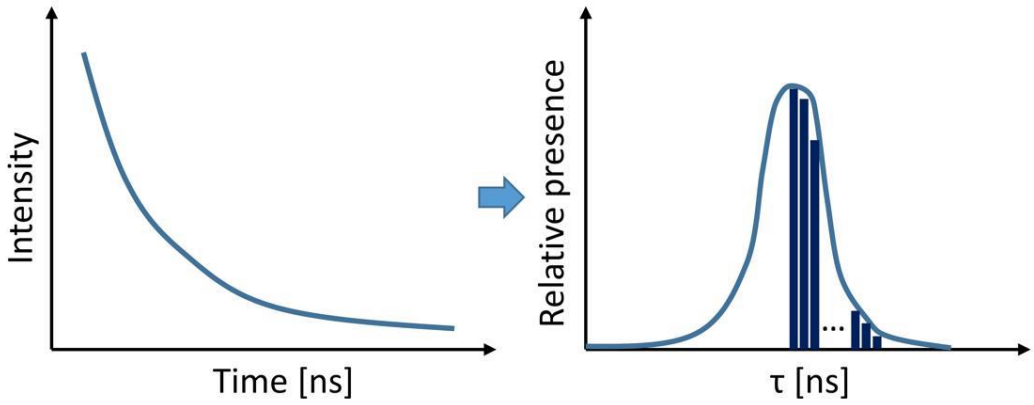

Figure 6.2: Schematic illustration of fitting the lifetime decay pattern (left) using a normal distribution function (right). The dark stripes denote different lifetime modes.

Similarly, the fluorescence lifetime of HSA at 675 µM (45 mg mL^{-1}) is fitted with a log-normal distribution function by:

$$\mathrm{I(t)} = \mathrm{A_2} \int_0^\infty f_{lognorm}(\tau) \cdot \exp(\frac{-t}{\tau}) d\,\tau + B_2 \tag{6.3}$$

A_2 is a scaling factor, and B_2 the background. t is the arrival time of photons, and τ the lifetime. $f_{lognorm}(\tau)$ is the log-normal distribution function:

$$f_{lognorm}(\tau) = \frac{1}{\tau\sigma\sqrt{2\pi}} \exp(-\frac{(\ln\tau-\tau_0)^2}{2\sigma^2}) \quad (6.4)$$

A log-normal distribution function is used here for HSA instead of a normal distribution in the case of pure AF633, because the fluorescence intensity of HSA decays significantly faster than AF633, loosing half its intensity within the first nanosecond. Therefore, the lifetime distribution of HSA is presumably to be asymmetric, with more modes in the faster lifetime region and less modes in the slower lifetime region. This is mathematically described by the log-normal distribution presented above.

6.2.2.1 Pure AF633

We first discuss the lifetime property of the dye AF633, free and attached to *p*HPMA-Chol (*p*HPMA-Chol*), the lifetime decay patterns of which are shown in Figure 6.3a and b, together with the fits, respectively. The fits are prefect in both cases. It is also worth noting that for *p*HPMA-Chol* the fit is better when using the distribution method than the single exponential decay (Figure 6.1). The resulting distribution functions are given in Figure 6.3c. It is clearly seen that the lifetime distribution function is significantly broadened when AF633 is attached to *p*HPMA-Chol (from σ = 0.24 ± 0.06 to σ = 0.66 ± 0.07 in equation 6.2), whereas the peak position does not vary (from τ_0 = 3.21 ± 0.01 ns to τ_0 = 3.19 ± 0.02 ns in equation 6.2). The broadening of the lifetime distribution can be explained by a change in the chemical environment of AF633 when covalently attached to *p*HPMA-Chol.

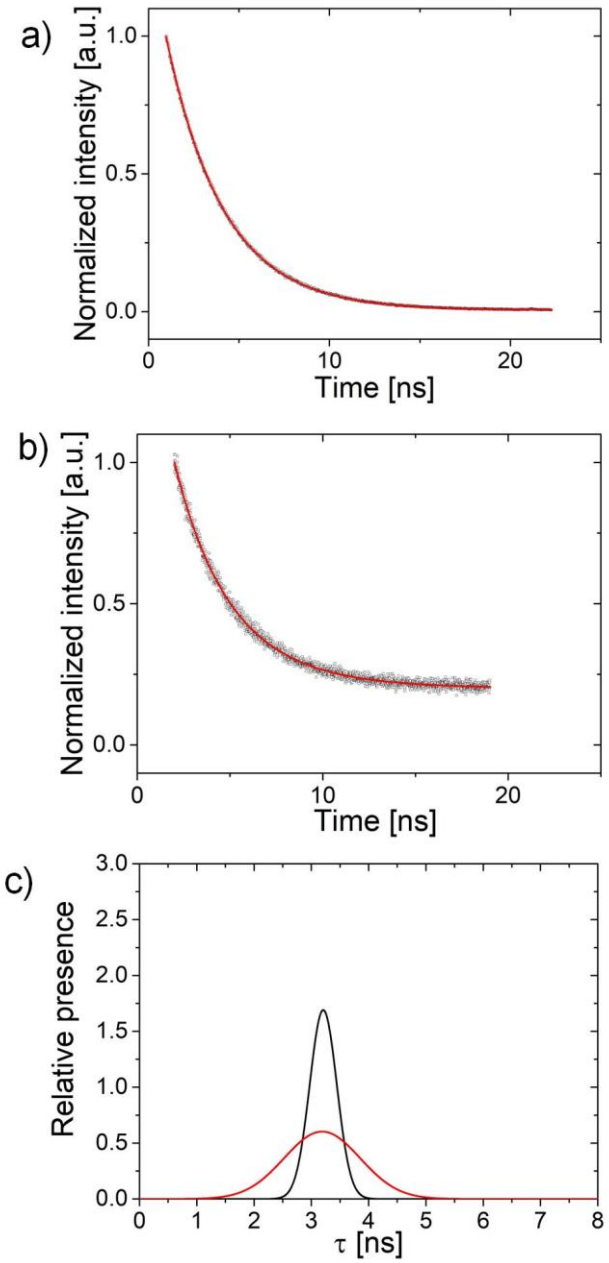

Figure 6.3: Fluorescence intensity decay of the dye AF633 (a) and of the dye AF633 covalently bound to *p*HPMA-Chol (*p*HPMA-Chol*) (b) both dissolved in PBS at a dye concentration of 10^{-8} M. together with the fits of a normal lifetime distribution (equation 6.1). The resulting normal distribution functions are given in (c): Black: AF633. Red: *p*HPMA-Chol*.

6.2.2.2. *p*HPMA-Chol* in the presence of HSA

As a reference, the lifetime decay pattern of a pure HSA solution was measured at a concentration of 675 µM, which is within its physiological range (Figure 6.4a), and was fitted using a log-normal lifetime distribution describing its rapid decay. The resulting lifetime distribution function is shown in Figure 6.4b, with $\tau_0 = 0.31 \pm 0.05$ ns and $\sigma = 1.16 \pm 0.08$ ns in

equation 6.4. We note here that the fluorescence signal obtained from the pure HSA solution cannot be directly attributed to HSA, which is known to be excited and to emit in the UV region, hence nearly impossible to be excited by the laser under experimental conditions (640 nm). The observed fluorescence is thus highly likely to be resulting from a tiny amount of other biological chromophores which are present in the commercial HSA and cannot be removed. Despite this, we will refer to the observed fluorescence by using the nomenclature "the fluorescence of HSA" hereafter.

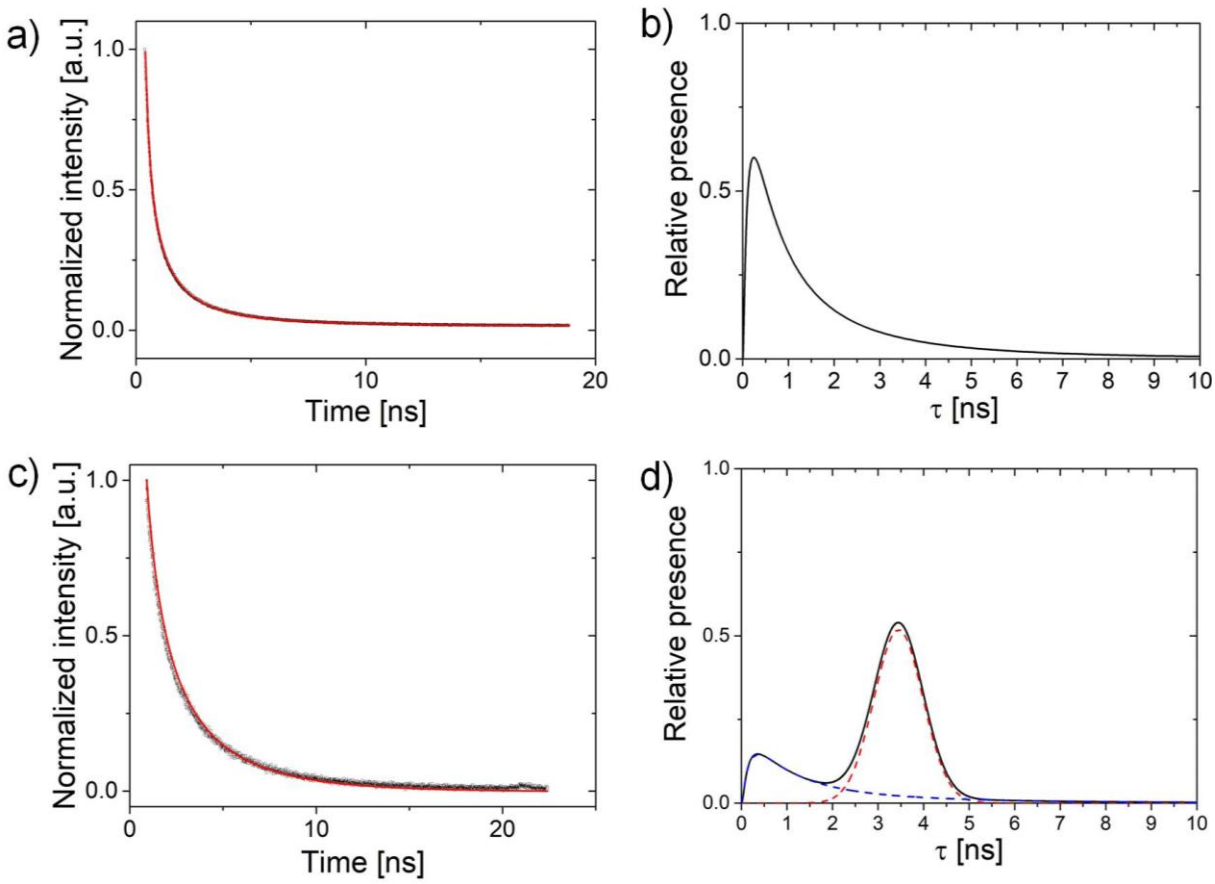

Figure 6.4: (a) Lifetime decay pattern of HSA at 675 µM in PBS. The resulting log-normal lifetime distribution function is given in (b). (c) Lifetime decay pattern of the mixed solution of *p*HPMA-Chol* having a dye concentration of 10^{-8} M and HSA at 675 µM in PBS. The resulting lifetime distribution functions are given in (d) with the respective contributions: blue: HSA; red: *p*HPMA-Chol*.

Subsequently, *p*HPMA-Chol* is dissolved in the HSA solution, and the lifetime decay pattern of this mixed solution is shown in Figure 6.4c together with the fit using a combination of two lifetime distribution functions of *p*HPMA-Chol* and of HSA, respectively. The fit is good over the whole time range. To simplify the fitting model, the lifetime distribution of HSA is kept the

same as in the pure HSA solution, which is appropriate because: The bandpass filter (690 ± 35 nm) placed before the detector is supposed to match the emission band of AF633 and significantly suppress the emission from HSA.

Figure 6.4d shows the resulting lifetime distribution function of *p*HPMA-Chol* in the presence of HSA. Upon mixing with HSA, it is found that the peak position of the *p*HPMA-Chol* shifted towards larger lifetime values (from to τ_0 = 3.19 ± 0.02 ns to to τ_0 = 3.45 ± 0.07 ns), whereas σ is not altered (from σ = 0.66 ± 0.07 to σ = 0.54 ± 0.06). A shift of lifetime towards lower values is normally due to collisional quenching of the fluorophores, whereas a shift towards larger values may result from secondary emissions due to re-excitation of the fluorophores which are already in their ground state. Therefore, in this system, it is possible that some of the AF633 dyes, which emit relatively fast (within the lifetime of HSA), can probably be re-excited by the emission of HSA, and thus the lifetime of AF633 becomes notably longer.

As mentioned earlier, the observed fluorescence emission from HSA cannot be fully attributed to the intrinsic fluorescence of HSA itself, since the presence of other biomacromolecular impurities, which absorb and emit in the yellow to red region, may contaminate the solutions spectroscopically. Nevertheless, this part of work helps to obtain spectroscopic information of the two species, which will be used immensely in the subsequent studies, namely pure HSA solution and *p*HPMA-Chol*, and to elucidate the fluorescence lifetime behavior of a complex system. Further experimental results on the fluorescence emission of HSA will be presented and discussed in the following chapter.

6.3. FLCS measurements

This chapter is based on ref. 179. Reprinted and adapted with permission. Copyright (2018) American Chemical Society.

To investigate the interaction between the *p*HPMA NPs and HSA using FLCS, the fluorescence emission from HSA as well as from Dox, must be suppressed sufficiently so that the resulting signal only originats from the dye AF633. Based on the experimental setup, two filtering methods are offered: (i) a bandpass filter which matches the emission wavelength of AF633; (ii) a digital filter which is generated based on the specific lifetime property of AF633. On the one hand, for the NPs without Dox, method (i) was used since the emission from HSA is at ca. 330 nm,[166] which is very far away from the one from AF633, which is at 647 nm. Therefore, the bandpass filter at 690 ± 35 nm is expected to suppress the emission from HSA thoroughly. On the other hand, for the NPs with Dox, methods (i) is no longer appropriate because Dox emits at ca. 600 nm which is close to the one from AF633.[180] Thus, method (ii) was used.

6.3.1. *p*HPMA-Chol-2 enriched by *p*HPMA-Chol* in the presence of HSA

For the FLCS experiments, *p*HPMA-Chol-2 (see Table 3.1 for characteristics) was chosen according to results from previous studies,[9, 10, 165] together with its fluorescently labelled analogue, *p*HPMA-Chol*, which contains 0.8 wt% of the far red dye AF633. Usually, one label per polymer chain or even less, or in other words, not all polymer chains are labeled, is enough for sufficient visualization of polymer both *in vitro* and *in vivo*. The low content of AF633, i.e. below 1 wt%, helps to avoid possible effects of the highly charged dye on the behavior of the polymer carrier. Also here the amount of the bound dye was sufficient for the characterization of the polymer and the formed NPs.

6.3.1.1. Diffusion behavior of the copolymer *p*HPMA-Chol*.

Using FLCS, a solution of the copolymer *p*HPMA-Chol* in PBS at a polymer concentration of 0.05 μM was measured as a reference. This polymer concentration corresponds to a dye concentration of AF633 of 0.01 μM, which is optimal for FLCS measurements. This polymer concentration is two magnitudes below the CMC, which is at ca. 5 μM based on results reported for similar copolymers,[107, 165] therefore NP formation is not expected. The autocorrelation functions obtained in three repetitions of the measurement are normalized by the number of molecules, *N*, and are shown in Figure 6.5 together with the fits of equation. 4.30 using $n_D = 1$. The curves feature two decays, which are attributed to the triplet state of the dye AF633 and

the diffusion of the copolymer chains, respectively. In the range of higher correlation times (> 0.1 ms), only slight variations of the curves are seen, indicating a consistency of the diffusion coefficients from the three measurements. The deviations in the range of lower correlation times (< 0.1 ms) are mostly due to variations of the amplitude, which is used for normalization of the curves by the average number of molecules in the confocal volume. By averaging the results obtained by fitting equation 4.30 to the three autocorrelation functions, a diffusion time τ_D = 0.213 ± 0.029 ms is obtained, giving a diffusion coefficient D = 57.9 ± 7.9 μm^2 s^{-1} using equation 4.31, corresponding to R_h = 3.7 ± 0.5 nm using the Stokes-Einstein relation (equation 4.32). The diffusion coefficient describes the translational diffusion of the dye AF633, which is covalently bound to the polymer chain, and is thus identical to the diffusion coefficient of the whole chain. Therefore, in the subsequent analysis of the autocorrelation functions of the mixed solutions of *p*HPMA-Chol-2 enriched with *p*HPMA-Chol* and HSA, this value is used for the free chains which are not associated with the NPs. In addition, some of the *p*HPMA-Chol* copolymers are associated with the NPs and can thus be used to characterize their diffusion behavior. The diffusion coefficient of the NPs is expected to be significantly smaller than the one of the non-assembled *p*HPMA-Chol*.

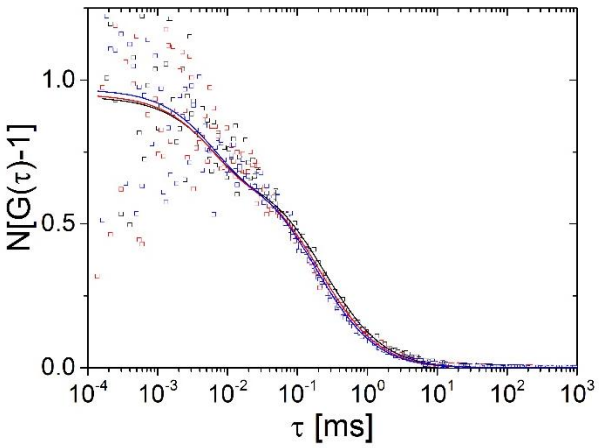

Figure 6.5: Autocorrelation functions (symbols) together with the fits of equation 4.30 (lines) from three FLCS measurements (shown in different colors) of *p*HPMA-Chol* in PBS. The polymer concentration is 0.05 μM, and the corresponding concentration of the dye AF633 is 0.01 μM. Reprinted with permission. Copyright (2018) American Chemical Society.

6.3.1.2. *p*HPMA-Chol-2 enriched with *p*HPMA-Chol* in the presence of HSA

To characterize the diffusion behavior of the dye-labelled *p*HPMA-chol NPs, the fluorescence emission from HSA, which hampers the characterization of the dye AF633, must be first carefully eliminated.

A bandpass filter (690 ± 35 nm) was mounted in front of the detector to suppress the fluorescence emission from HSA. To verify its function, the lifetime decay of a solution of *p*HPMA-Chol-2 enriched with *p*HPMA-Chol* (dye concentration: 0.01 µM) as well as the lifetime decay of a pure HSA solution (52 µM) were measured separately. The dye concentration is the same as in all mixed solutions that were measured using FLCS, and the concentration of HSA corresponds to the maximum value present in this part of the study. Despite a much higher concentration of HSA, it is obvious that the counts per second from HSA is much less than that from *p*HPMA-Chol-2 enriched with *p*HPMA-Chol* using the same instrumental setup (Figure 6.6). The fluorescence intensity ratio between *p*HPMA-Chol-2 enriched with *p*HPMA-Chol* and HSA is found to be 116:1 by integrating the two lifetime decay curves over the whole area. Therefore, for the mixed solutions of *p*HPMA-Chol-2 and HSA, the emission from HSA, which is still present through the bandpass filter, is expected to be at ca. 0.09% and 0.8% of the total emitted intensity, for HSA concentration at 5 and 52 µM, respectively (Figure 6.6 inset). Subsequent attempts were made to filter the remaining signal using a digital filter, where the overall lifetime decay pattern was fitted by a sum of the lifetime decay patterns of the pure AF633 dye and pure HSA. However, due to the strong contribution from AF633, reasonable fits could not be made. Nevertheless, this confirms that the HSA emission has been sufficiently suppressed by means of using only the optical bandpass filter.

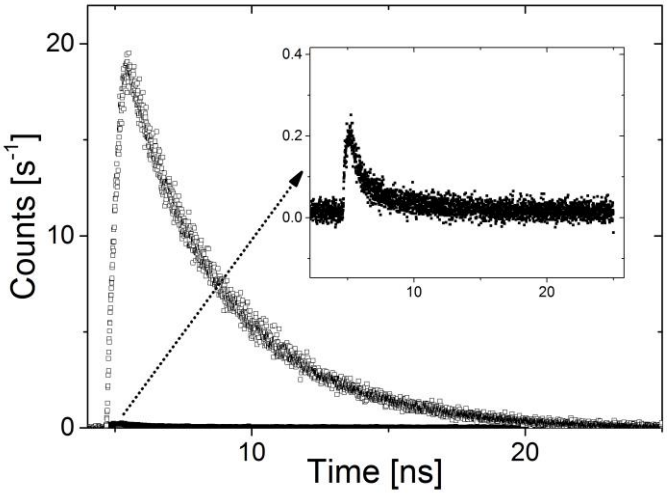

Figure 6.6: Lifetime decay patterns of a solution of *p*HPMA-Chol-2 enriched with *p*HPMA-Chol* (open symbols) and of a pure HSA solution (closed symbols). The concentrations of the dye AF633 and of HSA are 0.01 µM and 52 µM (3.5 mg mL^{-1}), respectively. The arrow indicates a zoom-in of the lifetime decay pattern of HSA visualizing its low intensity. Reprinted with permission. Copyright (2018) American Chemical Society.

*p*HPMA-Chol-2 enriched with *p*HPMA-Chol* (*p*HPMA-Chol-2/*p*HPMA-Chol*, molar ratio ranging from 1400:1 to 5600:1) was mixed with HSA having varied concentrations in PBS, and the resulting mixed solutions were measured by FLCS. Fluorescence backgrounds were discriminated and filtered out digitally, using the lifetime decay patterns obtained from the respective mixed solutions (see Appendix B).[145, 147]

The normalized autocorrelation functions of the mixed solution having a polymer concentration of 140 μM and a HSA concentration of 52 μM are shown exemplarily in Figure 6.7a. The autocorrelation functions overlap after normalization by the number of molecules, *N*, obtained from the fits using equation 4.30. Before this normalization, the autocorrelation functions differ from each other (Figure B.2, Appendix); the overlap after normalization indicates that the variations are mainly due to different amplitudes of the autocorrelation functions, which are inversely proportional to the average number of fluorescent molecules in the confocal volume, *N*. The curves and the fits using equation 4.30 for all other mixed solutions are shown in the Appendix (Figure B.2) and the resulting R_h values and the fractions of the slow decay in Figure 6.7b and c. It is noteworthy that all obtained autocorrelations are sufficiently well described using $n_D = 2$ in equation 4.30, namely two decays, which are attributed to the diffusion of the unassociated chains and the chains associated with the NPs, respectively. No large aggregates of the NPs are observed.

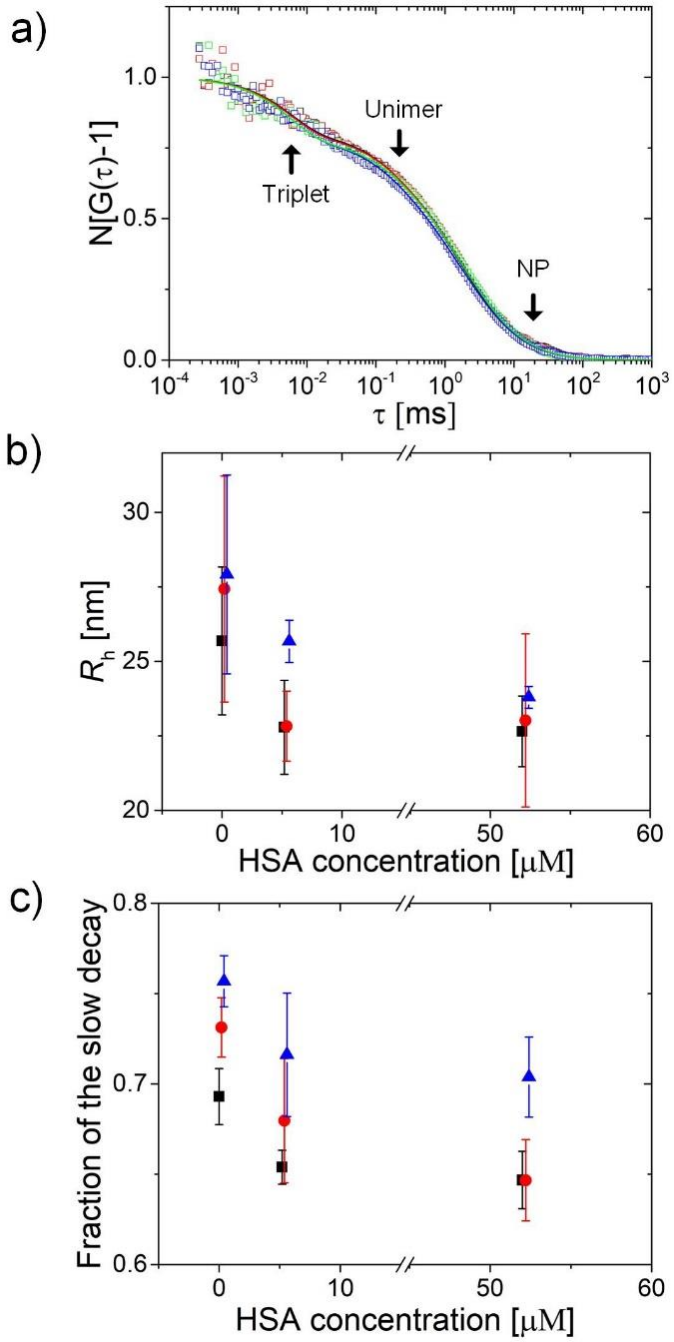

Figure 6.7: (a) Autocorrelation functions of the mixed solutions of *p*HPMA-Chol-2 enriched with *p*HPMA-Chol* and HSA having a polymer concentration of 140 μM and a HSA concentration of 52 μM, respectively. The dye concentration of AF633 is 0.01 μM. The colors of the curves indicate repetitions of measurements on the same sample. The arrows indicate the decay times of the triplet state of the dye, the diffusion of the unimers and the diffusion of the NPs, respectively. (b) R_h values of the NPs in the presence of HSA varied in dependence on HSA concentration. (c) The fraction of the slow decay, which corresponds to the fraction of the dye associated with the NPs. The polymer concentration in (b) and (c) is 35 μM (black squares),

70 μM (red circles) and 140 μM (blue triangles), respectively. Error bars in (b) and (c) are standard deviations resulting from repetitions of measurements. The data points are slightly offset along the concentration axis for clarity. Reprinted with permission. Copyright (2018) American Chemical Society.

Without mixing with HSA, NPs having an average R_h = 27.0 ± 3.2 nm were observed for all three polymer concentrations, i.e. 35, 70 and 140 μM, which is expected since these concentrations are all well above the CMC at ca. 5 μM.[107, 165] In the presence of HSA, the data indicate a slight decrease in R_h with increasing HSA concentration for all three polymer concentrations. At 55 μM HSA concentration, R_h is found at 23.2 ± 1.5 nm. This decrease, however, cannot be clearly resolved due to the large uncertainties. Thus, the R_h values of the NPs remain within the optimal range for the EPR effect (10–200 nm).[76] It is also found that the fraction of the slow decay increases with polymer concentration both in the presence and absence of HSA. This means that more NPs are formed at higher polymer concentrations. We thus conclude that the formation of NPs is not hindered by the presence of HSA. No increase of R_h is observed with HSA concentration, i. e. HSA does not form a static protein corona around the *p*HPMA NPs. These findings are in good agreement with the SAXS results presented in Chapter 5.2.3: Only tiny mismatches were observed in very low *q* region when modeling the SAXS curves from the mixed solutions using the scatterings from the individual components.

6.3.2. *p*HPMA-Chol-Dox-2 enriched with *p*HPMA-Chol* in the presence of HSA

Due to the overlap of Dox and AF633 in their emission spectra in the red region (> 600 nm), the bandpass filter at 690 ± 35 nm is no longer sufficient to eliminate the emission from Dox as well as from HSA. Digital filters based on the lifetime properties of the respective components, i.e. AF633, Dox and HSA, were thus employed. As described previously (Chapter 4.3.2), the digital filters are probability functions describing how likely a detected photon originates from a certain component. These functions are numerically converted from the results of the linear fit, where the overall lifetime decay pattern is fitted by a sum of all three patterns of AF633, Dox and HSA, respectively. To characterize the influence of HSA on the *p*HPMA NPs carrying Dox, these NPs were investigated in the presence of HSA having varied concentration using FLCS. The polymer concentration of *p*HPMA-Chol-Dox-2 was constant at 58.9 μM (2.56 mg mL^{-1}), which is safely above the CMC. The concentration of AF633 was the same one as previously (*p*HPMA-Chol-2 enriched with *p*HPMA-Chol*) at 10^{-8} M. Four HSA concentrations were chosen, ranging from 0.53 μM to 525 μM, to characterize its influence on the size of the NP.

The linear fits of the overall lifetime decay patterns and the correspondingly generated digital filters of two mixed solutions are exemplarily shown in Figure 6.8. For low HSA concentration at 52.5 μM (Figure 6.8a), the overall decay is dominated by the one of AF633 in the full time range, whereas the one of HSA contributes mainly to the first 10 ns. It is worth noting that the amplitude of the pattern of Dox is almost zero from the fit: There is no trace of fluorescence emission from Dox found in the mixed solution. Four digital filters were generated based on the fit shown in Figure 6.8a: The one of HSA has the highest amplitude only in the first several ns, followed by the one of AF633 which becomes predominant till ca. 15 ns. After this point, the filter of the background starts to grow continuously until the end of the data range. The filter function of Dox is either slightly negative or very close to zero in the full time range. Recalling that the physical meaning of a digital filter, the amplitudes of these filters can be translated into a scenario that a detected photon is highly likely to be emitted from HSA in the first several ns, from AF633 between 5 ns to 15 ns, or from the background starting from 15 ns. Meanwhile, there is hardly any photon likely to be emitted from Dox, which is expected, since Dox is mainly excited in the wavelength range of 400–600 nm, recalling that the excitation wavelength was 640 nm.

When the HSA concentration is 10 times higher, namely 525 μM (Figure 6.8c), interestingly, the fit indicates a clear presence of Dox emission rapidly after the start of the decay (< 2 ns). We attribute the presence of the Dox emission to the much higher HSA concentration. HSA is known to emit in the range of 300–450 nm with a peak at 330 nm.[23, 166, 181] It is thus reasonable that the emission from HSA can excite Dox and results in secondary emissions from Dox.[180] The generated digital filters resemble the ones in Figure 6.8b, since the emission of Dox is too weak to have any influence on the generated filter functions.

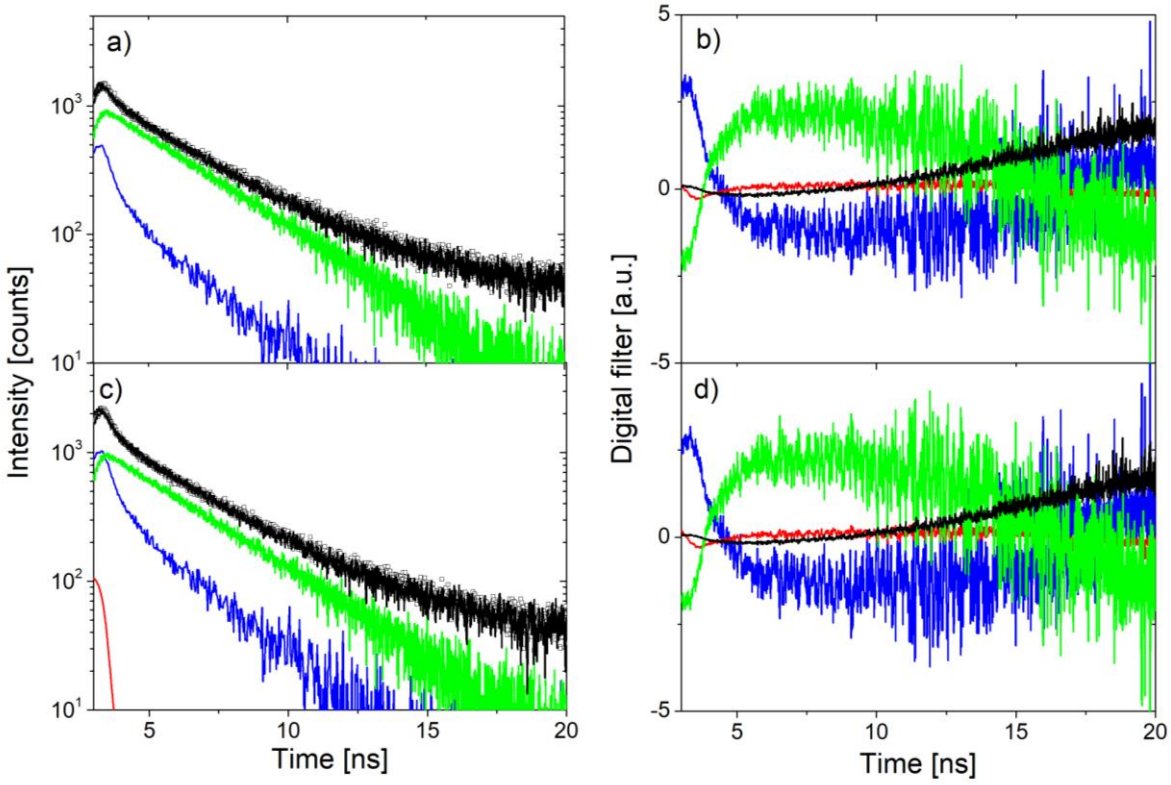

Figure 6.8: Examples of digital filters for different fluorescence species generated based on their respective lifetime properties. The concentration of *p*HPMA-Chol-Dox-2 was constant at 58.9 µM (2.56 mg mL^{-1}). The concentration of HSA is 52.5 µM in (a,b) and 525 µM in (c,d), respectively. The lifetime decay patterns (a,c) and corresponding digital filters (b,d) are distinguished by their colors: Black: Overall; Green: AF633; Blue: HSA; Red: Dox.

Figure 6.9a shows the normalized autocorrelation functions of different mixed solutions having varied HSA concentration together with the fits using equation 4.30. These autocorrelation functions were calculated by employing the digital filters of AF633 generated from the respective solutions, and thus carry information only of *p*HPMA-Chol*.

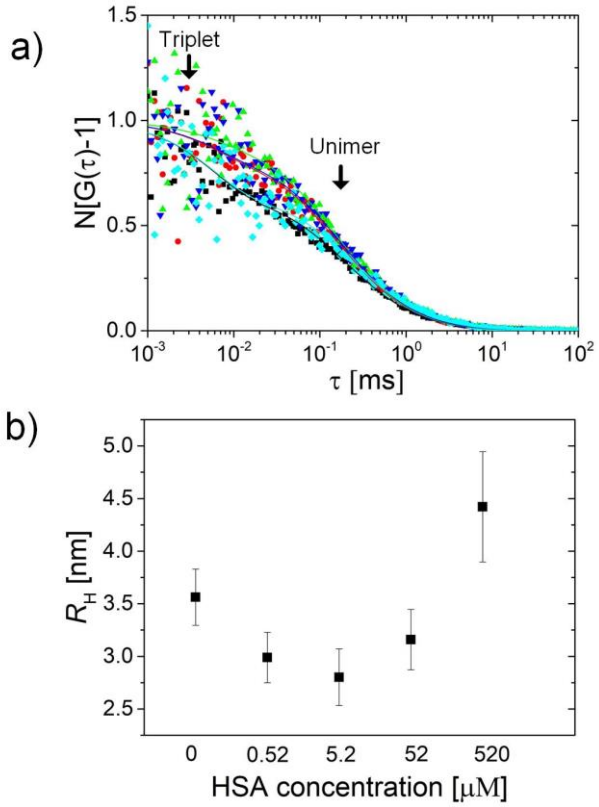

Figure 6.9: (a) Normalized autocorrelation functions (symbols) of *p*HPMA-Chol-Dox-2 enriched with *p*HPMA-Chol* in the presence of HSA, together with the fits using equation 4.30 (lines). The autocorrelation functions were calculated using the digital filters generated for AF633 based on its lifetime properties obtained from the respective mixed solution. The concentration of *p*HPMA-Chol-Dox-2 was constant at 58.9 μM (2.56 mg mL^{-1}). The concentration of HSA is indicated by colors: 0, black; 0.52 μM, red; 5.2 μM, green; 52 μM, blue; 520 μM, cyan. (b) R_h values observed in dependence on HSA concentration.

All autocorrelation functions feature two diffusional decays: One at ca. 0.005 ms and another one at ca. 0.2 ms. In contrast to the *p*HPMA-Chol system, where a third decay at ca. 2 ms was observed (Figure 6.7a) due to formation of NPs, the *p*HPMA-Chol-Dox-2 system does not show a third decay. Therefore, we fitted all obtained autocorrelation functions using equation 4.30 with $n = 1$. The resulting R_H values calculated using the Stokes-Einstein equation are shown in Figure 6.8b. It is seen that all observed R_H values are within the size of 3–5 nm, which are too small to originate from the *p*HPMA NPs. This means that only the free unimers are observed using the experimental setup. A small increase in R_H was observed at high HSA concentration, namely 525 μM, which suggests the possibility of complexation of HSA to the polymer chains. Based on our previous SAXS result, the Dox-carrying copolymers do form NPs under similar experimental conditions, namely polymer concentration and temperature. Therefore, we

attribute the absence of the NPs to the mathematical treatment to the autocorrelation functions using digital filters. In other words, we suspect that the complexity of the current system is beyond the capability of the FLCS instrument in terms of separating autocorrelation functions using the lifetime properties of the individual components. Therefore, for FLCS measurements where multiple fluorescent components and NPs of large size are present, simple bandpass filters seem to offer a more reliable and direct solution.

6.4. Fluorescence quenching

Since no change of particle size was observed, neither in our SAXS experiments,[165] nor in the FLCS results discussed above, the formation of a hard HSA corona on the NPs is highly unlikely. However, these results do not exclude the possibilities of the following interaction types: (i) HSA may form complexes with the unimers (free *p*HPMA-Chol chains that are not associated to the NPs). This type of complexation is expected to give a rise in the hydrodynamic radius of the free chains, leading to a longer diffusion time of the first fast decay mode in the FLCS measurements. However, we did not observe any significant change in the fast decay mode in the *p*HPMA-Chol system. First, it is mainly due to the fact that the molar ratio between the unimers and NP is ca. 3:7 (Figure 6.7c), meaning that the autocorrelation functions are "more sensitive" to size changes of the much larger NPs instead of the smaller chains. Second, HSA is small as well with a radius of gyration of 2-3 nm (Chapter 5.2.1).[165] The complexation of few HSA molecules on a unimer may result in an increase in size which is too small to be sensed. (ii) A few HSA molecules become trapped in the meshes and entanglements of the NP shell. Similarly, this leads to a trivial increase in the NP's size and is in practice very difficult to be resolved using FLCS. However, both scenarios can be identified using additional fluorescence spectroscopic methods, such as fluorescence quenching.

Fluorescence quenching refers to a decrease in the steady-state fluorescence intensity, which may be due to either a static or a dynamic quenching process. A static quenching process involves complexation of a fluorophore and other ligand, resulting in a ground state complex which is no longer fluorescent, hence a decrease observed in steady-state fluorescence intensity. In case of a collisional quenching, the quencher must diffuse to the fluorophore within its lifetime. Upon collision, the fluorophore returns to its ground state, without emission of a photon. By observing the steady-state fluorescence intensity of HSA mixed with *p*HPMA-Chol-2 at different polymer concentrations, the possible complexation of HSA and *p*HPMA NPs can be analyzed quantitatively.

The concentration of HSA used in similar studies was commonly chosen below 5 μM, where the fluorescence of HSA is quenched.[157, 158] In the present study, a higher value of HSA concentration was used in all mixed solutions, i.e. 15 μM, such that there is enough free HSA which may interact with the NPs by means of, for instance, protein corona formation. Figure 6.10a shows the emission spectra of HSA in the presence of *p*HPMA-Chol-2, having concentrations in the range of 0.9–70 μM. This polymer concentration range, which covers the

regions both below and above the CMC, was chosen for two reasons: First, the influence of the micellization on the interactions between HSA and the *p*HPMA system can be identified. Second, the interaction type between HSA and the unimers may differ from the one between HSA and the NPs. For application, there is a constant presence of the unimers in blood independently on the polymer concentration. It is thus vital to understand how these unimers interact with HSA. It is found, that with increasing *p*HPMA-Chol-2 concentration, the fluorescence intensity of HSA decreases (Figure 6.10a). Steady-state fluorescence intensities were obtained by integrating over the whole area under the respective curve, and the corresponding Stern-Volmer plot (F_0/F against the polymer concentration) of the fluorescence intensity is given in Figure 6.10c.

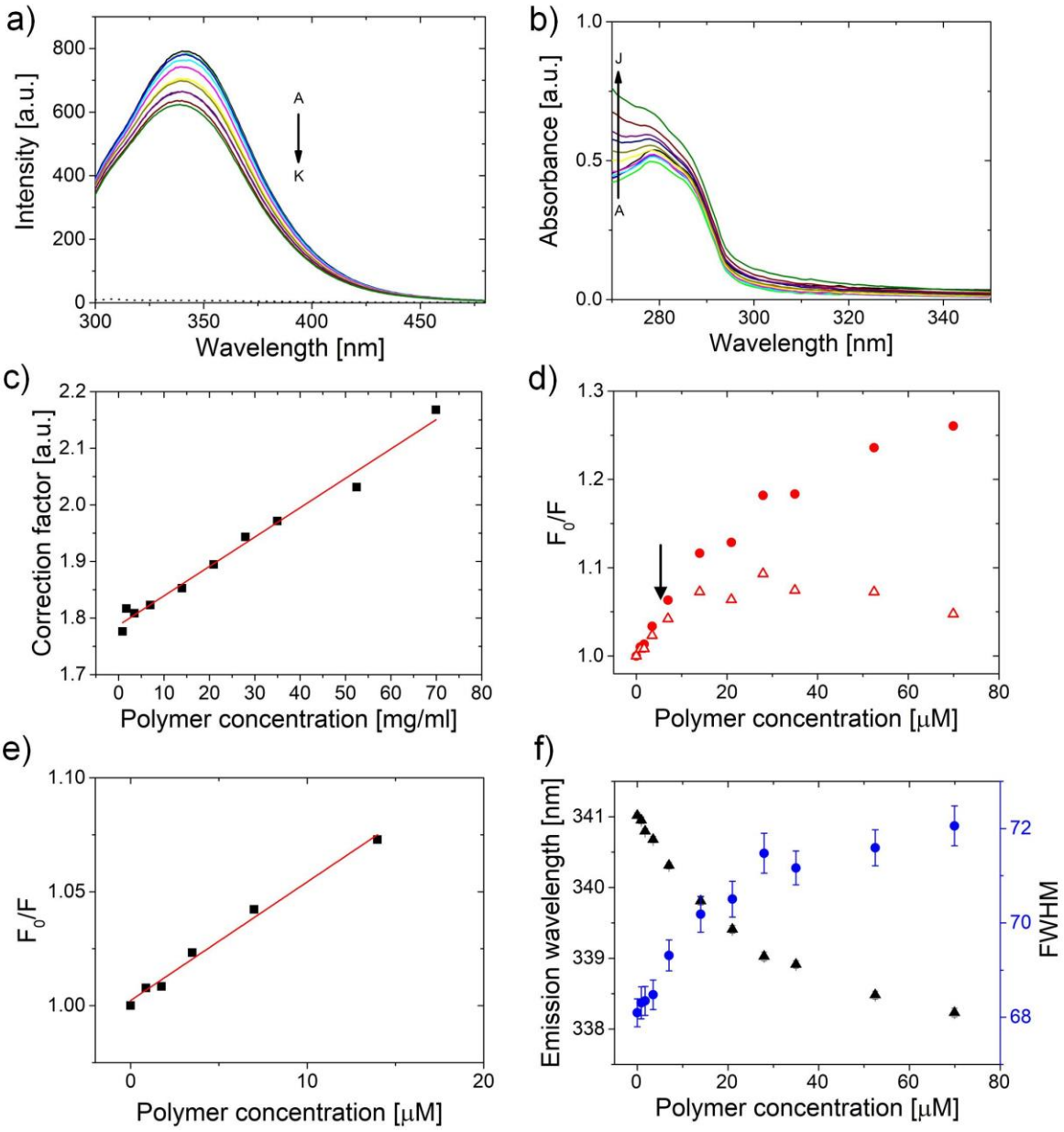

Figure 6.10: (a) Fluorescence spectra of HSA (uppermost curve, A) with increasing concentration of *p*HPMA-Chol-2 (curves B-K, 0.9–70 μM). The spectra were obtained with 15 μM HSA in PBS at an excitation wavelength of 280 nm. The fluorescence spectrum of a pure *p*HPMA-Chol solution at 140 μM is shown as a dotted line. (b) UV-Vis spectra of the mixed solutions of HSA and *p*HPMA-Chol-2, measured at different polymer concentrations (A-J: 0.9–70 μM). (c) Linear fit to the correction factors obtained at each polymer concentration calculated using equation 4.39. The pure HSA solution was excluded from the linear fit region, to get rid of any effect on HSA's absorbance due to interaction between HSA and *p*HPMA-Chol-2. (d) Stern-Volmer plot for the fluorescence quenching data of the mixed solutions of *p*HPMA-Chol-2 and HSA. Red triangles and circles: F_0/F values with and without correction of the inner-filter effect, respectively. (equation 4.39). The black arrow marks the CMC of *p*HPMA-Chol-2. (e) Stern-Volmer analysis of the linear region of Figure 6.10d using equation 4.38. (f) Emission peak (black triangles) and FWHM (Full width at half maximum, blue circles) of the HSA spectrum in dependence on polymer concentration. The parameters were obtained by fitting single Gaussian peaks to the fluorescence spectra of HSA (equation 4.42).

It is important to note that a main confounding factor in fluorescence quenching experiment is the inner-filter effect, which refers to a loss in the steady-state fluorescence intensity due to the absorbance of the incident light and the emitted light from fluorophores by the quencher molecules. The UV-Vis spectra of the mixed solutions (Figure 6.10b) demonstrate a significant increase in the absorbance with polymer concentration, indicating that the influence of the inner-filter effect must be taken into account before any conclusion can be drawn from the Stern-Volmer plot. The correction factors were calculated in dependence on the polymer concentrations by equation 4.39 using the corresponding absorbance at the excitation and emission wavelength of HSA, i.e. at 280 nm and 334 nm, respectively, where a very good linearity is seen (inset of Figure. 6.10c). The respective correction factors were obtained by a linear fit to the data and subsequently applied to the steady-state fluorescence intensities, resulting in a Stern-Volmer plot of the corrected intensities (Figure 6.10d).

After the correction, F_0/F features a rapid linear increase up to a polymer concentration of ca. 15 μM, demonstrating a quenching process. At higher polymer concentrations (>15 μM), F_0/F becomes constant, indicating that the fluorescence intensity of HSA is not further quenched by the additional copolymer.

Let us first assume the quenching to be caused by collisions between HSA and the polymer. To quantitatively analyze the quenching, equation 4.33 was first fitted to the data in the linear

region of F_0/F, i.e. at a polymer concentration of 0–14 μM (Figure 6.10e). The slope of the fit gave the Stern-Volmer constant, $K_D = (5.4 \pm 0.3) \times 10^3$ M^{-1}. To obtain the bimolecular quenching rate constant using equation 4.33, the fluorescence lifetime of free HSA (unquenched) must be a priori known. Despite the presence of three fluorophores in HSA, namely tryptophan, tyrosine and phenylalanine, the fluorescence emission from HSA is mainly due to tryptophan. The other two fluorophores hardly contribute to the overall intensity due to their very low quantum yield (phenylalanine) or because they are easily quenched (tyrosine).[181] Numerous investigations have addressed the tryptophan lifetime in HSA in both free and quenched conditions:[182-188] The heterogeneous lifetime of tryptophan was found in the range of 2–6 ns with two exponential decay modes ($n = 2$ in equation 4.40.).[183-187] Using equation 4.33, one obtains a value of k_q in the order of 10^{12} s^{-1} M^{-1}. This value is far beyond the limit of a diffusion-controlled bimolecular rate which is normally in the range of 10^9–10^{10} s^{-1} M^{-1}. Furthermore, based on the diffusion coefficient of *p*HPMA-Chol*, $D = 57.9 \pm 7.9$ μm^2 s^{-1}, which was obtained earlier using FLCS, the maximal distance which a *p*HPMA-Chol-2 chain can travel within 6 ns is ca. 0.8 nm, which makes it impossible for *p*HPMA-Chol-2 to diffuse to HSA and quench it through collision. Based on these discussions, the observed quenching process must be a static one. In this case, the obtained Stern-Volmer constant is equivalent to the association constant describing complexation between *p*HPMA-Chol-2 and HSA, i.e. K_S = [*p*HPMA-Chol-2|HSA]/([*p*HPMA-Chol-2] × [HSA]) = $(5.4 \pm 0.3) \times 10^3$ M^{-1}, where "|" denotes complexation (equation 4.37).

Interestingly, the observed static quenching seems to reach its saturation at high polymer concentration values (> 20 μM), which is counterintuitive, since the Stern-Volmer theory predicts that the number of quenched fluorophores increases linearly with quencher concentration. This phenomenon of a hindered quenching efficiency clearly points to a loss in the number of quenching sites at high polymer concentration. As the polymer concentration increases beyond the CMC, the polymers form micelles (NPs). Most of the cholesterol moieties are no longer exposed and accessible to HSA but protected by the *p*HPMA chains. Therefore, it is reasonable that the static quenching of HSA is attributed to the complexation between cholesterol side groups and HSA, which has been previously reported using circular dichroism and fluorescence quenching methods.[172, 178] Considering that there are on average ca. 4 cholesterol side groups on each chain, we obtain a new association constant describing the binding of HSA to the cholesterol side groups in the linear region of the Stern-Volmer plot (Figure 6.10d), which is K_S = [Chol|HSA]/([Chol] × [HSA]) = $(1.4 \pm 0.08) \times 10^3$ M^{-1}. Reasonably,

this value lies below the one observed for HSA binding to free cholesterol, which is (2.3 ± 0.3)×10^3 M^{-1}, because the cholesterol groups in the present study are tethered to the chains.

Furthermore, a weak blue shift together with a broadening of the emission peak of HSA at ca. 340 nm with increasing polymer concentration was observed (Figure 6.10f). A blue shift of the fluorescence emission is normally due to a change of the environment of the fluorophore from polar to non-polar, which reduces the effect of solvent relaxation.[189] This corresponds to a scenario where the polarity of the environment of HSA, which is mainly due to the polarity of water molecules, decreases, when it forms complex with *p*HPMA-Chol-2 (Figure 6.11). In addition to that, the slight broadening of the emission peak of HSA (Figure 6.10f) is another evidence of multiple HSA locations, namely free in water, bound to cholesterol side groups on the unimers, or even in the outer shell of the NPs (see Chapter 2.1). Recalling the fact that the cholesterol groups are randomly distributed along the chain, the surface of the NPs is presumably rough and locally irregular. HSA can hence enter the NP and bind to those few cholesterol moieties which are distributed across the hydrophilic shell. Nevertheless, since the changes of the peak position and the peak width are only minor, the number of HSA molecules, which enter the NP through this manner, is presumably very low.

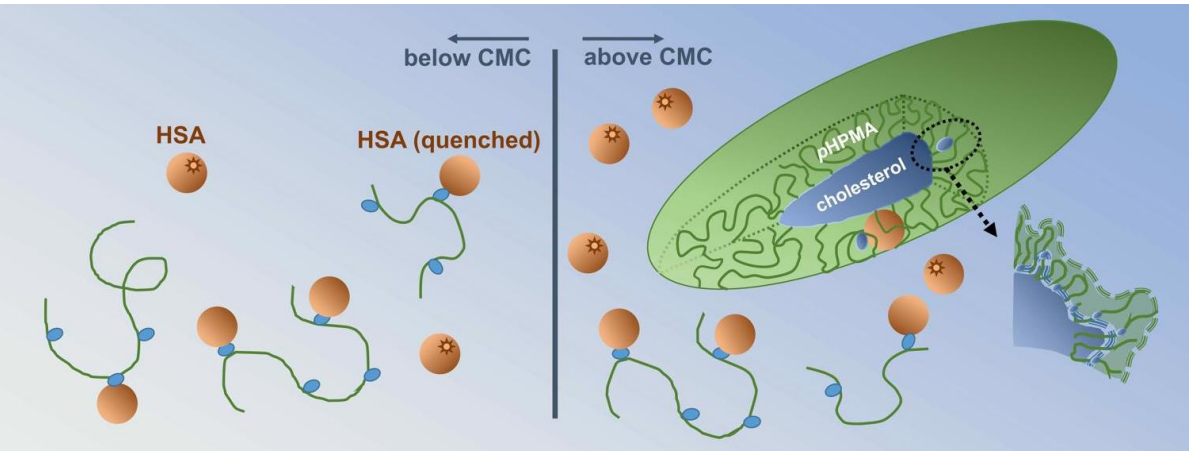

Figure 6.11: Schematic sketch of the fluorescence quenching of HSA by binding to the cholesterol side groups on *p*HPMA-Chol-2 below its CMC. Above the CMC, most cholesterol groups are protected in the NP core and thus free from such binding. However, it cannot be excluded that few HSA enters the NP and bind to the cholesterol groups which are randomly located in the shell. Reprinted with permission. Copyright (2018) American Chemical Society.

6.5. Conclusion

An investigation of the interaction between the drug delivery NPs formed by the amphiphilic *p*HPMA-Chol-2 and HSA in aqueous solution was carried out using a combination of FLCS and fluorescence quenching methods.

*p*HPMA-Chol carrying the fluorescent dye AF633 is used as a label of the NPs. The fluorescent signal from HSA was suppressed by an optical bandpass filter which matches the emission spectrum of AF633. The mixed solutions of *p*HPMA-Chol NPs and HSA were measured by FLCS at varied concentrations. For all three polymer concentrations, i.e. 35, 70 and 140 μM, NPs having R_h around 27 nm were observed. For three investigated polymer concentrations, it was found that R_h of the NP remained when HSA was present. It is unlikely that HSA forms a protein corona surrounding the NPs. The same strategy to label the NP was used for the Dox-carrying copolymer *p*HPMA-Chol-Dox-2, which was mixed with HSA having concentrations ranging from 0.52 to 525 μM, with the latter being its physiological value. Due to the overlap of the fluorescence emission of Dox and AF633 in the emission spectrum, the discrimination of the fluorescence of the dye was no longer able to be fulfilled by the bandpass filter. Instead, digital filters, which are generated using the lifetime properties of the individual components, were in use. The such generated digital filter of the dye AF633 was applied to all autocorrelations, resulting in filtered autocorrelation functions which carry diffusional information only of the dye. However, due to the complexity of the system, we suspect that these digital filters do not work properly since no NP but only unimers are observed, which is in controversy with our previous results obtained using SAXS.

Subsequently, a fluorescence quenching experiment was carried out, where the intrinsic fluorescence of HSA was used as a probe to address the previously reported weak interaction between HSA and *p*HPMA-Chol NPs. The observed quenched fluorescence of HSA below the CMC of *p*HPMA-Chol-2 was characterized as a static quenching process resulting from the complexation between HSA and the cholesterol side groups. The blue shift and broadening of the emission spectrum of HSA suggested a change of environmental polarity of HSA, which was explained by multiple HSA locations, i.e. free HSA, HSA bound to *p*HPMA-Chol-2 and HSA bound to cholesterol in the NP shell.

These results indicate that the drug delivery using the *p*HPMA-based NPs is not affected by HSA, since only the unassociated unimers (free chains) are affected by HSA through binding to cholesterol side groups.

7. Summary and conclusion

This thesis addresses the interaction between the *p*HPMA NPs, which are potentially nano drug carriers against solid tumor, and proteins from human blood plasma, towards a more realistic environment in which the drug carriers are investigated. At this, we gain knowledge on the behavior of the *p*HPMA system in protein environment, as well as general knowledge and rules in designing future drug delivery systems.

In the first part of the thesis, we concentrated on detecting possible interactions between the *p*HPMA NPs and HSA, by investigating the mixed solution of the NPs and HSA in PBS using SAXS, SANS and ITC. For this purpose, two polymer systems, which share the same backbone structure from HPMA and are decorated by cholesterol moieties, were used: *p*HPMA-Chol, which does not carry the anti-cancer drug Dox, and *p*HPMA-Chol-Dox, which carries Dox. We firstly analyzed the pure polymers which were not yet mixed with HSA. Using SAXS, it was found that both copolymers self-assemble into ellipsoidal NPs above the CMC in PBS. The size of the NPs was found to be very weakly dependent on the polymer concentration. Only at relatively high polymer concentrations (> 2 mg mL^{-1}), the NPs were slightly larger. The R_g of a single HSA molecule was found to be 27 Å at the physiological concentration of 35 mg mL^{-1}. At low HSA concentrations, apparently larger R_g values were observed, which were attributed to the presence of HSA dimers as proved by AUC and SAXS data. Then, the *p*HPMA-Chol and *p*HPMA-Chol-Dox system were mixed with HSA in PBS, respectively, in a way that both the polymer concentration and the HSA concentration were varied in a wide range. The SAXS curves of the mixed solutions of the *p*HPMA NPs and HSA were modeled using a combination of the form factors of the pure NP and HSA, where it was concluded, that HSA binds to the NPs without Dox. As a complementary to SAXS, in which the scattered intensity from the bound HSA was superposed by the dominant unbound ones, and thus cannot be clearly resolved, ITC gave signal resulting from the binding events. From the ITC results, the influence of Dox was clearly discriminated: The binding of HSA to the NPs was strongly hindered when Dox is present in the NPs. This conclusion was further supported using solvent matching in SANS, where the secondary structure of HSA was observed to be altered by the NPs without Dox.

The second part of the thesis was devoted to characterizing the nature of the binding of HSA to the NPs. To distinguish properly the NPs in the presence of HSA in the mixed solution, fluorescence labeling was employed: A fluorescent dye AF633 was covalently bound to the

backbone, which facilitates the investigation using FLCS. Despite the fact, that both HSA and Dox, are fluorescent and may hamper the clear distinction of the dye, FLCS exploits the fluorescence lifetime properties of the individual components and is able to calculate the autocorrelation function based on the photons emitted solely from the dye. From FLCS results, unaltered hydrodynamic radii of the NPs with or without Dox were observed, when exposed to HSA environment. The formation of protein corona, which is a layer of proteins surrounding the NP, is thus excluded. Furthermore, the digital filters did not work properly for the system with Dox.

Recalling the fact that HSA is intrinsically fluorescent, its fluorescence spectrum was recorded in dependence on the polymer concentration of the one without Dox. The emission of HSA decreases with increasing concentration of polymer. After carefully examining the impact of the inner-filter effect on the emission spectrum, the decrease in intensity was attributed to fluorescence quenching. By analyzing the dependence of the fluorescence lifetime of HSA on the polymer concentration, the quenching process is characterized as a static one. In other words, HSA interacts mainly with the unimers by binding their cholesterol side groups.

Combining the above-mentioned results obtained from the mixed solutions of HSA and the *p*HPMA NPs, on the one hand, we conclude, that HSA, the most abundant protein from human blood, only weakly binds to the NPs. However, it is important to note that the binding does not influence the function of the NPs in delivering drug to the solid tumors, since no significant change in the size of the NPs was observed. It thus still fulfills the requirement of the EPR effect. On the other hand, the "stealth" function the *p*HPMA shell of the NPs shed light on the future design of nano drug carriers: by using a tiny amount of highly hydrophobic material, e.g. cholesterol, through which a very high hydrophilic fraction is achieved. This way, the interactions between the NPs and blood proteins are expected to be minimized.

Also used as platform for drug delivery, poly(2-oxazoline) was first present in the 1990s and lay dormant for almost two decades.[190] In recent years, it came back to the focus for next-generation polymer therapeutics, through intensive studies on its physicochemical properties under biological conditions.[191-193] In comparison, despite the huge number of investigations on *p*HPMA-based drug delivery systems, seldom has addressed its biocompatibility issue in terms of protein adsorption. Therefore, our research shed light on the future of the therapeutics based on the relative "old" *p*HPMA copolymers, by giving a full physical investigation on its behavior in the presence of protein from human blood. There are admittedly more aspects, which must be considered in the future, due to the complexity of real blood. This work, however, has paved

the way for characterizing complex systems addressing NPs and proteins in the fields of bio- and polymer physics.

Appendix A. Supporting information for Chapter 5

SAXS curve of *p*HPMA-Hyd

The SAXS result of the simplest structure, i.e. the water soluble *p*HPMA-Hyd, which does not contain hydrophobic groups, is presented in Figure A.1. Due to a lack of hydrophobic segment, *p*HPMA-Hyd is expected to behave similarly to ideal polymer chains in theta solvent described by a spatial averaged size, the radius of gyration R_g. In Figure A.1, two SAXS curves from *p*HPMA-Hyd having different polymer concentrations, i.e. 10 and 20 mg mL^{-1} are shown. The two curves coincide over the full q range after normalization by their concentration, indicating that the structure of these chains is not concentration-dependent. The curve at 20 mg mL^{-1} is modeled by the Debye function (equation A1), which describes the scattering from an ideal chain. The fit gives R_g = 61 ± 2 Å. The Debye function is given by:

$$D(x) = 2(e^{-x} + x - 1)/x^2 \quad \text{(A1)}$$

with the expression $x=(qR_g)^2$, where R_g is the radius of gyration.

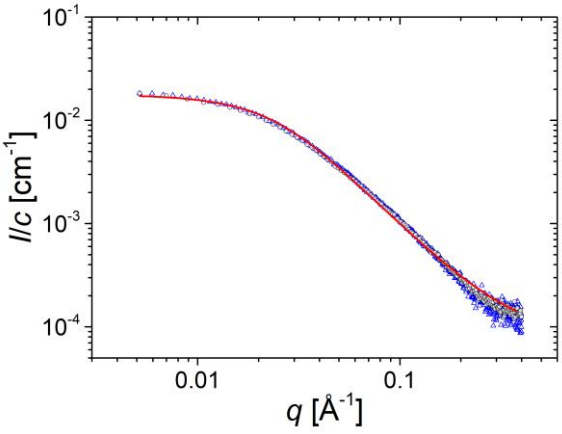

Figure A.1: SAXS curves of the water soluble *p*HPMA-Hyd having concentration of 10 mg mL^{-1} (blue triangles) and 20 mg mL^{-1} (black circles) in PBS. Curves are normalized by their concentration. The red curve is the fit to the curve at 20 mg mL^{-1} using the Debye function.

Analytical Ultracentrifugation (AUC) result on pure HSA solutions

This section is based on ref. 194.

The sedimentation analysis of human serum albumin (HSA) solutions was performed using a ProteomeLab XL-I analytical ultracentrifuge equipped with an An50Ti rotor (Beckman Coulter, USA) at a 0.7 or 0.233 mg mL^{-1} total loading concentration in 0.05 M sodium

phosphate and 0.15 M NaCl buffer (pH 7.4), which was also used as a reference. The sedimentation velocity experiments were carried out at 50000 rpm and 20 °C; the absorbance scans were recorded at 230 nm in 10 min intervals, with 30 μm spatial resolution. The sedimentation equilibrium experiments were carried out at 24000, 28000, 32000, 36000, 40000, 44000 and 48000 rpm and 20 °C, while the absorbance scans were recorded at 230 nm in 18 h intervals, with a 10 μm spatial resolution. The buffer density and peptide partial specific volumes were estimated in SEDNTERP. The data were analyzed with SEDFIT and SEDPHAT.[195, 196]

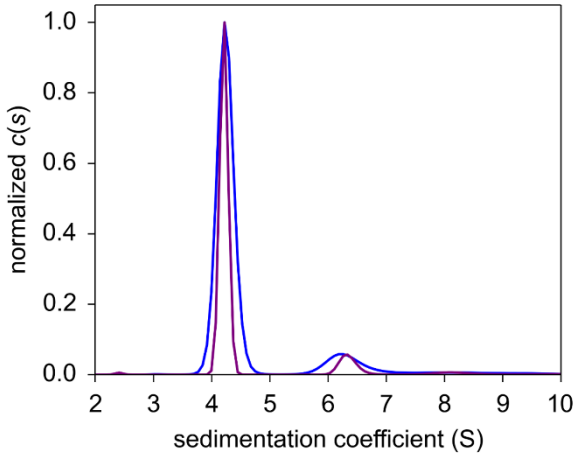

Figure A.2: The distribution of sedimentation coefficients for HSA (0.5 mg mL^{-1}) recorded using interference (IF, blue) and absorption (Abs, purple) modes.

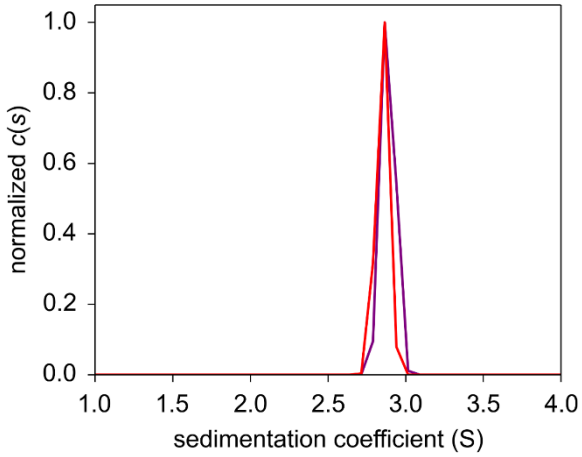

Figure A.3: The distribution of sedimentation coefficients for HSA (40 mg mL^{-1}) recorded using the interference mode. The sample was measured 2 times, which is indicated by the different colors.

In the distribution function of the sedimentation coefficient for the 0.5 mg mL^{-1} HSA solution, the HSA dimers are clearly seen as a second peak in the region of $6 < S < 7$ (Figure A.2). At 40 mg mL^{-1}, only a single peak is observed and the HSA dimers are thus absent (Figure A.3). The shift of the peak to a lower S value is caused by the crowding effect in solution due to the high concentration. These findings are in good agreement with the SAXS results on the pure HSA solutions (Chapter 5, Figure 5.2), where R_g = 27.4 ± 0.2 Å is observed at 35 mg mL^{-1} which matches well the value of HSA monomer. Larger R_g values due to the presence of dimers are observed at low HSA concentrations i.e. at 0.35 and 3.5 mg mL^{-1}.

Fit of the SAXS curve of *p*HPMA-Chol-1 by a form factor for spherical particles

To fit the SAXS curves of *p*HPMA-Chol-1, different models were tried, and the best and simplest fit is obtained using the form factor of an ellipsoid. An example of the fit using a form factor for spheres is given in Figure A.4. The data could not be properly modeled in the low q region, together with some deviations from the shoulder at ca. 0.05 $Å^{-1}$.

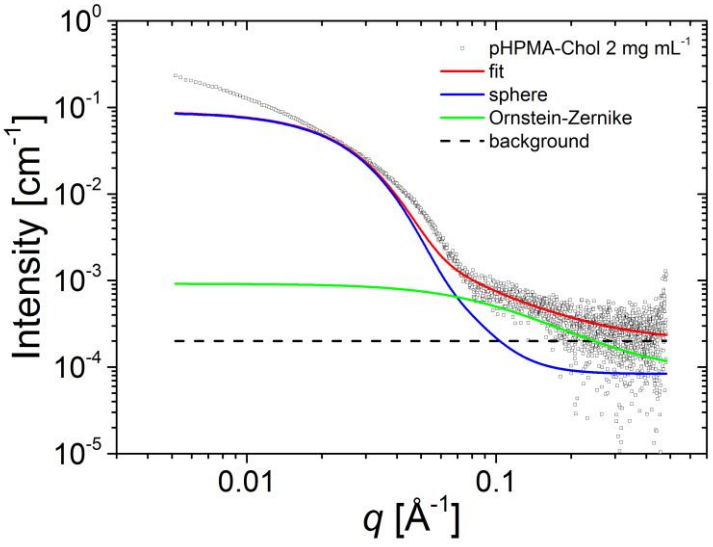

Figure A.4: Model fit of the SAXS curve of *p*HPMA-Chol-1 having a concentration of 2.0 mg mL^{-1} together with the contributions (equation 4.10).

Appendix B. Supporting information for Chapter 6

Modeling of fluorescence lifetime using lifetime distribution functions

The following codes are to be used in Igor Pro environment:

```
Function LnSN(cw,yw,xw) : FitFunc
	Wave cw,yw,xw
#if exists("LnSNX")
	yw = LnSNX(cw,xw)
#else
	yw = fLnSN(cw,xw)
#endif
	return(0)
End
Function fLnSN(w,t) : FitFunc
	Wave w
	Variable t
	Variable answer
	Variable answer1
	Variable answer2
	Variable answer3
Variable ss1,ss2,ss3
//Modeling of lifetime using a lognormal distribution function
for(ss1=0.05; ss1<=12; ss1+=0.01)
answer1 += exp(-(ln(ss1)-w[4])^2/(2*w[3]^2))*exp(-t/(w[2]+ss1))/(ss1*w[3]*(w[2]+ss1))
Endfor
answer1 *= w[1]/sqrt(2*pi)
//Endlognormal
```

```
//Modeling of lifetime using a single exponential function
answer2 = w[5]*exp(-t/w[6])
//Endsingle
// Modeling of lifetime using a normal distribution function
for(ss2=1;ss2<=30;ss2+=0.01)
answer3 += exp(-(ss2^2)/200)*exp(-t/(w[8]+(ss2/10)*w[9]))/(w[8]+(ss2/10)*w[9])
Endfor
for(ss3=1;ss3<=30;ss3+=0.01)
answer3 += exp(-(ss2^2)/200)*exp(-t/(w[8]-(ss2/10)*w[9]))/(w[8]-(ss2/10)*w[9])
Endfor
answer3 += exp(-t/w[8])/w[8]
answer3 *= (w[7]/sqrt(2*pi*(w[9]^2)))
//Endsingle
answer += w[0] + answer1 + answer2 + answer3
return answer
End
```

Background discrimination using lifetime decay patterns

A solution of *p*HPMA-Chol-2 enriched with *p*HPMA-Chol* having a concentration of 35 μM is measured using fluorescence lifetime correlation spectroscopy (FLCS) and the resulting autocorrelation functions with and without the background discrimination are plotted together (Figure B.1). By fitting equation 4.30 to the obtained autocorrelation functions, it is found that the average number of molecules decreases from 1.35 ± 0.01 (black) to 1.22 ± 0.01 (red) after applying the background discrimination function. The reduced number of molecules leads to a higher amplitude of the autocorrelation function, which normally results in better determined diffusion times.

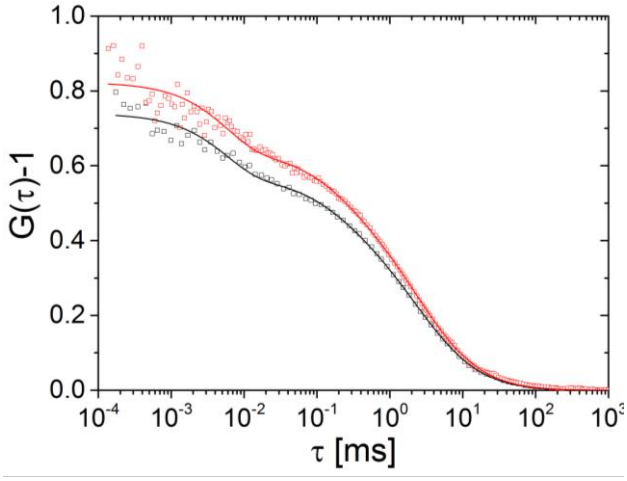

Figure B.1: FLCS autocorrelation functions of a solution of *p*HPMA-Chol-2 (enriched with *p*HPMA-Chol*) at 35 µM (black symbols) together with the fits (lines). After elimination of the fluorescence background, the average number of molecules decreases from 1.35 (black, no background discrimination) to 1.22 (red, with background discrimination).

Fitting of the autocorrelation functions of the mixed solutions of *p*HPMA-Chol-2 copolymer and HSA. All obtained autocorrelation functions and the corresponding fits are shown in Figure B.2. The resulting fit parameters are summarized in Table B.1. It is seen that the variation of the autocorrelation functions obtained from the same sample is mainly due to a different number of molecules which cannot be controlled precisely experimentally.

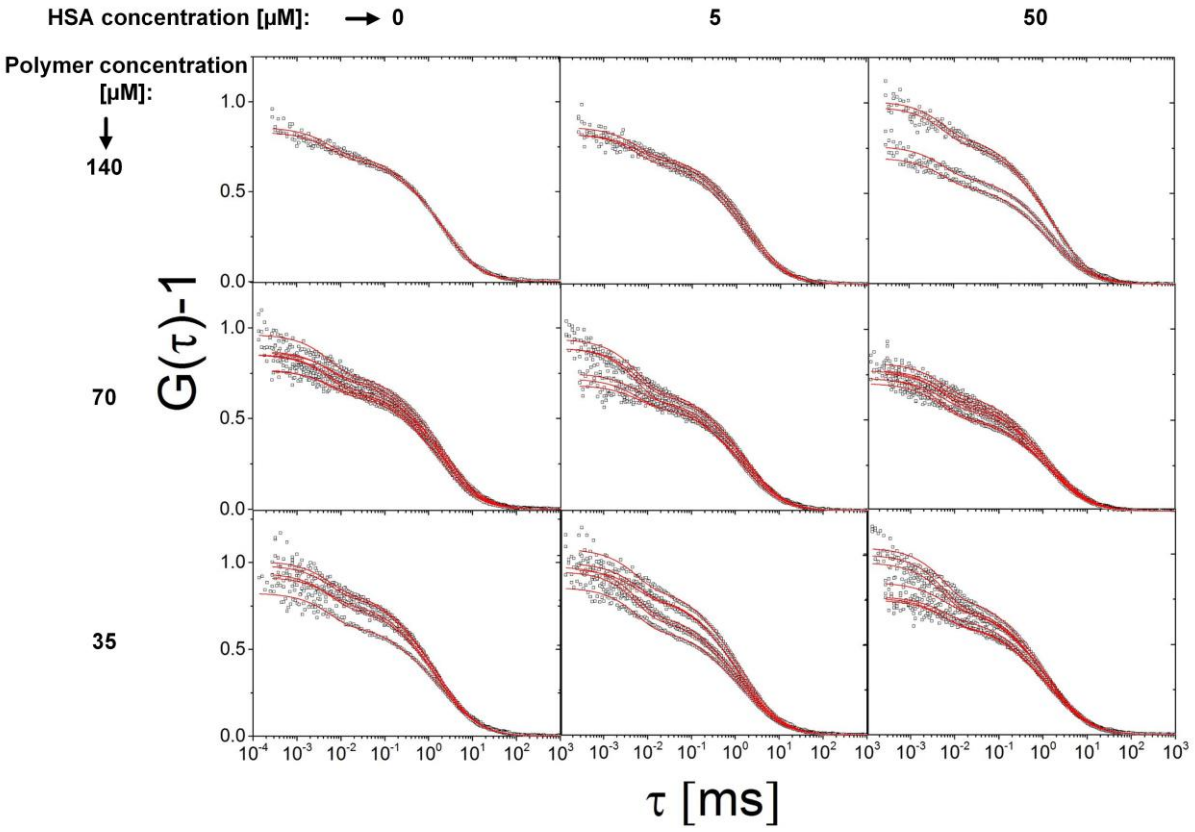

Figure B.2: Autocorrelation functions of mixed solutions of *p*HPMA-Chol-2 copolymer and HSA (symbols) measured using FLCS and fits of equation 4.30. Concentrations of polymer and HSA for respective plots are given on the left and on the top.

Table B.1: Fit parameters of mixed solutions using equation 4.30.

Concentration	# [a]	ρ	$\Delta\rho$	τ [ms]	$\Delta\tau$ [ms]	N	ΔN	T	ΔT
c(*p*HPMA-Chol-2): 35 µM *c*(HSA): 0 µM	1	0.68	0.02	2.92	0.20	1.22	0.01	0.22	0.01
	2	0.68	0.03	2.44	0.17	0.99	0.01	0.18	0.01
	3	0.69	0.02	2.43	0.12	1.02	0.00	0.17	0.01
	4	0.71	0.04	2.36	0.21	1.07	0.01	0.21	0.01
	5	0.71	0.02	2.34	0.10	1.09	0.00	0.16	0.01
c(*p*HPMA-Chol-2): 35 µM *c*(HSA): 5 µM	1	0.64	0.03	2.42	0.17	1.22	0.01	0.28	0.01
	2	0.65	0.03	2.30	0.18	1.07	0.01	0.28	0.01
	3	0.65	0.03	2.20	0.18	1.10	0.01	0.29	0.01
	4	0.66	0.02	2.23	0.13	0.97	0.00	0.21	0.01
	5	0.66	0.02	1.95	0.08	1.05	0.00	0.20	0.00
	6	0.66	0.02	2.19	0.10	1.08	0.00	0.18	0.01

c(*p*HPMA-Chol-2): 35 μM *c*(HSA): 52 μM	1	0.63	0.03	2.06	0.16	0.97	0.00	0.27	0.01
	2	0.64	0.03	2.09	0.16	1.00	0.00	0.29	0.01
	3	0.63	0.03	2.36	0.17	1.05	0.00	0.27	0.01
	4	0.67	0.03	2.12	0.16	1.19	0.01	0.18	0.01
	5	0.64	0.02	2.29	0.15	1.31	0.01	0.16	0.01
	6	0.66	0.04	2.20	0.21	1.32	0.01	0.20	0.01
	7	0.65	0.02	2.29	0.11	1.34	0.01	0.18	0.01
c(*p*HPMA-Chol-2): 70 μM *c*(HSA): 0 μM	1	0.73	0.02	2.90	0.15	1.04	0.00	0.23	0.01
	2	0.73	0.02	2.96	0.17	1.17	0.01	0.23	0.01
	3	0.74	0.02	3.22	0.13	1.17	0.00	0.21	0.01
	4	0.70	0.02	2.48	0.15	1.15	0.01	0.18	0.01
	5	0.73	0.02	2.56	0.14	1.16	0.01	0.16	0.01
	6	0.75	0.03	2.22	0.14	1.31	0.01	0.15	0.01
	7	0.74	0.02	2.33	0.11	1.30	0.01	0.18	0.01
c(*p*HPMA-Chol-2): 70 μM *c*(HSA): 5 μM	1	0.61	0.03	2.02	0.15	1.12	0.00	0.32	0.01
	2	0.71	0.03	2.15	0.14	1.06	0.00	0.30	0.01
	3	0.69	0.03	2.27	0.14	1.12	0.00	0.27	0.01
	4	0.69	0.02	2.33	0.14	1.32	0.01	0.19	0.01
	5	0.69	0.05	2.26	0.25	1.37	0.01	0.21	0.01
	6	0.69	0.02	2.29	0.14	1.45	0.01	0.17	0.01
c(*p*HPMA-Chol-2): 70 μM *c*(HSA): 52 μM	1	0.67	0.02	2.53	0.14	1.30	0.00	0.24	0.01
	2	0.68	0.03	2.21	0.18	1.37	0.01	0.28	0.01
	3	0.64	0.02	2.73	0.17	1.43	0.01	0.27	0.01
	4	0.65	0.02	2.12	0.11	1.23	0.00	0.21	0.01
	5	0.63	0.03	2.07	0.17	1.29	0.01	0.20	0.01
	6	0.63	0.03	1.98	0.15	1.32	0.01	0.21	0.01
	7	0.63	0.03	2.03	0.17	1.38	0.01	0.21	0.01
c(*p*HPMA-Chol-2): 140 μM *c*(HSA): 0 μM	1	0.77	0.02	2.48	0.11	1.17	0.01	0.17	0.01
	2	0.75	0.01	2.94	0.10	1.20	0.00	0.17	0.01
c(*p*HPMA-Chol-2): 140 μM *c*(HSA): 5 μM	1	0.69	0.02	2.45	0.13	1.21	0.01	0.19	0.01
	2	0.71	0.01	2.46	0.09	1.21	0.00	0.15	0.00
	3	0.75	0.02	2.58	0.12	1.15	0.01	0.18	0.01
c(*p*HPMA-Chol-2): 140 μM *c*(HSA): 52 μM	1	0.70	0.02	2.26	0.10	0.99	0.00	0.19	0.01
	2	0.71	0.02	2.34	0.13	1.02	0.01	0.20	0.01
	3	0.73	0.02	2.32	0.13	1.32	0.01	0.22	0.01

4	0.68	0.02	2.33	0.11	1.44	0.01	0.22	0.01

(a) #: repetition number of the same sample. *c*(*p*HPMA-Chol-2) and *c*(HSA) denote the concentration of *p*HPMA and HSA, respectively.

List of publications

1. X. Zhang, B.-J. Niebuur, P. Chytil, T. Etrych, S. K. Filippov, A. Kikhney, D. C. F. Wieland, D. I. Svergun, C.M. Papadakis: Macromolecular pHPMA-Based Nanoparticles with Cholesterol for Solid Tumor Targeting: Behavior in HSA Protein Environment. *Biomacromolecules* **2018**, 19, 470-480.

2. X. Zhang, P. Chytil, T. Etrych, W. Liu, L. Rodrigues, G. Winter, S. K. Filippov, C. M. Papadakis: Binding of HSA to Macromolecular pHPMA Based Nanoparticles for Drug Delivery: An Investigation Using Fluorescence Methods. *Langmuir* **2018**, 34, 7998–8006.

Conference talks

1. X. Zhang, B.-J. Niebuur, P. Chytil, T. Etrych, S. K. Filippov, A. Kikhney, F. Wieland, D. I. Svergun, C. M. Papadakis: HPMA-Based Drug Delivery System -Behavior in Protein Environment. DPG-Frühjahrstagung, Dresden, 19 – 24 March 2017

2. X. Zhang, B.-J. Niebuur, P. Chytil, T. Etrych, D. I. Svergun, S. K. Filippov, C. M. Papadakis: HPMA-Based Drug Delivery System -Investigated in Protein Environment Using Fluorescence Methods. 3rd Workshop ”Fluorescence Correlation Spectroscopy in Soft Matter Science”, Garching, 11 – 12 October 2017

Conference poster presentations

1. X. Zhang, B.-J. Niebuur, E. Lomkova, P. Chytil, S. K. Filippov, C. M.Papadakis: A Fluorescence Lifetime Study of the Drug Delivery System Based on HPMA Copolymers. 2nd Internal Biennial Science Meeting of the MLZ, Grainau, 15 – 18 June 2015

2. X. Zhang, B.-J. Niebuur, P. Chytil, T. Etrych, S. K. Filippov, A. Kikhney, F. Wieland, D. I. Svergun, C.M. Papadakis: Macromolecular HPMA-based Drug Delivery System - Behavior in Protein Environment. DPG-Frühjahrstagung, Regensburg, 6 – 11 March 2016

3. X. Zhang, B.-J. Niebuur, P. Chytil, T. Etrych, S. K. Filippov, A. Kikhney, F. Wieland, D. I. Svergun, C. M. Papadakis: Macromolecular HPMA-based Drug Delivery System - Behavior in Protein Environment. 30th Conference of the European Colloid and Interface Society, Rome, 4 – 9 September 2016

4. X. Zhang, B.-J. Niebuur, P. Chytil, T. Etrych, S. K. Filippov, A. Kikhney, F. Wieland, D. I. Svergun, C. M. Papadakis: Macromolecular HPMA-Based Drug Delivery System– Behavior in Protein Environment. 13th Zsigmondy Colloquium, Saarbrücken, 5 – 7 April 2017

5. X. Zhang, B.-J. Niebuur, P. Chytil, T. Etrych, S. K. Filippov, A. Kikhney, F. Wieland, D. I. Svergun, C. M. Papadakis: Macromolecular HPMA-Based Drug Delivery System– Behavior in Protein Environment. 9th International Symposium ”Molecular Mobility and Order in Polymer Systems”, Saint Petersburg, 19 – 23 June 2017

6. X. Zhang, B.-J. Niebuur, P. Chytil, T. Etrych, S. K. Filippov, A. Kikhney, F. Wieland, D. I. Svergun, C. M. Papadakis: Macromolecular HPMA-Based Drug Delivery System– Behavior in Protein Environment. Kolloid-Tagung “Multiresponsive systems”, Garching, 9 – 11 October 2017

Bibliography

(1) Markovsky, E.; Baabur-Cohen, H.; Eldar-Boock, A.; Omer, L.; Tiram, G.; Ferber, S.; Ofek, P.; Polyak, D.; Scomparin, A.; Satchi-Fainaro, R. *J. Control. Release* **2012**, 161, 446-460.

(2) Cassidy, J.; Newell, D. R.; Wedge, S. R.; Cummings, J. *Cancer Surv* **1993**, 17, 315-341.

(3) Duncan, R. *Adv. Drug Deliv. Rev.* **2009**, 61, 1131-1148.

(4) Duncan, R.; Vicent, M. J. *Adv. Drug Deliv. Rev.* **2010**, 62, 272-282.

(5) Kopeček, J.; Kopečková, P. *Adv. Drug Deliv. Rev.* **2010**, 62, 122-149.

(6) Ulbrich, K.; Šubr, V. *Adv. Drug Deliv. Rev.* **2010**, 62, 150-166.

(7) Vicent, M. J.; Manzanaro, S.; de la Fuente, J. A.; Duncan, R. *J. Drug Target.* **2004**, 12, 503-515.

(8) Griffiths, P. C.; Paul, A.; Apostolovic, B.; Klok, H.-A.; de Luca, E.; King, S. M.; Heenan, R. K. *J. Control. Release* **2011**, 153, 173-179.

(9) Chytil, P.; Etrych, T.; Koňák, Č.; Šírová, M.; Mrkvan, T.; Bouček, J.; Říhová, B.; Ulbrich, K. *J. Control. Release* **2008**, 127, 121-130.

(10) Filippov, S. K.; Chytil, P.; Konarev, P. V.; Dyakonova, M.; Papadakis, C. M.; Zhigunov, A.; Plestil, J.; Stepanek, P.; Etrych, T.; Ulbrich, K.; Svergun, D. I. *Biomacromolecules* **2012**, 13, 2594-2604.

(11) Filippov, S. K.; Franklin, J. M.; Konarev, P. V.; Chytil, P.; Etrych, T.; Bogomolova, A.; Dyakonova, M.; Papadakis, C. M.; Radulescu, A.; Ulbrich, K.; Stepanek, P.; Svergun, D. I. *Biomacromolecules* **2013**, 14, 4061-4070.

(12) Lynch, I.; Dawson, K. A. *Nanotoday* **2008**, 3, 40-47.

(13) Pan, H.; Qin, M.; Meng, W.; Cao, Y.; Wang, W. *Langmuir* **2012**, 28, 12779-12787.

(14) Zhu, X.; Liu, M. *Langmuir* **2011**, 27, 12844-12850.

(15) Mahmoudi, M.; Lynch, I.; Ejtehadi, M. R.; Monopoli, M. P.; Bombelli, F. B.; Laurent, S. *Chem. Rev.* **2011**, 111, 5610-5637.

(16) Saifer, A.; Goldman, L. *J. Lipid Res.* **1961**, 2, 268-270.

(17) Brock, A. *Acta Pharmacol. Toxicol. (Copenh)* **1976**, 38, 497-507.

(18) Spector, A. A. *Methods Enzymol.* **1986**, 128, 320-339.

(19) Wang, C. S.; Bass, H.; Whitmer, R.; McConathy, W. J. *J. Lipid Res.* **1993**, 34, 2091-2098.

(20) Curry, S.; Brick, P.; Franks, N. P. *Biochimica Et Biophysica Acta-Molecular and Cell Biology of Lipids* **1999**, 1441, 131-140.

(21) Kobayashi, T.; Tanaka-Ishii, R.; Taguchi, R.; Ikezawa, H.; Murakami-Murofushi, K. *Life Sciences* **1999**, 65, 2185-2191.

(22) Simard, J. R.; Zunszain, P. A.; Hamilton, J. A.; Curry, S. *J. Mol. Biol* **2006**, 361, 336-351.

(23) Charbonneau, D.; Beauregard, M.; Tajmir-Riahi, H. A. *Journal of Physical Chemistry B* **2009**, 113, 1777-1784.

(24) Thakur, R.; Das, A.; Chakraborty, A. *RSC Adv.* **2014**, 4, 14335-14347.

(25) Cedervall, T.; Lynch, I.; Lindman, S.; Berggård, T.; Thulin, E.; Nilsson, H.; Dawson, K. A.; Linse, S. *Proc. Natl. Acad. Sci. U. S. A.* **2007**, 104, 2050-2055.

(26) Rubinstein, M.; Colby, R. H. *Polymer Physics.*, Oxford University Press, 2003.

(27) Gedde, U. W. *Polymer Physics.*, Kluwe Academic Publishers, 2001.

(28) Miller-Chou, B. A.; Koenig, J. L. *Prog. Polym. Sci.* **2003**, 28 1223–1270.

(29) Flory, P. J. *J. Chem. Phys.* **1942**, 10, 51-61.

(30) Huggins, M. L. *J. Am. Chem. Soc.* **1942**, 64,, 1712-1719.

(31) Huggins, M. L. *J. Phys. Chem.* **1942**, 46, 151-158.

(32) Fisicaro, E.; Compari, C.; Duce, E.; Biemmi, M.; Peroni, M.; Braibanti, A. *Phys. Chem. Chem. Phys.* **2008**, 10, 3903-3914

(33) Rosenholm, J. B.; Burchfield, T. E.; Hepler, L. G. *J. Colloid Interface Sci.* **1980**, 78, 191-194.

(34) Hamley, I. W. *The Physics of Block Copolymers.*, Oxford University Press, 1998.

(35) Alexandridis, P.; Lindman, B. *Amphiphilic Block Copolymers: Self-Assembly and Applications.*, Elsevier, 2000.

(36) Mai, Y. Y.; Eisenberg, A. *Chem. Soc. Rev.* **2012**, 41, 5969-5985.

(37) Darling, S. B. *Prog. Polym. Sci.* **2007**, 32, 1152-1204.

(38) Rosler, A.; Vandermeulen, G. W. M.; Klok, H. A. *Adv. Drug Deliv. Rev.* **2001**, 53, 95-108.

(39) Li, L.; Raghupathi, K.; Song, C.; Prasad, P.; Thayumanavan, S. *Chem. Commun.* **2014**, 50, 13417-13432.

(40) Sato, T. *Polymers* **2018**, 10, 73.

(41) Tominaga, Y.; Mizuse, M.; Hashidzume, A.; Morishima, Y.; Sato, T. *J. Phys. Chem. B* **2010**, 114, 11403-11408.

(42) Yamakawa, H.; Yoshizaki, T. *Helical Wormlike Chains in Polymer Solutions.*, Springer: Berlin/heidelberg, Germany, 2016.

(43) Shimada, J.; Yamakawa, H. *J. Chem. Phys.* **1986**, 85, 591-600.

(44) Yamakawa, H.; Stackmayer, W. H. *J. Chem. Phys.* **1972**, 57, 2843-2854.

(45) Kawata, T.; Hashidzume, A.; Sato, T. *Macromolecules* **2007**, 40, 1174-1180.

(46) Tian, F.; Yu, Y.; Wang, C.; Yang, S. *Macromolecules* **2008**, 41, 3385-3388.

(47) Vilar, G.; Tulla-Puche, J.; Albericio, F. *Curr. Drug Deliv.* **2012**, 9, 367 - 394.

(48) Kopecek, J.; Kopeckova, P. *Drug Delivery in Oncology: From Basic Research to Cancer Therapy.*, WILEY-VCH, 2011.

(49) Jatzkewits, H. *Z. NatuNaturforsch.* **1955**, 10b 27–31.

(50) Shumikhina, K. I.; Panarin, E. F.; Ushakov, S. N. *Antibiotiki* **1966**, 11, 767–770.

(51) Givental, N. I.; Ushakov, S. N.; Panari, E. F.; Popov, G. O. *Antibiotiki* **1965**, 10, 701–706.

(52) Ringsdorf, H. *J. Polym. Sci.* **1975**, 51, 135–153.

(53) Godwin, A.; Bolina, K.; Clochard, M.; Dinand, E.; Rankin, S.; Simic, S.; Brocchini, S. *J. Pharm. Pharmacol.* **2001**, 53, 1175–1184.

(54) Knop, K.; Hoogenboom, R.; Fischer, D.; Schubert, U. S. *Angew. Chem. Int. Ed.* **2010**, 49, 6288 – 6308.

(55) Turecek, P. L.; Bossard, M. J.; Schoetens, F.; Ivens, I. A. *J. Pharm. Sci.* **2016**, 105, 460-475.

(56) Kolate, A.; Baradia, D.; Patil, S.; Vhora, I.; Kore, G.; Misra, A. *J. Control. Release* **2014**, 192, 67-81.

(57) Bunker, A. *Phys. Procedia* **2012**, 34, 24 – 33.

(58) Lollo, G.; Rivera-Rodriguez, G. R.; Bejaud, J.; Montier, T.; Passirani, C.; Benoit, J.-P.; García-Fuentes, M.; Alonso, M. J.; Torres, D. *Eur. J. Pharm. Biopharm.* **2014**, 87, 47-54.

(59) Ogunleye, A.; Bhat, A.; Irorere, V. U.; Hill, D.; Williams, C.; Radecka, I. *Microbiology* **2015**, 161, 1-17.

(60) Khalil, I. R.; Burns, A. T. H.; Radecka, I.; Kowalczuk, M.; Khalaf, T.; Adamus, G.; Johnston, B.; Khechara, M. P. *Int. J. Mol. Sci.* **2017**, 18, 313.

(61) Richard, A.; Margaritis, A. *Crit. Rev. Biotechnol.* **2001**, 21, 219-232.

(62) Ulbrich, K.; Etrych, T.; Chytil, P.; Jelínková, M.; Říhová, B. *J. Drug Target.* **2004**, 12, 477-489.

(63) Bae, Y.; Jang, W. D.; Nishiyama, N.; Fukushima, S.; Kataoka, K. *Mol. BioSyst.* **2005**, 1, 242-250.

(64) Muharnmad, F.; Guo, M. Y.; Qi, W. X.; Sun, F. X.; Wang, A. F.; Guo, Y. J.; Zhu, G. S. *J. Am. Chem. Soc.* **2011**, 133, 8778-8781.

(65) Gupta, P.; Vermani, K.; Garg, S. *Drug Discov. Today* **2002**, 7, 569-579.

(66) Sershen, S. R.; Westcott, S. L.; Halas, N. J.; West, J. L. *J. Biomed. Mater. Res.* **2000**, 51, 293-298.

(67) Bikram, M.; Gobin, A. M.; Whitmire, R. E.; West, J. L. *J. Control. Release* **2007**, 123, 219-227.

(68) Needham, D.; Dewhirst, M. W. *Adv. Drug Deliv. Rev.* **2001**, 53, 285-305.

(69) Guduru, R.; Liang, P.; Runowicz, C.; Nair, M.; Atluri, V.; Khizroev, S. *Sci. Rep.* **2013**, 3.

(70) Chandran, P. R.; Sandhyarani, N. *RSC Adv.* **2014**, 4, 44922-44929.

(71) Hurrell, S.; Cameron, R. E. *Polym. Int.* **2003**, 52, 358-366.

(72) Kataoka, K.; Harada, A.; Nagasaki, Y. *Adv. Drug Deliv. Rev.* **2001**, 47, 113-131.

(73) Fang, J.; Nakamura, H.; Maeda, H. *Adv. Drug Deliv. Rev.* **2011**, 63, 136-151.

(74) Maeda, H.; Nakamura, H.; Fang, J. *Adv. Drug Deliv. Rev.* **2013**, 65, 71-79.

(75) Noguchi, Y.; Wu, J.; Duncan, R.; Strohalm, J.; Ulbrich, K.; Akaike, T.; Maeda, H. *Jpn. J. Cancer Res.* **1998**, 89, 307-314.

(76) Talelli, M.; Rijcken, C. J. F.; Nostrum, C. F. v.; Storm, G.; Hennink, W. E. *Adv. Drug Deliv. Rev.* **2010**, 62, 231-239.

(77) Rahman, M.; Laurent, S.; Tawil, N.; Yahia, L. H.; Mahmoudi, M. *Protein-Nanoparticle Interactions: The Bio-Nano Interface.*, Springer Berlin Heidelberg, 2013.

(78) Lynch, I.; Cedervall, T.; Lundqvist, M.; Cabaleiro-Lago, C.; Linse, S.; Dawson, K. A. *Adv. Colloid Interface Sci.* **2007**, 134-135, 167-174.

(79) Lindman, S.; Lynch, I.; Thulin, E.; Nilsson, H.; Dawson, K. A.; Linse, S. *Nano Lett.* **2007**, 7, 914-920.

(80) Cedervall, T.; Lynch, I.; Foy, M.; Berggård, T.; Donnelly, S. C.; Cagney, G.; Linse, S.; Dawson, K. A. *Angew. Chem. Int. Ed.* **2007**, 46, 5754-5756.

(81) Mahmoudi, M.; Simchi, A.; Imani, M. *J. Phys. Chem. C* **2009**, 113, 9573-9580.

(82) Mahmoudi, M.; Simchi, A.; Imani, M.; Shokrgozar, M. A.; Milani, A. S.; Häfeli, U. O.; Stroeve, P. *Colloids Surf. B: Biointerfaces* **2010**, 75, 300-309.

(83) Walczyk, D.; Bombelli, F. B.; Monopoli, M. P.; Lynch, I.; Dawson, K. A. *J. Am. Chem. Soc.* **2010**, 132, 5761-5768.

(84) Aggarwal, P.; Hall, J. B.; McLeland, C. B.; Dobrovolskaia, M. A.; McNeil, S. E. *Adv. Drug Deliv. Rev.* **2009**, 61, 428-437.

(85) Lundqvist, M.; Stigler, J.; Cedervall, T.; Berggård, T.; Flanagan, M. B.; Lynch, I.; Elia, G.; Dawson, K. *ACS Nano* **2011**, 5, 7503-7509.

(86) Monopoli, M. P.; Aberg, C.; Salvati, A.; Dawson, K. A. *Nat. Nanotechnol.* **2012**, 7, 779-786.

(87) Shemetov, A. A.; Nabiev, I.; Sukhanova, A. *ACS Nano* **2012**, 6, 4585-4602.

(88) Walkey, C. D.; Chan, W. C. W. *Chemical Society Reviews* **2012**, 41, 2780-2799.

(89) Saptarshi, S. R.; Duschl, A.; Lopata, A. L. *J. Nanobiotechnology* **2013**, 11, 26.

(90) Yang, S. T.; Liu, Y.; Wang, Y. W.; Cao, A. *Small* **2013**, 9, 1635-1653.

(91) Kim, Y.; Ko, S. M.; Nam, J. M. *Chemistry – An Asian Journal* **2016**, 11, 1869-1877.

(92) Simberg, D.; Park, J. H.; Karmali, P. P.; Zhang, W. M.; Merkulov, S.; McCrae, K.; Bhatia, S. N.; Sailor, M.; Ruoslahti, E. *Biomaterials* **2009**, 30, 3926-3933.

(93) Monopoli, M. P.; Walczyk, D.; Campbell, A.; Elia, G.; Lynch, I.; Bombelli, F. B.; Dawson, K. A. *J. Am. Chem. Soc.* **2011**, 133, 2525-2534.

(94) Jansch, M.; Stumpf, P.; Graf, C.; Ruhl, E.; Muller, R. H. *Int. J. Pharm.* **2012**, 428, 125-133.

(95) Roach, P.; Farrar, D.; Perry, C. C. *J. Am. Chem. Soc.* **2005**, 127, 8168-8173.

(96) Mahmoudi, M.; Shokrgozar, M. A.; Sardari, S.; Moghadam, M. K.; Vali, H.; Laurent, S.; Stroeve, P. *Nanoscale* **2011**, 3, 1127-1138.

(97) Lacerda, S. H. D. P.; Park, J. J.; Meuse, C.; Pristinski, D.; Becker, M. L.; Karim, A.; Douglas, J. F. *ACS Nano* **2010**, 4, 365-379.

(98) Cox, M. C.; Barnham, K. J.; Frenkiel, T. A.; Hoeschele, J. D.; Mason, A. B.; He, Q.-Y.; Woodworth, R. C.; Sadler, P. J. *J. Biol. Inorg. Chem.* **1999**, 4, 621-631.

(99) Mahmoudi, M.; Simchi, A.; Milani, A. S.; Stroeve, P. *J. Colloid Interface Sci.* **2009**, 336, 510-518.

(100) Schulze, C.; Kroll, A.; Schulze, C.; Kroll, A.; Lehr, C.-M.; Schäfer, U. F.; Becker, K.; Schnekenburger, J.; Schulze Isfort, C.; Landsiedel, R.; Wohlleben, W. *Nanotoxicology* **2008**, 2, 51-61.

(101) Lundqvist, M.; Stigler, J.; Elia, G.; Lynch, I.; Cedervall, T.; Dawson, K. A. *Proc. Natl. Acad. Sci. U.S.A.* **2008**, 105, 14265-14270.

(102) Aggarwal, P.; Hall, J. B.; McLeland, C. B.; Dobrovolskaia, M. A.; McNeil, S. E. *Adv. Drug Deliv. Rev.* **2009**, 61, 428-437.

(103) Hemmelmann, M.; Mohr, K.; Fischer, K.; Zentel, R.; Schmidt, M. *Mol. Pharmaceutics* **2013**, 10, 3769−3775.

(104) Amoozgar, Z.; Yeo, Y. *Wiley Interdiscip. Rev. Nanomed. Nanobiotechnol.* **2012**, 4, 219-233.

(105) Kabanov, A. V.; Vinogradov, S. V. *Angew. Chem. Int. Ed.* **2009**, 48, 5418-5429.

(106) Obereigner, B.; Burešová, M.; Vrána, A.; Kopeček, J. *J. Polym. Sci. Polym. Symp.* **1979**, 66, 41-52.

(107) Filippov, S. K.; Vishnevetskaya, N. S.; Niebuur, B.-J.; Koziolová, E.; Lomkova, E. A.; Chytil, P.; Etrych, T.; Papadakis, C. M. *Colloid Polym. Sci.* **2017**, 295, 1313-1325.

(108) Walkey, C. D.; Olsen, J. B.; Guo, H.; Emili, A.; Chan, W. C. W. *J. Am. Chem. Soc.* **2012**, 134, 2139-2147.

(109) Gessner, A.; Waicz, R.; Lieske, A.; Paulke, B.-R.; Mäder, K.; Müller, R. H. *Int. J. Pharm.* **2000**, 196, 245-249.

(110) Papagiannopoulos, A.; Meristoudi, A.; Pispas, S.; Radulescu, A. *Biomacromolecules* **2016**, 17, 3816-3827.

(111) Papagiannopoulos, A.; Meristoudi, A.; Pispas, S.; Keiderling, U. *Soft Matter* **2016**, 12, 6547-6556.

(112) Vlassi, E.; Papagiannopoulos, A.; Pispas, S. *Eur. Polym. J.* **2017**, 88, 516-523.

(113) Vlassi, E.; Giannopoulos, A. P.; Pispas, S. *Colloid Polym. Sci.* **2017**, 295, 1359-1369.

(114) Adams, M. L.; Lavasanifar, A.; Kwon, G. S. *J. Pharm. Sci.* **2003**, 92, 1343-1355.

(115) Pippa, N.; Kaditi, E.; Pispas, S.; Demetzos, C. *Soft Matter* **2013**, 9, 4073-4082.

(116) Milonaki, Y.; Kaditi, E.; Pispas, S.; Demetzos, C. *J. Polym. Sci. Pol. Chem.* **2011**, 50, 1226–1237.

(117) Kragh-Hansen, U.; Minchiotti, L.; Brennan, S. O.; Sugita, O. *Eur. J. Biochem.* **1990**, 193, 169-174.

(118) Zhao, Y.; Marcel, Y. L. *Biochemistry* **1996**, 35, 7174-7180.

(119) Chytil, P.; Koziolova, E.; Etrych, T.; Ulbrich, K. *Macromol. Biosci.* **2018**, 18.

(120) Burtis, C. A.; Ashwood, E. R.; Bruns, D. E. *Tietz Textbook of Clinical Chemistry and Molecular Diagnostics*, Elsevier, 2012.

(121) Berman, H. M.; Westbrook, J.; Feng, Z.; Gilliland, G.; Bhat, T. N.; Weissig, H.; Shindyalov, I. N.; Bourne, P. E. *Nucleic Acids Res.* **2000**, 28, 235-242.

(122) Web page of the crystal structure of HSA, https://www.rcsb.org/structure/1E78, Accessed 30.06, 2018.

(123) Svergun, D. I.; Koch, M. H. J.; Timmins, P. A.; May, R. P. *Small Angle X-Ray and Neutron Scattering from Solutions of Biological Macromolecules.*, Oxford University Press, 2013.

(124) Stuhrmann, H. B. *Modern Aspects of Small-Angle Scattering.*, Kluwer Academic Publishers, 1993.

(125) Heller, W. T. *Acta Cryst. D* **2010**, 66, 1213-1217.

(126) Pedersen, J. S.; Svaneborg, C.; Almdal, K.; Hamley, I. W.; Young, R. N. *Macromolecules* **2003**, 36, 416-433.

(127) Knoll, W.; Ibel, K.; Sackmann, E. *Biochemistry* **1981**, 20, 6379-6383.

(128) Brasher, L. L.; Kaler, E. W. *Langmuir* **1996**, 12, 6270-6276.

(129) Zaccai, N. R.; Sandlin, C. W.; Hoopes, J. T.; Curtis, J. E.; Fleming, P. J.; Fleming, K. G.; Krueger, S., in *Methods in Enzymology*, ed. Z. Kelman, Academic Press, 2016, vol. 566, 159-210.

(130) Blanchet, C. E.; Spilotros, A.; Schwemmer, F.; Graewert, M. A.; Kikhney, A.; Jeffries, C. M.; Franke, D.; Mark, D.; Zengerle, R.; Cipriani, F.; Fiedler, S.; Roessle, M.; Svergun, D. I. *J. Appl. Crystallogr.* **2015**, 48, 431-443.

(131) Petoukhov, M. V.; Konarev, P. V.; Kikhney, A. G.; Svergun, D. I. *J. Appl. Crystallogr* **2007**, 40, S223-S228.

(132) Franke, D.; Kikhney, A. G.; Svergun, D. I. *Nucl. Instrum. Methods Phys. Res.* **2012**, 689, 52-59.

(133) Kline, S. R. *J. Appl. Crystallogr.* **2006**, 39, 895-900.

(134) Petoukhov, M. V.; Franke, D.; Shkumatov, A. V.; Tria, G.; Kikhney, A. G.; Gajda, M.; Gorba, C.; Mertens, H. D. T.; Konarev, P. V.; Svergun, D. I. *J. Appl. Crystallogr.* **2012**, 45, 342-350.

(135) Webpage of Heinz Maier-Leibnitz Zentrum, http://mlz-garching.de/instrumente-und-labore/nanostrukturen/kws-1.html, Accessed 23.02.2018, 2018.

(136) Bartlett, P.; Ottewil, R. H. *J. Chem. Phys.* **1992**, 96, 3306-3318.

(137) Svergun, D. I.; Feigin, L. A. *Structure Analysis by Small-Angle X-Ray and Neutron Scattering.*, Plenum Press, 1987.

(138) Shibayama, M.; Tanaka, T.; Han, C. C. *J. Chem. Phys.* **1992**, 97, 6829-6841.

(139) Freyer, M. W.; Lewis, E. A. in *Biophysical Tools for Biologists: Vol 1 in Vitro Techniques*, eds. J. J. Correia and H. W. Detrich, Elsevier Academic Press Inc, San Diego, 2008, vol. 84, pp. 79-113.

(140) Keller, S.; Vargas, C.; Zhao, H.; Piszczek, G.; Brautigam, C. A.; Schuck, P. *Anal. Chem.* **2012**, 84, 5066-5073.

(141) Krichevsky, O.; Bonnet, G. *Rep. Prog. Phys.* **2002**, 65, 251-297.

(142) Papadakis, C. M.; Košovan, P.; Richtering, W.; Wöll, D. *Colloid Polym. Sci.* **2014**, 292, 2399–2411.

(143) Koynov, K.; Butt, H.-J. *Curr. Opin. Colloid Interface Sci.* **2012**, 17, 377–387.

(144) Wöll, D. *RSC Adv.* **2014**, 4, 2447-2465.

(145) Böhmer, M.; Wahl, M.; Rahn, H. J.; Erdmann, R.; Enderlein, J. *J. Chem. Phys. Lett.* **2002**, 353, 439-445.

(146) Benda, A.; Hof, M.; Wahl, M.; Patting, M.; Erdmann, R.; Kapusta, P. *Rev. Sci. Instrum.* **2005**, 76, 33106.

(147) Enderlein, J.; Gregor, I. *Rev. Sci. Instrum.* **2005**, 76, 033102.

(148) Yuan, C. T.; Lin, C. A.; Lin, T. N.; Chang, W. H.; Shen, J. L.; Cheng, H. W.; Tang, J. *J. Chem. Phys.* **2013**, 139, 234311.

(149) Basit, H.; Lopez, S. G.; Keyes, T. E. *Methods* **2014**, 68, 286–299.

(150) Humpolíčková, J.; Benda, A.; Sýkora, J.; Macháň, R.; Kral, T.; Gasinska, B.; Enderlein, J.; Hof, M. *Biophys. J.* **2008**, 18, 679–684.

(151) Kapusta, P.; Wahl, M.; Benda, A.; Hof, M.; Enderlein, J. *J. Fluoresc.* **2007**, 17, 43-48.

(152) Müller, C. B.; Loman, A.; Pacheco, V.; Koberling, F.; Willbold, D.; Richtering, W.; Enderlein, J. *EPL* **2008**, 83, 46001.

(153) Lakowicz, J. R. *Principles of Fluorescence Spectroscopy*, Springer, New York, 2006.

(154) Papadopoulou, A.; Green, R. J.; Frazier, R. A. *J. Agric. Food Chem.* **2005**, 53, 158-163.

(155) Wang, Y.-Q.; Zhang, H.-M.; Zhang, G.-C.; Tao, W.-H.; Tang, S.-H. *J. Lumin.* **2007**, 126, 211–218.

(156) Hu, Y.-J.; Liu, Y.; Shen, X.-S.; Fang, X.-Y.; Qu, S.-S. *J. Mol. Struct.* **2008**, 738, 143–147.

(157) Neamtu, S.; Mic, M.; Bogdan, M.; Turcu, I. *J. Pharm. Biomed. Anal.* **2013**, 72, 134–138.

(158) Tayyab, S.; Izzudin, M. M.; Kabir, M. Z.; Feroz, S. R.; Tee, W.-V.; Mohamad, S. B.; Alias, Z. *J. Photochem. Photobiol., B* **2016**, 162 386–394.

(159) Shi, C.; Tang, H.; Xiao, J.; Cui, F.; Yang, K.; Li, J.; Zhao, Q.; Huang, Q.; Li, Y. *J. Agric. Food Chem.* **2017**, 65, 656−665.

(160) Kubista, M.; Sjoback, R.; Eriksson, S.; Albinsson, B. *Analyst* **1994**, 119, 417-419.

(161) Yappert, M. C.; Ingle, J. D. *Appl. Spectrosc.* **1989**, 43, 759-767.

(162) Wiechelman, K. J. *Am. Lab.* **1986**, 18, 49-53.

(163) MacDonald, B. C.; Lvinb, S. J.; Pattersonc, H. *Analytica Chimica Acta* **1997**, 338 155-162.

(164) Mertens, M. L.; Kägi, J. H. R. *Analytical Biochemistry* **1979**, 96, 448-455.

(165) Zhang, X.; Niebuur, B.-J.; Chytil, P.; Etrych, T.; Filippov, S. K.; Kikhney, A.; F.Wieland; Svergun, D. I.; Papadakis, C. M. *Biomacromolecules* **2018**, 2, 470-480.

(166) de Lauder, W. B.; Wahl, P. *Biochem. Biophys. Res. Com.* **1971**, 42, 398-404.

(167) Kubin, R. F.; Fletcher, A. N. *J. Lumin.* **1982**, 27, 455-462.

(168) Naldi, M.; Baldassarre, M.; Nati, M.; Laggetta, M.; Giannone, F. A.; Domenicali, M.; Bernardi, M.; Caraceni, P.; Bertucci, C. *J. Pharm. Biomed. Anal.* **2015**, 112, 169-175.

(169) Treuheit, M. J.; Kosky, A. A.; Brems, D. N. *Pharm. Res.* **2002**, 19, 511-516.

(170) Glatter, O.; Kratky, O. *Small-Angle X-ray Scattering*, Academic Press, London, 1982.

(171) Shieh, H.-S.; Hoard, L. G.; Nordman, C. E. *Acta Cryst.* **1981**, 37, 1538-1543.

(172) Charbonneau, D.; Beauregard, M.; Tajmir-Riahi, H.-A. *J. Phys. Chem. B* **2009**, 113, 1777–1784.

(173) Agudelo, D.; Bourassa, P.; Bruneau, J.; Bérubé, G.; Asselin, É.; Tajmir-Riahi, H. *PLOS one* **2012**, 7, e43814.

(174) Neamtu, S.; Mic, M.; Bogdan, M.; Turcu, I. *J. Pharm. Biomed. Anal.* **2013**, 72, 134-138.

(175) Huang, R. X.; Carney, R. R.; Ikuma, K.; Stellacci, F.; Lau, B. L. T. *Acs Nano* **2014**, 8, 5402-5412.

(176) De, M.; You, C.-C.; Srivastava, S.; Rotello, V. M. *J. Am. Chem. Soc.* **2007**, 129, 10747-10753.

(177) Byrne, N.; Wang, L. M.; Belieres, J. P.; Angell, C. A. *Chem. Comm.* **2007**, 2714-2716.

(178) Liu, P.; He, M.; Chen, F.; Li, X.; Zhang, C. *Protein Pept. Lett.* **2008**, 15, 360-364.

(179) Zhang, X.; Chytil, P.; Etrych, T.; Liu, W.; Rodrigues, L.; Winter, G.; Filippov, S. K.; Papadakis, C. M. *Langmuir* **2018**, 34, 7998-8006.

(180) Motlagh, N. S. H.; Parvin, P.; Ghasemi, F.; Atyabi, F. *Biomed. Opt. Express* **2016**, 7, 2400-2406.

(181) Sułkowska, A. *J. Mol. Struct.* **2002**, 614, 227-232.

(182) Helms, M. K.; Petersen, C. E.; Bhagavan, N. V.; Jameson, D. M. *FEBS Lett.* **1997**, 408, 67-70.

(183) Hazan, G.; Haas, E.; Steinberg, I. Z. *Biochim. Biophys. Acta* **1976**, 434, 144-153.

(184) Kasai, S.; Horie, T.; Mizuma, T.; Awazu, S. *J. Pharm. Sci.* **1987**, 76, 387–392.

(185) I., M.; Pecht, I.; Stryer, L. *Proc. Natl. Acad. Sci. USA* **1979**, 76, 56-60.

(186) Lakowicz, J. R.; Gryczynski, I. *Biophys. Chem.* **1992**, 45, 1-6.

(187) Vos, K.; van Hoek, A.; Visser, A. J. *Eur. J. Biochem.* **1987**, 165, 55–63.

(188) Marzola, P.; Gratton, E. *J. Phys. Chem.* **1991**, 95, 9488-9495.

(189) Abou-Zied, O. K.; Al-Shihi, O. I. K. *J. Am. Chem. Soc.* **2008**, 130, 10793-10801.

(190) Luxenhofer, R.; Han, Y. C.; Schulz, A.; Tong, J.; He, Z. J.; Kabanov, A. V.; Jordan, R. *Macromol. Rapid Commun.* **2012**, 33, 1613-1631.

(191) Zhang, N.; Pompe, T.; Amin, I.; Luxenhofer, R.; Werner, C.; Jordan, R. *Macromol. Biosci.* **2012**, 12, 926-936.

(192) Ulbricht, J.; Jordan, R.; Luxenhofer, R. *Biomaterials* **2014**, 35, 4848-4861.

(193) Tong, J.; Luxenhofer, R.; Yi, X.; Jordan, R.; Kabanov, A. V. *Mol. Pharm.* **2010**, 7, 984-992.

(194) Filippov, S. K. **2017**, unpublished data.

(195) Schuck, P. *Biophys. J.* **2000**, 78, 1606-1619.

(196) Houtman, J. C. D.; Brown, P. H.; Bowden, B.; Yamaguchi, H.; Appella, E.; Samelson, L. E.; Schuck, P. *Protein Sci.* **2007**, 16, 30-42.

Acknowledgments

I would like to thank many people who offered me help and support in many forms, without which I could never finish this study.

First and foremost, I would like to express my sincerest gratitude to my Doktormutter Prof. Dr. Christine M. Papadakis for the continuous support all the way throughout my Ph.D research. Not only for her enormous knowledge, but also for her encouragement and great patience. I am so grateful for the immense time she took and efforts she made supporting me finishing the study. When facing the most challenging difficulties, I never feel alone nor helpless.

I would like to thank Dr. Sergey K. Filippov (Institute of Macromolecular Chemistry, Prague) for the great collaboration on this project, and offering me opportunities carrying ITC and FLCS measurements. His deep understanding and enthusiasm for the project always inspire me.

I would like to thank Dr. Petr Chytil and Dr. Tomáš Etrych (Institute of Macromolecular Chemistry, Prague) for their insightful comments. Moreover, all polymer samples regarding this project was synthesized by Dr. Chytil, thus special thanks to his efforts on offering us first class materials.

Special thanks go to Dr. Dmitri I. Svergun and his beamline team at the European Molecular Biology Laboratory, Hamburg, Dr. D. C. Florian Wieland, Dr. Alexey Kikhney, Dr. Andrey Gruzinov and Dr. Tobias Graewert, who offered professional support by our collaborative SAXS experiments, and further suggestions and help in data analysis.

I am also grateful to Dr. Jiří Pánek (Institute of Macromolecular Chemistry, Prague) for his generous support during FLCS measurements and helpful discussions.

I am thankful to Dr. Henrich Frielinghaus (KWS-1 instruments at the Heinz Maier-Leibnitz Zentrum (MLZ), Garching) for his professional support during the SANS beamtime.

I wish to thank M. Sc. Letícia Rodrigues and M. Sc. Weiwei Liu (Chair of Pharmaceutical Technology and Biopharmaceutics, Department of Pharmacy, Ludwig Maximilian University of Munich), for their continuous assistance during experiments.

I thank my Bachelor students, B. Sc. Benedikt Grünewald and B. Sc. Thomas Retzer for their efforts in DLS measurements.

I would also like to express my thanks to my colleagues from the group of Physik weicher Materie: Dr. Anatoly V. Berezkin, Dr. Konstantinos N. Raftopoulos, Dr. Margarita A.

Dyakonova, Dr. Natalya S. Vishnevetskaya, M. Sc. Bart-Jan Niebuur, M. Sc. Florian Jung, M. Sc. Chia-Hsin Ko and M. Sc. Jia-Jhen Kang. They are always so kind to help. I enjoy our mental and physical trainings towards good and healthy scientists.

I would also like to acknowledge all members of the Chair of Functional Materials for the nice and friendly working atmosphere and the great time we had together.

Moreover, I thank Susanna Fink, Marion Waletzki and Carola Kappauf for their kind support, especially in bureaucratic aspects.

Furthermore, I would like to thank Deutsche Forschungsgemeinschaft (Pa 771/17-1) and the Czech Science Foundation (Grant No. 15-10527J) for the financial support.

Finally, I thank my family for their support. I feel so lucky to be someone you love, and someone who’s loving you.